Quarterly Technical Report

Solid State Research

1988:3

Lincoln Laboratory

MASSACHUSETTS INSTITUTE OF TECHNOLOGY

LEXINGTON, MASSACHUSETTS

ADA209645

This technical report has been reviewed and is approved for publication.

FOR THE COMMANDER

Hugh L. Southall

Hugh L. Southall, Lt. Col., USAF
Chief, ESD Lincoln Laboratory Project Office

MASSACHUSETTS INSTITUTE OF TECHNOLOGY
LINCOLN LABORATORY

SOLID STATE RESEARCH

QUARTERLY TECHNICAL REPORT

1 MAY — 31 JULY 1988

ISSUED 7 MARCH 1989

LEXINGTON   MASSACHUSETTS

ABSTRACT

This report covers in detail the research work of the Solid State Division at Lincoln Laboratory for the period 1 May through 31 July 1988. The topics covered are Electrooptical Devices, Quantum Electronics, Materials Research, Submicrometer Technology, Microelectronics, and Analog Device Technology. Funding is provided primarily by the Air Force, with additional support provided by the Army, DARPA, Navy, SDIO, NASA, and DOE.

TABLE OF CONTENTS

vi

LIST OF ILLUSTRATIONS

INTRODUCTION

1. ELECTROOPTICAL DEVICES

The integrated-optics wavefront measurement sensor has been used to determine the near-field radial phase variation of a 2-μs pulse from a 7-J dye laser with 200-ns resolution. Large fluctuations in the wavefront on this short time scale were clearly detected, which explain the previously measured poor quality of the time-averaged far field.

Mass transport has been observed on GaP and has been used to form microlenses by smoothing out etched multilevel mesa structures. Good quality microlenses have been obtained, which are potentially useful for collimating short-wavelength diode laser and laser array outputs.

A new reactor has been developed for atmospheric-pressure OMVPE growth of InP and related alloys. The reactor has a chimney geometry with a sidearm added for susceptor rotation and mechanized substrate loading.

A two-dimensional GaInAsP/InP diode laser array has been operated with CW power dissipation up to 500 W/cm^2 into a Si microchannel heat sink. A value of 0.06°C cm^2/W for the thermal resistance of the heat sink was deduced from the changes in threshold current of test lasers in the array.

Diffraction-coupled arrays of InGaAsP/InP buried-heterostructure lasers have been fabricated that utilize a novel scalloped mirror for greatly increased coupling between stripes. Cylindrical mirrors have been incorporated into the arrays to increase the power in the central far-field lobe.

2. QUANTUM ELECTRONICS

A Ti:Al$_2$O$_3$ laser has been operated in a ring configuration by displacing the pump beam in a standard astigmatically compensated folded laser cavity and satisfying a degeneracy condition by adjusting the position of the flat output mirror. Unidirectional operation has been achieved using the Faraday effect in a Brewster-angle prism employed for coarse mechanical tuning.

The energy of a 440-fs, 0.1-pJ pulse from a dye laser has been increased by a factor of 10^7 in a Ti:Al$_2$O$_3$ laser pumped by a copper-vapor laser. The 1.2-ps, 1-μJ output pulses have been compressed to 275 fs.

End-pumped Nd:LaF$_3$ and Nd:LaMgAl$_{11}$O$_{19}$ (Nd:LMA) lasers have been demonstrated with measured slope efficiencies of 47 and 31 percent, respectively, using a CW Ti:Al$_2$O$_3$ laser as a pump source. The slope efficiency for Nd:LaF$_3$ is typical for end-pumped Nd^{3+} lasers, but the slope value for Nd:LMA appears to be limited by excited state absorption.

Single-frequency Nd-doped solid state lasers have been constructed from large dielectrically coated wafers of various crystals, optically pumped with the close-coupled unfocused output of 20-mW GaAlAs diode lasers. Only single-longitudinal- and single-transverse-mode operation has been observed in these lasers up to many times threshold, with an instrument-limited linewidth of 5 kHz.

By mixing the outputs of two frequency-modulated Nd:YAG lasers, sum radiation has been generated with a broad spectral envelope and high spectral density. Single-frequency radiation has been obtained either by sum-frequency mixing the outputs of the two lasers modulated at the same frequency and depth but 180° out-of-phase, or by externally demodulating the output of one frequency-modulated Nd:YAG laser.

3. MATERIALS RESEARCH

A vertical rotating-disk reactor has been developed for growth of extremely uniform GaAs and AlGaAs layers by OMVPE. By operation at reduced pressure (0.2 atm) and a substrate rotation rate of 500 rpm, thickness uniformity of ± 1 percent and alloy compositional uniformity of ± 0.1 percent (e.g., ± 0.0003 in $Al_{0.3}Ga_{0.7}$) have been achieved for layers grown on 5-cm-diam. substrates.

4. SUBMICROMETER TECHNOLOGY

The new scanning-e-beam lithography system has passed its customer-acceptance testing and is in service. This machine has a minimum beam diameter of 8 nm and has produced patterns with features as small as 50 nm.

Damage on the vertical sidewalls of GaAs lines patterned by dry etching has been investigated. With the use of chlorine reactive-ion etching at low self-bias potentials or ion-beam-assisted etching with chlorine, it has been possible to pattern GaAs lines as narrow as 80 nm which remain conducting.

Boron-doped epitaxial diamond films have been grown on (100)-oriented diamond substrates. The films, which are smooth except for isolated defects, have been used to make working point-contact diodes, though large-area diodes are often shorted.

5. MICROELECTRONICS

A 420×420 CCD imager has been fabricated that features an on-chip frame-store and an output circuit with a noise level of 6 electrons rms at a 1-MHz data rate. The device was designed for multichip arrays and can be closely abutted to other imagers along three edges.

A technique has been developed using molecular beam epitaxy for growing GaAs and AlGaAs layers with thicknesses and Al content that vary in a controlled manner over the surface of a (100)-oriented GaAs substrate. The technique has been used to fabricate lasers which operate 40 nm apart in wavelength on two different regions of a single wafer, making possible multiwavelength optical interconnect technology.

6. ANALOG DEVICE TECHNOLOGY

Superconducting thin films of bismuth-strontium-calcium-copper oxide have been deposited using sequential e-beam evaporation of Cu, Bi, and $Sr_x Ca_{1-x}F_2$. The best films produced to date have a zero-resistance temperature of 90 K, a critical current density of 8×10^4 A/cm^2 at 77 K, and a nominal composition of $Bi_2Sr_2Ca_1Cu_2O_y$.

A process has been developed to fabricate all-Nb thin-film L-C resonators with Q >400 in the 10- to 20-MHz range for incorporation into the multichannel superconductive time-integrating correlator. Damage to the anodized-Nb dielectric is reduced to the required level by sputtering the Nb counterelectrode with a dc magnetron at a reduced power of 500 W and by using an elevated Ar pressure of 20 mTorr.

REPORTS
ON SOLID STATE RESEARCH

1 May Through 31 July 1988

PUBLISHED REPORTS

Journal Articles

JA No.

5955	Microwave Bulk-Acoustic-Wave Reflection-Grating Resonators	D.E. Oates J.Y. Pan	IEEE Trans. Ultrason. Ferroelec. Freq. Contr. **25**, 315 (1988)
6006	Pattern Transfer by Dry Etching Through Stencil Masks	S.W. Pang M.W. Geis W.D. Goodhue N.N. Efremow D.J. Ehrlich R.B. Goodman J.N. Randall	J. Vac. Sci. Technol. B **6**, 249 (1988)
6027	Monolithic GaAs/Si Optoelectronic Integrated Circuits	H.K. Choi	Optoelectronics — Devices and Technologies **2**, 265 (1987)
6029	A Review of Excimer Laser Projection Lithography	M. Rothschild D.J. Ehrlich	J. Vac. Sci. Technol. B **6**, 1 (1988)
6047	Spatial Light Modulators Using Charge-Coupled-Device Addressing and Electroabsorption Effects in GaAs/AlGaAs Multiple Quantum Wells	K.B. Nichols B.E. Burke B.F. Aull W.D. Goodhue B.F. Gramstorff C.D. Hoyt A. Vera	Appl. Phys. Lett. **52**, 1116 (1988)
6062	Residual Infrared Absorption in As-Grown and Annealed Crystals of Ti:Al$_2$O$_3$	R.L. Aggarwal R.E. Fahey A. Sanchez M.M. Stuppi A.J. Strauss C.P. Khattak*	IEEE J. Quantum Electron. **QE-24**, 1003 (1988)

---

* Author not at Lincoln Laboratory.

Meeting Speeches

MS No.

7626	Liquid-Solid Interface Morphologies and Defect Structures in Zone-Melting-Recrystallized Silicon-on Insulator Films	J.S. Im* C.K. Chen C.V. Thompson* M.W. Geis H. Tomita*	Mat. Res. Soc. Symp. Proc. Vol. **107** (1988), pp. 169-174
7666	Small-Signal Gain Measurements in a Ti:Al_2O_3 Amplifier	K.F. Wall R.L. Aggarwal R.E. Fahey A.J. Strauss	IEEE J. Quantum Electron. **QE-24**, 1016 (1988)
7685	Normal State Infrared Anisotropy of Polycrystalline $La_{1.85}Sr_{0.15}CuO_{4-y}$	G.L. Doll* J. Steinbeck* G. Dresselhaus* M.S. Dresselhaus* A.J. Strauss H.J. Zeiger	Mat. Res. Soc. Symp. Proc. Vol. **99** (1988), p. 841
7693	Magnetic Excitations in La_2CuO_4	I. Ohana* Y.C. Liu* M.S. Dresselhaus* G. Dresselhaus* P.J. Picone* H. Jenssen* D.R. Gabbe* H.J. Zeiger A.J. Strauss	Mat. Res. Soc. Symp. Proc. Vol. **99** (1988), p. 439
7711	International Solid State Circuits Conference, Panel on Issues in Fabrication of Neural Networks	J.P. Sage	1988 Technical Digest, Int. Solid-State Circuits Conf. (IEEE, New York, 1988), p. 213
7755	Silicon Permeable Base Transistors for Low-Phase-Noise Oscillator Applications Up to 20 GHz	D.D. Rathman W.K. Niblack*	1988 IEEE MTT-S Digest **S-4** (1988), p. 537
7838	High-Speed Resonant-Tunneling Diodes	E.R. Brown T.C.L.G. Sollner W.D. Goodhue C.L. Chen	*Quantum Well and Superlattice Physics II*, F. Capasso, G.H. Dohler, and J.N. Schulman, eds., Proc. SPIE **943** (1988), p. 2
7936	Comments on Monolithic Two-Dimensional Diode Laser Array vs Rack-and-Stack Hybrid Technology	J.N. Walpole	*High Power Laser Diodes and Applications*, L. Figueroa, ed., Proc. SPIE **893** (1988), pp. 131-132

---

* Author not at Lincoln Laboratory.

UNPUBLISHED REPORTS

Journal Articles

JA No.

6069	Optical Stark Effect in $Al_xGa_{1-x}As$/GaAs Coupled Quantum Wells	H.Q. Le J.V. Hryniewicz W.D. Goodhue V.A. Mims	Accepted by Opt. Lett.
6076	Fundamental Oscillations Up to 200 GHz in Resonant Tunneling Diodes and New Estimates of Their Maximum Oscillation Frequency from Stationary-State Tunneling Theory	E.R. Brown W.D. Goodhue T.C.L.G. Sollner	Accepted by J. Appl. Phys.
6082	Wideband Superconductive Chirp Filters	M.S. DiIorio R.S. Withers A.C. Anderson	Accepted by IEEE Trans. Microwave Theory Tech.
6083	RF Surface Resistance of YBaCuO Thin Films	M.S. DiIorio A.C. Anderson B-Y. Tsaur	Accepted by Phys. Rev. Lett.
6106	Reduction of Intermodulation Distortion in Interferometric Optical Modulators	L.M. Johnson H.V. Roussell	Accepted by Appl. Phys. Lett.
6112	Hydrodynamic Dispersion in Rotating Disk OMVPE Reactors: Numerical Simulation and Experimental Measurements	S. Patnaik* R.A. Brown* C.A. Wang	Accepted by J. Cryst. Growth
6114	Hybrid Approach to Two-Dimensional Surface-Emitting Diode Laser Arrays	J.P. Donnelly R.J. Bailey C.A. Wang G.A. Simpson K. Rauschenbach	Accepted by Appl. Phys. Lett.
6129	Reactive Ion Etching of GaAs and AlGaAs in a BCl_3-Ar Discharge	S.S. Cooperman* H.K. Choi H.H. Sawin* D.F. Kolesar	Accepted by J. Vac. Sci. Technol.
6131	InGaAsP/InP Buried-Heterostructure Lasers with Concurrent Fabrication of the Stripes and Mirrors	D. Yap J.N. Walpole Z.L. Liau	Accepted by Appl. Phys. Lett.

---

* Author not at Lincoln Laboratory.

* Author not at Lincoln Laboratory.

7727	Growth Characteristics of a Vertical Rotating-Disk OMVPE Reactor	C.A. Wang S. Patnaik* J.W. Caunt R.A. Brown*	4th International Conference on Metalorganic Vapor Phase Epitaxy, Hakone, Japan, 16-20 May 1988
7756B	Wide-Bandwidth Analog Signal Processing Using Superconductive Electronics	J.B. Green	Seminar, Oregon Center for Advanced Technical Education, Beaverton, Oregon, 29 June 1988
7767A	RF Losses in Superconducting Thin Films	A.C. Anderson	4th Annual Northeast Regional Meeting on Applications of High-T_c Superconductors: Status and Prospects, New Brunswick, New Jersey, 9-11 May 1988
7770A	Monolithic GaAs/Si Integration	G.W. Turner	Seminar, University of New Mexico, Albuquerque, New Mexico, 3 May 1988
7771A	A Tunable Solid State Laser: Titanium-Doped Sapphire	K.F. Wall	Solid-State Seminars, Yale University, New Haven, Connecticut, 6 May 1988
7787B	Superconductive RF Components for Enhanced Communications Systems	R.W. Ralston R.A. Murphy	1988 Tactical Communications Conference, Fort Wayne, Indiana, 3 May 1988
7787C	Passive Microwave and Milli-meter-Wave Superconductive Component Technology	R.W. Ralston	IEEE MTT-S International Microwave Symposium, Workshop on Superconductivity and Microwaves, New York, New York, 23 May 1988
7812	A Solid State CCD Smart Retina	A.M. Chiang	Artificial Intelligence Laboratory Seminar, MIT, Cambridge, Massachusetts, 2 May 1988
7815	Dry Etching Induced Damage on Vertical Sidewalls on GaAs Structures	S.W. Pang W.D. Goodhue T.M. Lyszczarz D.J. Ehrlich R.B. Goodman	The 32nd International Symposium on Electron, Ion, and Photon Beams, Ft. Lauderdale, Florida, 31 May-3 June 1988

* Author not at Lincoln Laboratory.

* Author not at Lincoln Laboratory.

---

* Author not at Lincoln Laboratory.

---

* Author not at Lincoln Laboratory.

ORGANIZATION

SOLID STATE DIVISION

A.L. McWhorter, *Head*
I. Melngailis, *Associate Head*
E. Stern, *Associate Head*
J.F. Goodwin, *Assistant*

N.L. DeMeo, Jr., *Associate Staff*

SUBMICROMETER TECHNOLOGY

D.J. Ehrlich, *Leader*
D.C. Shaver, *Assistant Leader*

Astolfi, D.K.
Black, J.G.
Dennis, C.L.
Doran, S.P.
Efremow, N.N., Jr.
Forte, A.R.
Gajar, S.A.*
Geis, M.W.
Horn, M.W.
Kunz, R.R.

Lyszczarz, T.M.
Maki, P.A.
Melngailis, J.†
Pang, S.W.
Rooks, M.J.
Rothschild, M.
Sedlacek, J.H.C.
Uttaro, R.S.
Young, E.M.

QUANTUM ELECTRONICS

A. Mooradian, *Leader*
P.L. Kelley, *Associate Leader*
A.Sanchez-Rubio, *Assistant Leader*

Aggarwal, R.L.
Barch, W.E.
Belanger, L.J.
Brailove, A.A.
Daneu, V.
DeFeo, W.E.
Fan, T.Y.
Hancock, R.C.
Hotaling, T.C.
Hryniewicz, J.V.
Jeys, T.H.
Lacovara, P.

Le, H.Q.
Menyuk, N.
Ochoa, J.R.
Schulz, P.A.
Sciacca, M.D.
Seppala, J.P.
Sharfin, W.F.
Sullivan, D.J.
Tapper, R.S.
Wall, K.F.
Zayhowski, J.J.

ELECTRONIC MATERIALS

A.J. Strauss, *Leader*
B-Y. Tsaur, *Associate Leader*
H.J. Zeiger, *Senior Staff*

Anderson, C.H., Jr.
Button, M.J.
Chen, C.K.
Choi, H.K.
Clark, H.R., Jr.
Connors, M.K.
Delaney, E.J.

Eglash, S.J.
Fahey, R.E.
Finn, M.C.
Iseler, G.W.
Kolesar, D.F.
Krohn, L., Jr.
Mastromattei, E.L.

Mattia, J.P.
Nitishin, P.M.
Pantano, J.V.
Tracy, D.M.
Turner, G.W.
Wang, C.A.
Young, K.K.

---

* Research Assistant
† Part Time

xxvii

APPLIED PHYSICS

R.C. Williamson, *Leader*
D.L. Spears, *Assistant Leader*
R.H. Rediker, *Senior Staff*

Aull, B.F.
Betts, G.E.
Bossi, D.E.*
Corcoran, C.J.*
Cox, C.H., III
Diadiuk, V.
Donnelly, J.P.
Ferrante, G.A.
Groves, S.H.
Harman, T.C.
Hovey, D.L.
Johnson, L.M.
Liau, Z.L.
Lind, T.A.
Missaggia, L.J.

Mull, D.E.
O'Donnell, F.J.
Palmacci, S.T.
Palmateer, S.C.
Pang, L.Y.*
Rauschenbach, K.
Reeder, R.E.
Roussell, H.V.
Seielstad, D.A.
Shipple, S.D.*
Tsang, D.Z.
Walpole, J.N.
Woodhouse, J.D.
Yap, D.*
Yee, A.C.

ANALOG DEVICE TECHNOLOGY

R.W. Ralston, *Leader*
R.S. Withers, *Associate Leader*

Anderson, A.C.
Arsenault, D.R.
Bhushan, M.
Boisvert, R.R.
Brogan, W.T.
Connelly, D.J.*
Denneno, A.P.
Dolat, V.S.
Fitch, G.L.
Frickey, J.M.
Green, J.B.
Holtham, J.H.

Lattes, A.L.
Lichtenwalner, D.J.*
Macedo, E.M., Jr.
Munroe, S.C.
Oates, D.E.
Pan, J.Y.*
Sage, J.P.
Seidel, M.N.*
Slattery, R.L.
Thompson, K.E.
Yu, L-S.*

MICROELECTRONICS

R.A. Murphy, *Leader*
E.D. Savoye, *Associate Leader*
B.B. Kosicki, *Assistant Leader*
R.W. Chick, *Senior Staff*

Actis, R.
Bales, J. W.*
Bennett, P.C.
Bozler, C.O.
Brown, E.R.
Burke, B.E.
Calawa, A.R.
Chen, C.L.
Chiang, A.M.
Chuang, M.L.*
Clifton, B.J.
Daniels, P.J.
Doherty, C.L., Jr.
Durant, G.L.

Felton, B.J.
Goodhue, W.D.
Gray, R.V.
Gregory, J.A.
Hollis, M.A.
Huang, J.C.M.
Johnson, B.W.
Johnson, K.F.
LaFranchise, J.R.
Lincoln G.A., Jr.
Mahoney, L.J.
Manfra, M.J.
Mathews, R.H.
McGonagle, W.H.

McIntosh, K.A.
Mountain, R.W.
Nichols, K.B.
Parker, C.D.
Pichler, H.H.
Rabe, S.
Rathman, D.D.
Reich, R.K.
Reinold, J.H., Jr.
Smith, F.W.*
Smythe, D.L., Jr.
Sollner, T.C.L.G.
Vera, A.
Wilde, R.E.

---

* Research Assistant

1. ELECTROOPTICAL DEVICES

1.1 TIME-RESOLVED WAVEFRONT MEASUREMENT OF A PULSED DYE LASER USING INTEGRATED OPTICS

An integrated-optics wavefront sensor with 200-ns temporal resolution[1] has been used to investigate the near-field phase and intensity distribution of a flashlamp-pumped pulsed dye laser with peak output in a 2-μs pulse of about 3.5 MW. Ten 200-ns snapshots of the wavefront have been taken during one 2-μs laser pulse. The time-resolved phase measurements have shown that a major portion of the measured degradation of the beam quality of the laser can be explained by dynamic processes that occur during the laser pulse.

The one-dimensional wavefront measurement sensor has two main components: a 20-element integrated-optics interferometer array on a $LiNbO_3$ substrate and a silicon imaging charge-coupled device (CCD) with buffer storage. The output of the CCD is read out into the computer between laser pulses. The 200-ns frame time is limited by the transfer rate of the signal from the CCD imager to the CCD buffer storage.

The dye laser consists of two separately pumped, longitudinal-flow dye cells, each of which is pumped by a pair of linear flashlamps. An unstable resonator configuration is used, which results in an annular output beam. Typically, the flashlamps support a 2,000-J pump discharge and the laser output is $\approx$7 J at repetition rates to 10 pps. Figure 1-1 shows the measured far-field energy distribution of a typical laser pulse. The beam is about 15 times its diffraction limit.
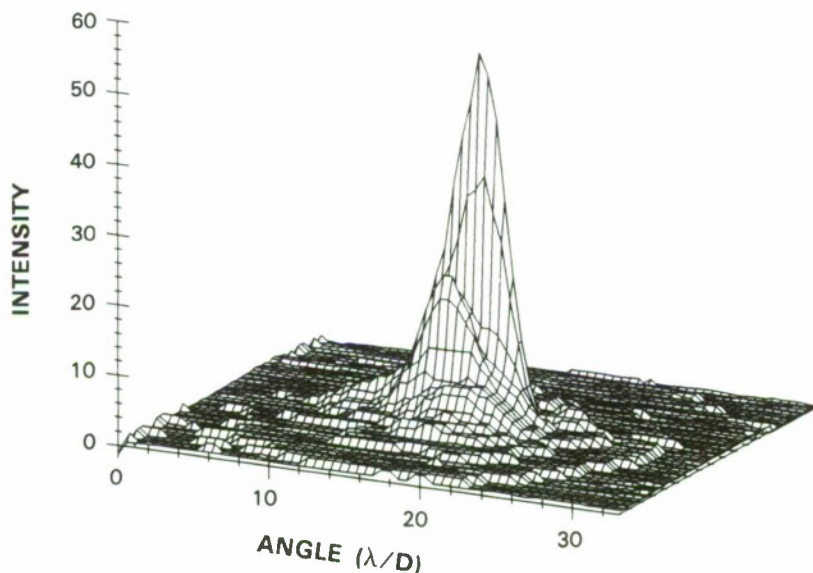
Figure 1-1. Measured far-field intensity distribution of dye laser. The beam is approximately 15 times its diffraction limit.

106458-40

1

Figure 1-2 shows the measured wavefront of the dye-laser beam during a single 2-μs pulse. The measurements were taken along a radial slice through the annular beam. Ten 200-ns wavefront measurements are shown, and one can easily see the large fluctuations occurring on the short time scale.
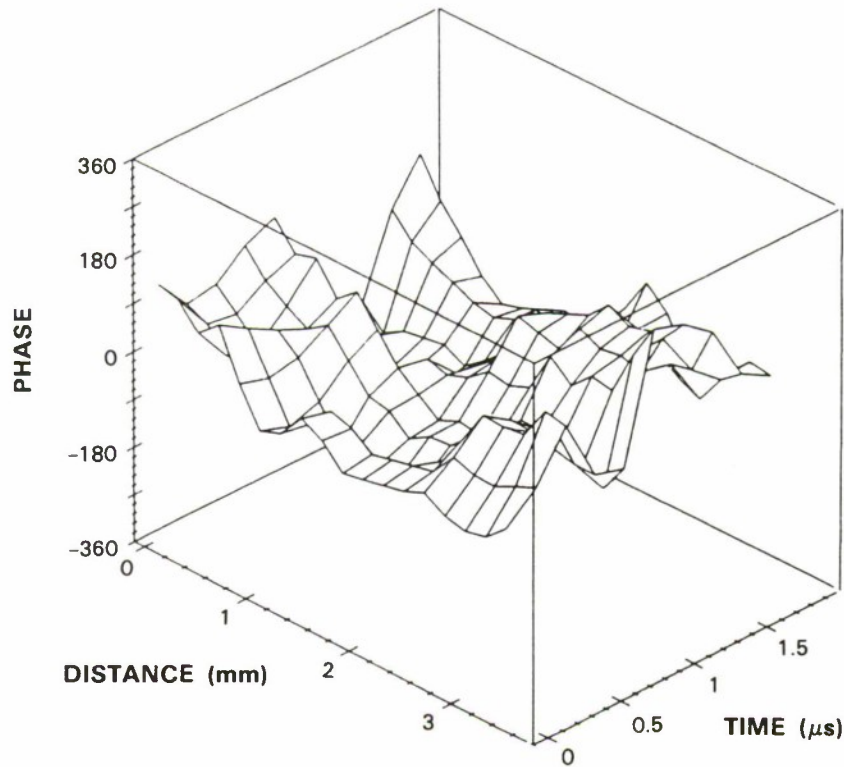
Figure 1-2.   Near-field wavefront at the output aperture of the dye laser. Ten measurements along a radial slice of the beam were made during the 2-s laser pulse.

Far-field distributions were calculated from the measured near-field phase and intensity distributions of each 200-ns interval. It was assumed in these calculations that the wavefront aberrations were cylindrically symmetric about the laser axis because the near-field measurements were made only along a radial slice of the laser beam. The time-averaged far-field pattern was calculated by adding the ten far-field intensities calculated from each of the ten measured 200-ns near-field distributions. This time-averaged intensity pattern is shown in Figure 1-3. The width of the pattern significantly exceeds the width obtained from any single 200-ns near-field distribution and is in good agreement with the directly measured time-averaged far-field pattern shown in Figure 1-1. This agreement is consistent with the assertion that the major contribution to the observed poor laser-beam quality is the temporal variation of the wavefront that occurs during the pulse. These fluctuations are believed to be due to heat produced by the absorption of pump radiation.

R.H. Rediker   T.A. Lind
B.G. Zollars   B.E. Burke
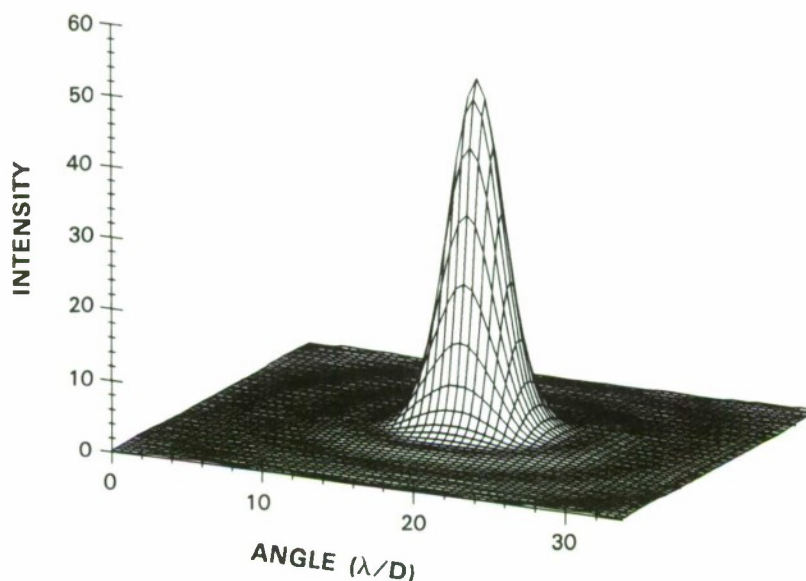
Figure 1-3. Far-field intensity distribution calculated from the measured near-field phase and intensity. Note the good agreement between this distribution and the measured far-field distribution of Figure 1-1.

1.2 GaP Microlenses by Mass Transport

We report the first observation of the mass transport phenomenon due to surface-energy minimization on GaP and the use of this phenomenon for the fabrication of high-quality microlenses. These GaP microlenses are transparent to shorter wavelengths than the previous mass-transported InP microlenses[2] and can be used for GaAs lasers and laser arrays.

In the present microlens fabrication, cylindrically symmetric multilevel mesa structures were first formed in a polished, ≈(100)-oriented GaP substrate by repeated use of photolithography and bromine-methanol etching. As shown in Figure 1-4(a), the mesa structure has six etched steps and an overall diameter of 120 μm. The step heights were designed for the desired lens profile by using the previously developed "equal-volume" design rule.[2] Then mass transport was carried out in H_2 and PH_3 flow at ≈1,000°C, the highest temperature available in our present furnace system.[3]

After an 81-h mass transport, complete smoothing of the six-step mesa structure was observed and the microlens was formed. The lens surface is very smooth except for some occasional small pits which are estimated to occupy less than a total of 0.1 percent of the lens area and are expected to have a negligible impact on the lens performance. An attempt was made to partially anneal out the surface pits in one structure, which is shown in Figure 1-4(b). The smooth lens surface has been further confirmed by examination under an interference-contrast optical microscope.

3

(a)

(b)

20 μm
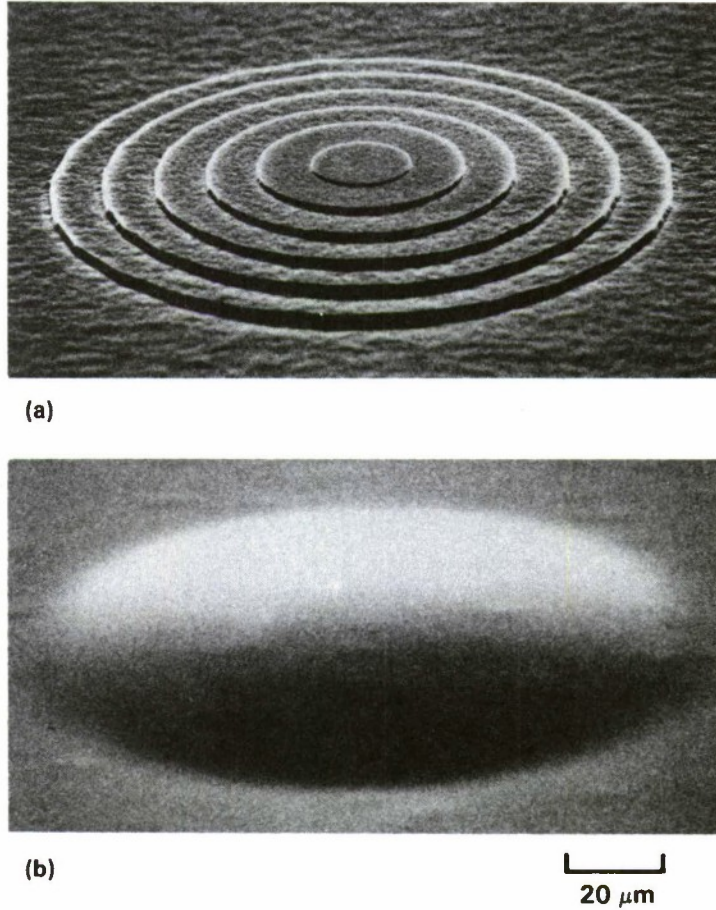
Figure 1-4.   Scanning electron micrographs of (a) an etched multilevel mesa structure in a GaP substrate, and (b) the microlens formed after mass transport.

Figure 1-5 shows stylus surface profiles of the mesa structure before and after the lens formation. The cone-shaped stylus has a small tip of ≈ 0.5-μm radius which can accurately reproduce the smooth lens profile with <0.04-μm broadening. However, relatively large broadening occurs when the stylus encounters the abrupt steps in the multilevel mesa structure, as seen in the upper part of Figure 1-5. Corrections can nevertheless be made by estimating (to within ≈ 0.5 μm) the true positions of the abrupt step edges as done in the middle part of Figure 1-5, where the profiles show a good agreement with the "equal-volume" design rule.

As shown in the lower part of Figure 1-5, the measured profile closely matches that of an ideal lens of 200-μm focal length. In the central part of the ≈ 100-μm diam., the deviations are estimated to be <0.05 μm. This result clearly demonstrates the capability of the present technique for accurately producing a desired lens profile.

4
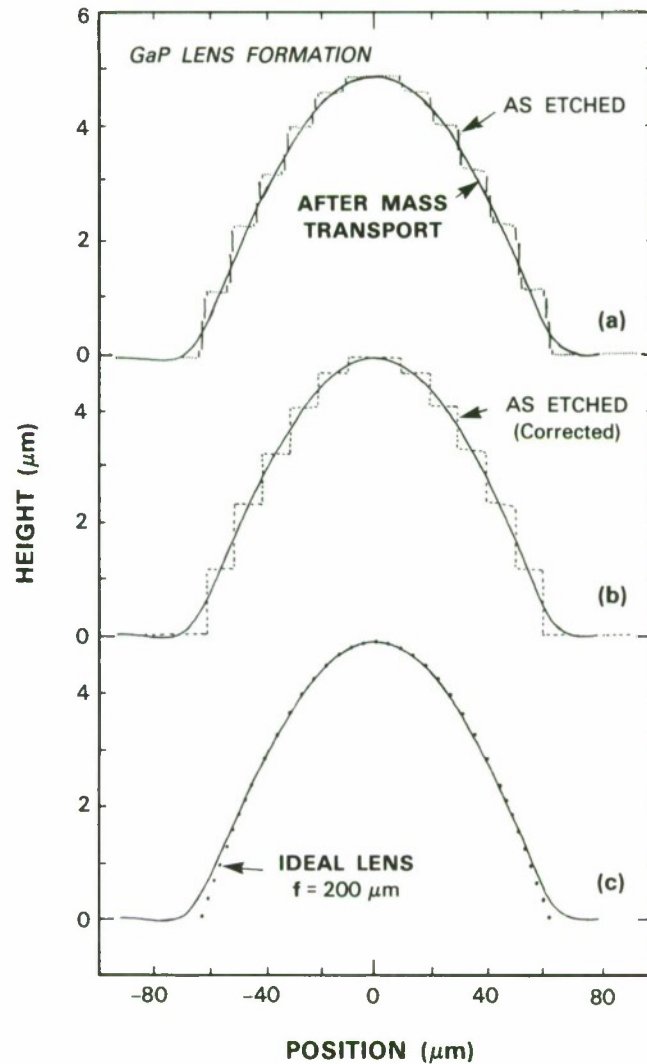
Figure 1-5. Stylus surface profiles of the mesa structure before and after mass transport. Part (a) shows the data as obtained, while part (b) shows the multilevel mesa profile corrected for the broadening caused by the size of the stylus. Part (c) compares the measured lens profile to an ideal lens profile.

Figure 1-6 shows optical micrographs of an array of GaP microlenses and the clear images formed by the light reflected from the top surface.[2] Some additional background light is seen in these photographs and is due to the transmitted light reflected back from the bottom surface. Work is underway to polish the back side and to antireflection coat both surfaces for light transmission experiments.

(a)

(b)
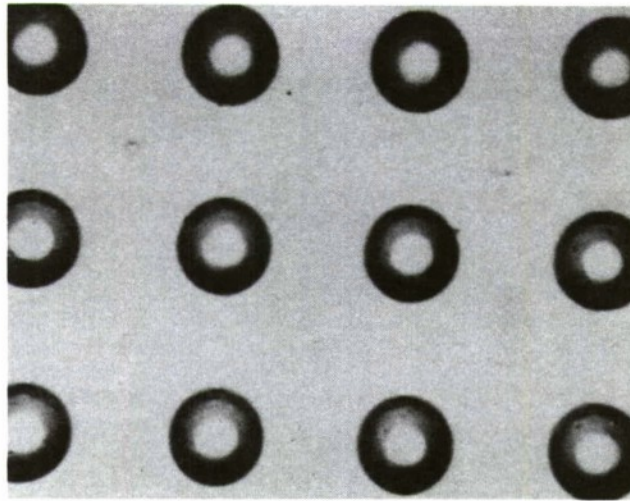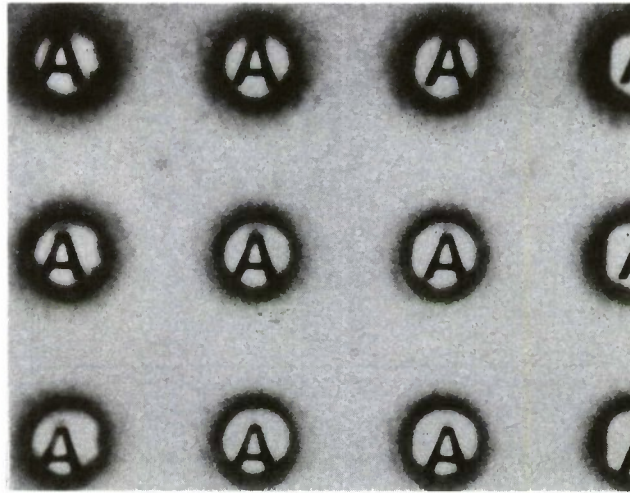
254 μm

Figure 1-6. Optical micrographs of an array of GaP microlenses, (a), and the array of images formed by the light reflected from the top surface, (b).

In conclusion, the first mass-transported GaP microlenses have been demonstrated. The present technique is capable of accurately controlling the lens profile and producing a very smooth lens surface. These high-quality microlenses are potentially useful for collimating a GaAs laser array output.

Z.L. Liau
D.E. Mull

6

1.3 A NEW OMVPE REACTOR FOR GROWTH OF InP AND RELATED ALLOYS

We report on a new type of reactor that has been developed for atmospheric pressure OMVPE growth, with special consideration given to the problems of growing materials containing indium and phosphorus. The goals for this reactor design, in addition to producing material with state-of-the-art purity and heterointerface abruptness, are to achieve uniformity within a few percent over the area of a 50-mm-diam. substrate and, with the use of substrate transfer through a loadlock, to have the capability of making many growths without disassembly of the reactor.

Figure 1-7 shows a photograph of the reactor, which has a chimney geometry (upward, parallel flow) with a sidearm added for susceptor rotation and mechanized substrate loading. The
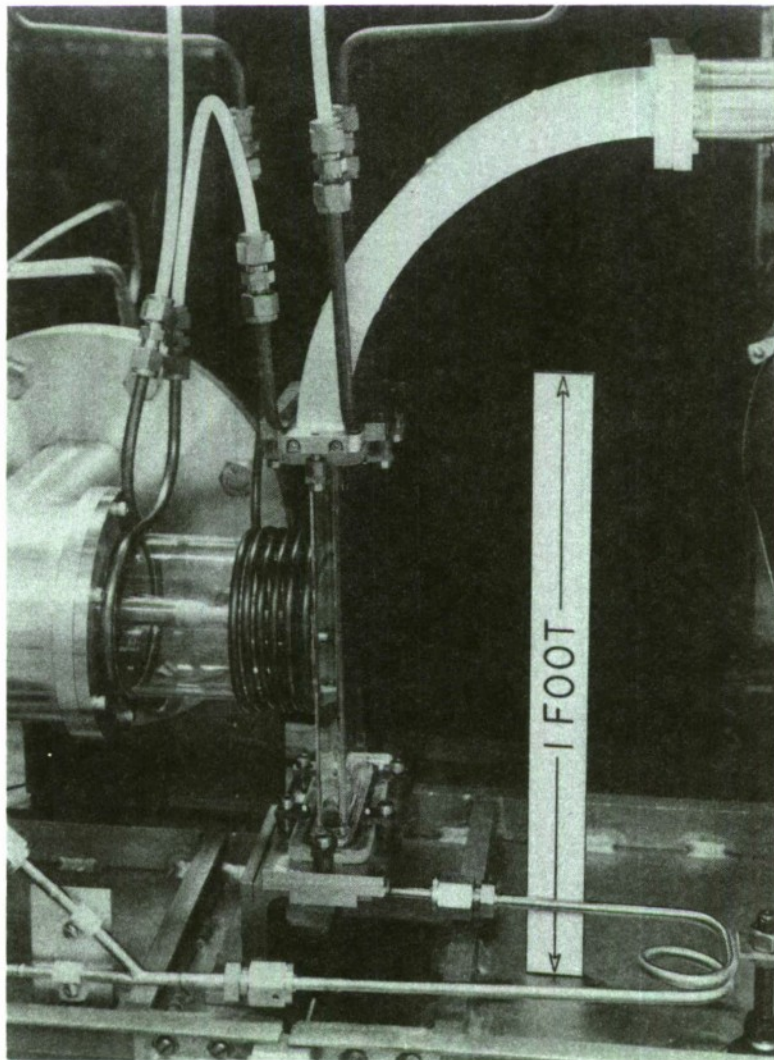
Figure 1-7. Photograph showing chimney reactor with sidearm.

body of the reactor is constructed of high-aspect-ratio (depth/width $\approx$ 8) rectangular fused silica tubing. This permits growth on 50-mm-diam. wafers with relatively high average gas velocities ($\approx$25 cm/s) at modest flows ($\approx$10 slpm). Flow visualization studies[4] and growth characterization have shown that under a wide variety of conditions, the flow in this reactor is free of vortices and convection cells, and that it is possible to select susceptor rotation rates which are high enough for growth averaging but low enough so as not to disturb the laminar flow. Also, at flows <5 slpm it is desirable to inject the gas through a large-area diffuser, but at flows above this level a simple injector which directs the gas toward the corners of the rectangle is quite adequate.

Figure 1-8 illustrates the mechanized substrate loading capability, which has been successfully used for many runs. The only exposure of the reactor to air comes when it is necessary to clean the reactor because of particulate contamination, something that occurs only after 50 μm or more of growth. Substrate removal is accomplished, under remote control, by retracting the rotation shaft with susceptor and attached substrate, then transferring to a second removal arm. Susceptor and substrate are withdrawn through a gate valve into a N_2-filled glove box. Remotely
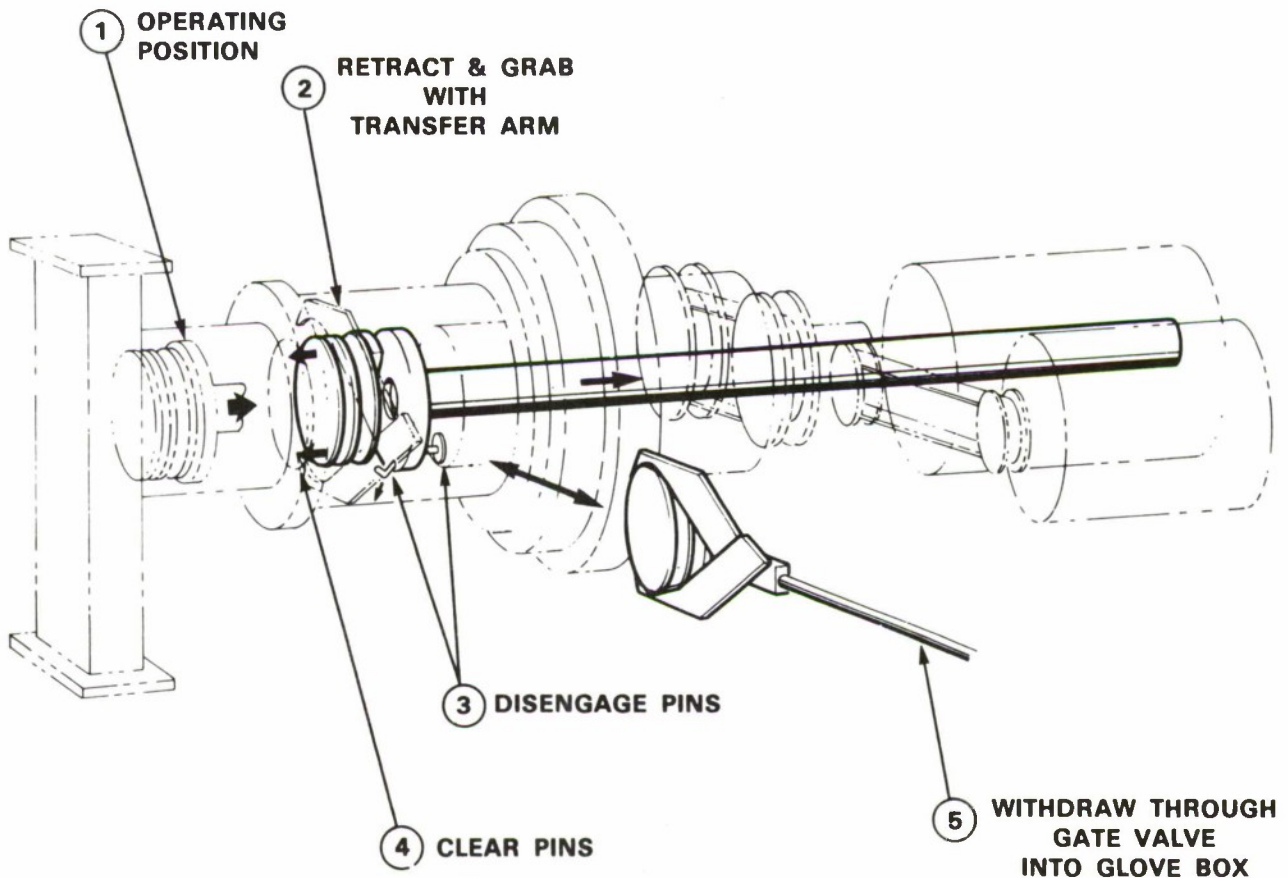
Figure 1-8. *Artist's conception of chimney reactor with rotation and substrate/susceptor transfer mechanisms.*

8

positioning the rotation and retraction mechanism relative to the growth area reduces substrate contamination and provides protection for mechanical components. The clearance between the susceptor and the reactor sidearm wall has been made no bigger than that needed for alignment and differential thermal expansion. The susceptor has been designed to reduce diffusion into the sidearm by acting as a labyrinth. With these precautions and with a flow into the sidearm $\approx 1/10$ the main flow, deposition in the sidearm is prevented and there is no detectable disruption of the main flow in the reactor.

To date, the performance of the sidearm chimney reactor has been evaluated by measuring growth deposition uniformity, first varying such parameters as flow, carrier gas composition and thermal boundary conditions, but without susceptor rotation. Then, after choosing the best values for the above parameters, the improvement brought by susceptor rotation has been determined. A technique involving growth of InP on GaAs substrates[5] has been used to evaluate deposition uniformity. This takes advantage of the low cost of GaAs substrates, compared with that of InP substrates, and of the chemical etching differences between GaAs and InP. Relatively smooth growth of InP on GaAs substrates can be obtained with a two-step process in which, first, a thin layer, 100 to 200 Å thick, is deposited at a low temperature ($\approx 400°C$) and then the remaining ≈ 1 μm of growth is made at the normal temperature ($\approx 650°C$). For growths with no rotational averaging, measurements of the thickness as a function of position typically show a decrease in thickness (or growth rate) with distance from the leading edge of the substrate. In addition, local fluctuations of several hundred angstroms (≤ 5 percent) over a distance of a few millimeters are sometimes seen. These variations can be reduced to the 1-percent range by using a baking step ($\approx 620°C$ for 10 min) to eliminate the oxide on the substrate prior to the low-temperature growth. Further reduction in the scatter can be obtained by growing thicker layers.

From the thickness uniformity measurements several conclusions have been reached: (1) At low flows, <5 slpm, thermal buoyancy forces are important. Improved uniformity can be obtained by using a dense carrier gas (fifty-fifty N_2-H_2 as opposed to H_2) and by cooling the reactor sidewall opposite the susceptor. In this regime, at a total flow of 3 slpm, leading-edge to trailing-edge variations of 35 percent or more are typically measured over 80 percent of a 50-mm-diam. wafer. (2) If the flow is increased to 7 slpm, the effects of thermal buoyancy are not seen. The H_2 carrier gas gives as good or better results than the N_2-H_2 mixture and cooling the sidewall does not help. The increased velocity reduces the systematic thickness variation to ≈ 20 percent. (3) Under these flow conditions, susceptor rotation improves the thickness uniformity by approximately a factor of ten. Figure 1-9 shows a 20-percent front-to-back variation reduced to less than a 2-percent radial variation by susceptor rotation. Additional improvements in uniformity can be achieved with higher gas flows; for example, at a flow of 14 slpm the radial variation is ≈ 1.5 percent. Further details of the thickness characterization have been presented and are in preparation.[6,7] Also included in Reference 7 is the report of our success at growing undoped InP with N_d-$N_a \approx 1 \times 10^{15}$ cm^{-3} and $\mu_{77} \approx 6 \times 10^4$ cm^2/V-s. At present, work is being undertaken to characterize this reactor for growth of InGaAsP alloys.

S.H. Groves   D.L. Hovey
S.C. Palmateer   A. Napoleone
J.W. Caunt

9
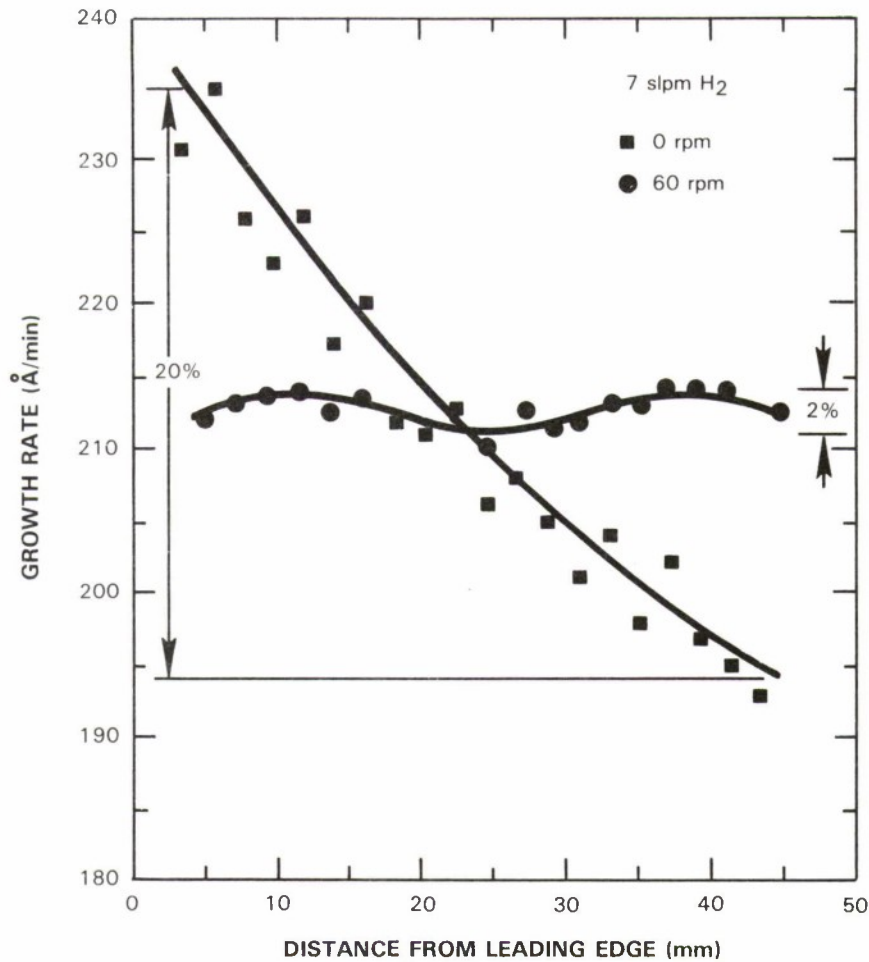
Figure 1-9.   Growth rate vs position with and without susceptor rotation for 7 slpm total flow with H_2 carrier gas.

1.4   MICROCHANNEL HEAT SINKS FOR TWO-DIMENSIONAL HIGH-POWER-DENSITY DIODE LASER ARRAYS

Semiconductor microchannel heat sinks have been proposed and demonstrated for heat extraction under conditions of high heat flux.[8-13] In this technology, water is forced through rows of small channels located within a few hundred micrometers of active devices fabricated on the surface of semiconductor wafers. The first application of this technology for cooling two-dimensional diode laser arrays is reported here.

The laser array and the heat sink were fabricated in different materials and subsequently bonded together. The array was fabricated in GaInAsP/InP with monolithically integrated beam deflectors to obtain light emission perpendicular to the surface of the wafer, as previously reported.[14] The dimensions and construction of the heat sink can be seen in the cross-sectional

10

view shown in Figure 1-10. Si was chosen for the heat sink because it is easily machined, has relatively high thermal conductivity, and has a thermal expansion coefficient close to that of InP. The channels (400 μm deep, 100 μm wide, and separated by 100 μm) were cut in 575-$\mu\pi$m-thick Si wafers with a wafer-dicing saw. A second Si wafer was soldered to each of these wafers to cover the channels and form the heat sink. The top of the heat sink was metallized and the laser array soldered to it. The heat sink was then mounted in an aluminum manifold and water forced through the microchannels at a pressure of 517 kPa (75 psi) and a flow rate of 20 cm^3/s.
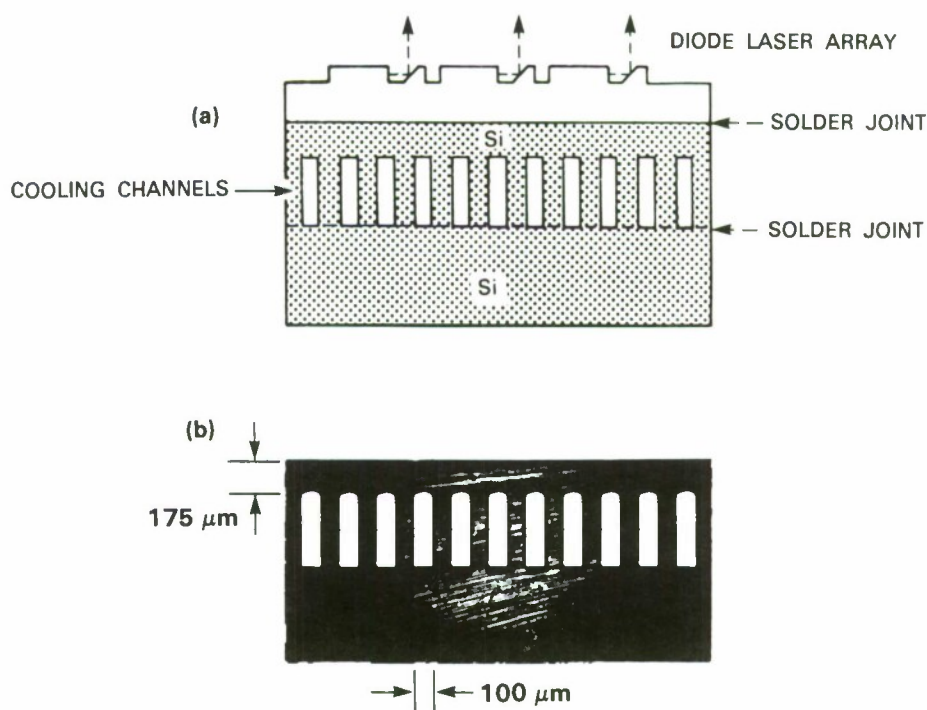
Figure 1-10. (a) Schematic illustration of the cross section of the microchannel heat sink with a surface-emitting diode laser array bonded to it, and (b) a photograph of the cross section of a Si microchannel heat sink showing typical dimensions.

The surface-emitting laser array used to characterize the heat sink consisted of 41 rows of lasers with four lasers in each row, with a row spacing of 100 μm and a row length of 1.02 mm. The laser array area ($\approx$0.04 cm^2) was considerably less than that of the heat sink (1 cm^2). The four lasers in the center row were electrically bonded together and were calibrated as the thermometer to measure the wafer temperature rise due to the heat load of the other lasers. The effective threshold current for the four lasers vs temperature was determined by observing the derivative of the L-I characteristic as the temperature of the cooling water was varied from 11 to 36°C, with no current supplied to the other lasers. This measured temperature dependence can be seen in Figure 1-11. With the coolant temperature set at either 11 or 21°C, threshold currents

11
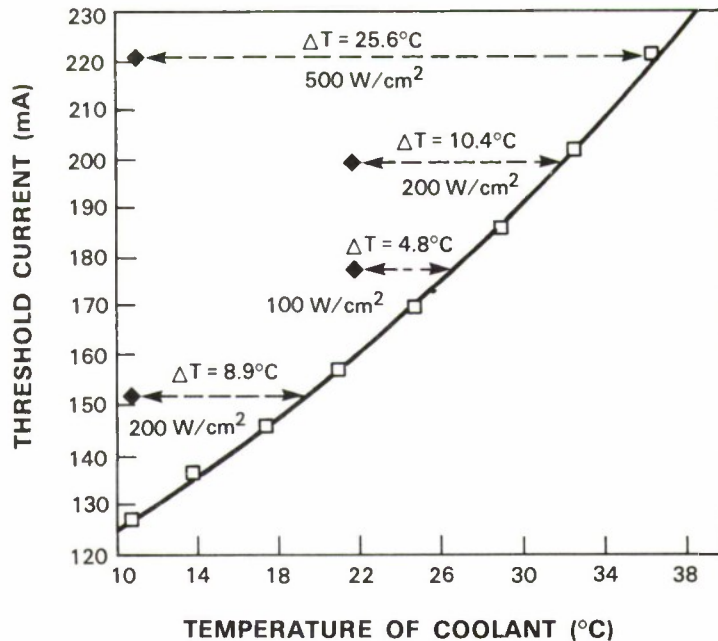
Figure 1-11. The effective threshold current of the test row of diode lasers vs the temperature of the coolant. The open squares are the calibration data points taken with no other heat load on the heat sink. The solid squares are data taken with the power dissipation in the diode laser array as indicated.

were then measured for the test array with different heat loads (up to 500 W/cm^2), produced by biasing the adjacent 40 rows of lasers. The temperature increase due to the heat load from the other lasers was determined from the change in the coolant temperature needed to give the same threshold current in the absence of heat load. The data points shown in Figure 1-11 yield an average temperature rise of 0.049°C cm^2/W. However, in order to obtain the actual thermal resistance this number must be adjusted to correct for the narrow width of the array and for the fact that the test lasers were cooler than the heat-producing lasers as discussed below.

Heat spreading in the short dimension of the 41 × 4 array can be corrected for by adding an estimated 15 percent to the measured temperature rise, yielding a temperature rise of 0.057°C cm^2/W. In order to obtain the temperature rise in the active regions of the heat-producing lasers, it is useful to consider several hypothetical temperature profiles across the surface of the laser array wafer. In Figure 1-12, curve (a) represents the approximate temperature profile expected when all 41 rows of lasers are each dissipating 100 mW (≈100 W/cm^2); curve (b) indicates the profile when no power is dissipated in the center (test) row, but all others are operating; and curve (c) corresponds to the profile expected if only the test row dissipates 100 mW. Curve (b) was drawn to show a temperature rise of 5.7°C (0.057°C cm^2/W) at the position of the test array. For the linear regime of heat flow, curve (a) is given by the sum of curves (b) and (c). Thus, if we can determine the temperature rise of the test row, we can obtain the temperature rise in the heat-producing lasers and the thermal resistance of the structure. The temperature rise
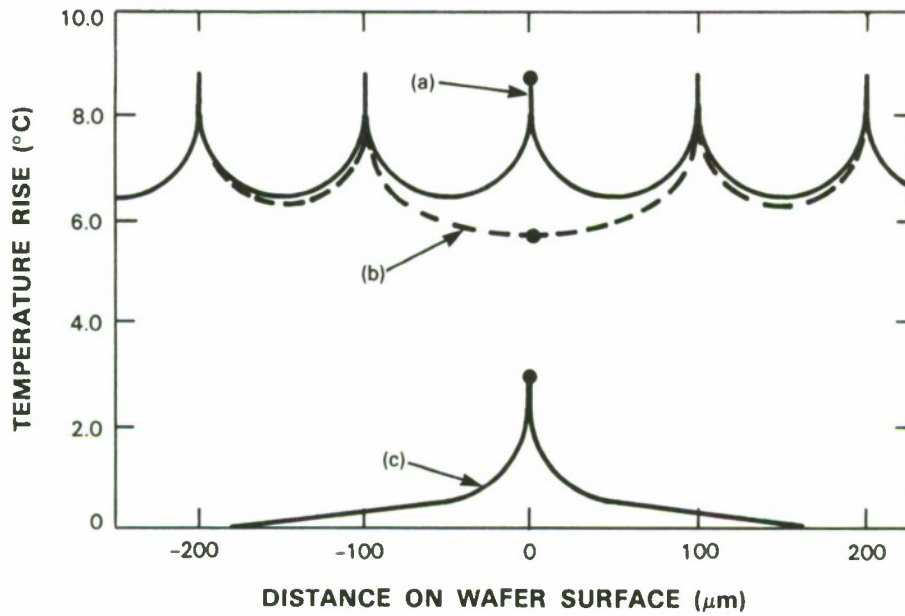
Figure 1-12. Hypothetical temperature profiles across the wafer surface, perpendicular to the laser rows, for (a) power dissipation of 100 mW in each row , (b) power dissipation of 100 mW in each row except the test row , and (c) power dissipation of 100 mW only in the test row. The solid points are taken from experimental data as described in the text.

of the test row was obtained by comparing the threshold current vs temperature obtained for CW operation (Figure 1-11) with that obtained for short-pulse operation (200-ns, 1 kHz) where heating is negligible. This measurement gave a value of 30°C/W or 3°C for 100 mW power dissipation. Adding the temperature rises deduced from the two experiments, 5.7°C and 3°C, we get an 8.7°C temperature rise in the active region of the heat-producing lasers for a power dissipation of 100 W/cm^2. Hence, the total thermal resistance is $R_{total} = 0.087°$C cm^2/W.

The thermal resistance R_{total} can be decomposed into three components: the thermal resistance R_{array} associated with heat spreading out of the 2-μm-wide active layer into the InP substrate, the thermal resistance R_{Si} associated with the Si between the InP and the top of the microchannels, and the remaining thermal resistance $R_{transfer}$ which characterizes the heat transfer process within the microchannel region (neglecting the resistance of thin metallizations and interfaces). The calculated values of R_{array} and R_{Si} are 0.039°C cm^2/W and 0.012°C cm^2/W, respectively, which when subtracted from R_{total} yields a value of 0.036°C cm^2/W for $R_{transfer}$.

In order to fully characterize the heat sink, the temperature rise of the coolant must be considered. For a typical flow rate of 20 cm^3/s, we calculate (using the heat capacity of water) a temperature rise of 0.012°C cm^2/W at the downstream end of a fully heated 1-cm-long channel. When this number is added to R_{total}, the maximum thermal resistance at the outlet is $R_{max} = 0.099°$C cm^2/W. (R_{total} is the thermal resistance at the inlet.) If we substract R_{array} from

13

R_{max} we get the maximum thermal resistance associated with the heat sink alone $R_{heat\ sink}$ = 0.060°C cm^2/W. A comparison of the present experiment with a detailed theoretical model[12, 13] is under way. The model includes a calculation of the convection cooling at the fins. The preliminary results show excellent agreement between the theory and experiment. A somewhat higher value for the maximum thermal impedance for a 1-cm^2 heat sink was extrapolated, $R_{heat\ sink}$ = 0.070°C cm^2/W.

L.J. Missaggia
J.N. Walpole
Z.L. Liau

1.5 NOVEL SCALLOPED-MIRROR DIFFRACTION-COUPLED LASER ARRAYS

The first diffraction-coupled arrays[15] of InGaAsP/InP buried-heterostructure (BH) lasers are reported. These arrays have a novel scalloped etched-mirror structure for more effective diffraction coupling. In addition, cylindrical output mirrors[16] have been incorporated to improve the array fill factor. In contrast to previous monolithic diffraction-coupled arrays, whose stripes were gain-guided or lightly index-guided,[15,17-19] the present BH laser arrays have the potential for lower threshold currents and less sensitivity to lateral spatial hole burning. Previous InGaAsP/InP BH laser arrays have been coupled by Y junctions.[20]

The structure of the present diffraction-coupled arrays is shown in Figure 1-13. The array has a set of BH laser stripes and a coupling section at one end of the cavity. The etched mirror at the end of the coupling section (which is 20 to 40 μm long) consists of a set of curved segments and resembles a scalloped shape. The curved segments approximate arcs of ellipses with the BH laser stripes located at the foci for effective coupling between adjacent stripes. To improve the fill factor, some of the arrays have at the other end a planar-waveguide output section that incorporates another set of curved mirror segments. These partially reflecting curved mirrors are centered with respect to the BH laser stripes and act as cylindrical lenses which reduce the beam divergence in the junction plane of each stripe by flattening the phase fronts of
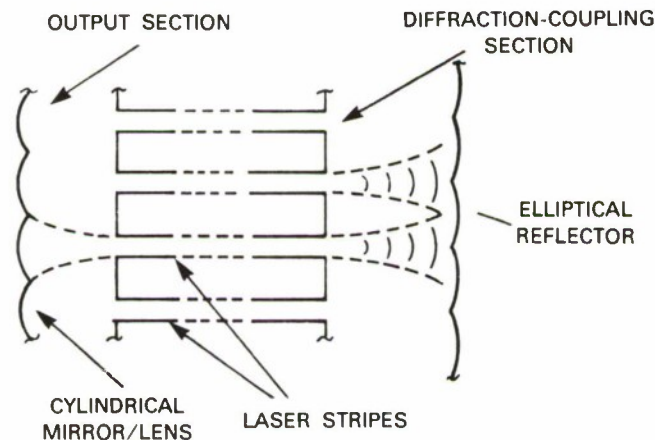
Figure 1-13. Illustration of scalloped-mirror diffraction-coupled laser array.

the diverging beams from the stripes. Little diffraction-coupling is expected to occur in the output section (which is typically 20 μm long) because the curved mirrors also partially refocus the light back into the original stripes.

The present arrays have been fabricated by a recently developed process in which the BH stripes and mirrors are formed concurrently by ion-beam-assisted etching and mass transport.[21] The curved mirror segments are therefore accurately aligned with respect to the BH stripes. The fabricated eight-stripe arrays have threshold currents between 150 and 300 mA. Figure 1-14(a) shows the far-field pattern in the junction plane of an array with a scalloped-mirror coupling section at one end. The output was taken from the other end, which has a mirror formed by cleaving through the stripes. The presence of the strong and narrow lobes in the far-field pattern shown is an indication of the strong locking between stripes that has been achieved despite the large (8 μm) stripe spacing and short (30 μm) coupling section. The observed lobe spacing of 9.5° is consistent with the stripe spacing. The full-width-at-half-maximum lobe widths are as narrow as 3°. Although the lobe widths are more than twice the diffraction limit, they are among the narrowest reported for InGaAsP/InP laser arrays. Differential quantum efficiencies of over 13 percent from a single output side have been measured just above threshold. Neither mirror was coated. Pulsed output powers as high as 100 mW have been obtained at higher currents, but with degraded far-field patterns.

Similarly strong coupling has not been achieved for arrays that have flat mirrors instead of the scalloped ones. The far-field pattern of such an array is shown, for comparison, in Figure 1-14(b). Note that the lobes in this far-field pattern are much wider and the baseline is also significantly higher compared with the pattern shown in Figure 1-14(a), which indicate the weaker locking in this array. Arrays with coupling sections of other lengths have also been investigated. The far-field patterns for arrays with 40-μm-long coupling sections were similar to those for arrays with 30-μm-long sections. However, the far-field patterns for arrays with 20-μm-long coupling sections showed weaker locking. Nevertheless, the improved locking obtained by using scalloped mirrors was still observed.

The far-field patterns shown in Figure 1-14 have many lobes because the fill factor, the ratio of the emitter size to the emitter spacing, of the BH laser array is poor ($\approx$0.2 for a typical active-region width of 1.5 μm). Improved fill factors have been achieved for arrays that have the cylindrical-mirror output sections. Figure 1-15 shows the far-field pattern for one such array. Note that the number of lobes has been greatly reduced. In addition, the intensity of the central far-field lobe is several times higher. With more optimal designs of the cylindrical-mirror segments, it should be possible to obtain single-lobe far-field patterns.

The results presented above show that strong locking can be achieved for shorter diffraction-coupling sections by using the scalloped mirrors. Use of shorter coupling sections is desirable for reduced threshold current, since the area of the coupling section (which is pumped) is reduced. In addition, there is less likelihood of instabilities that may arise for long coupling sections, which can resemble broad-area lasers. Calculations of the diffracted and reflected field profile made using the diffraction integral show that the scalloped-mirror laser array has decreased feedback
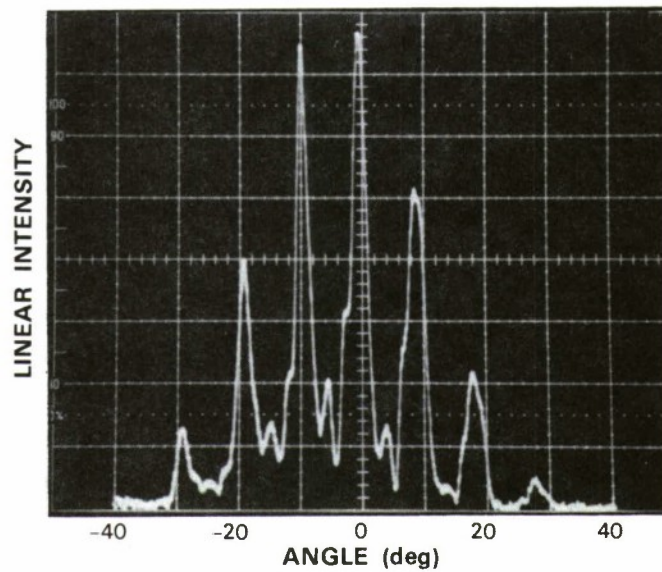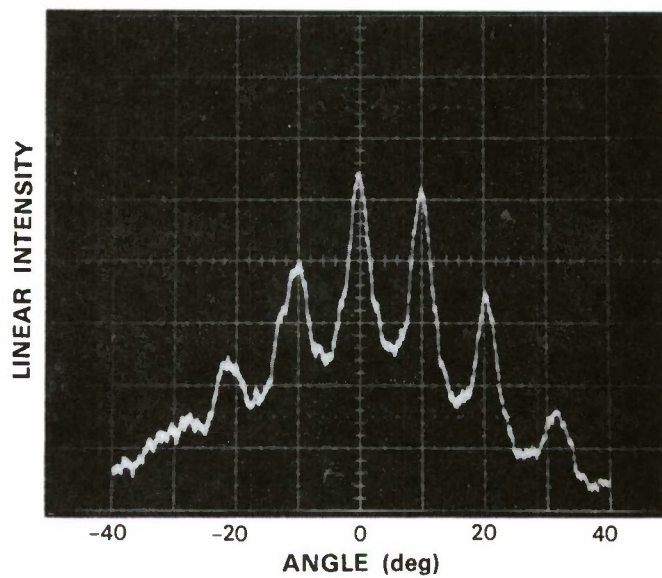
Figure 1-14. Far-field patterns (in the junction plane) from the cleaved end of diffraction-coupled BH laser arrays having (a) a scalloped mirror, and (b) a flat mirror.

16
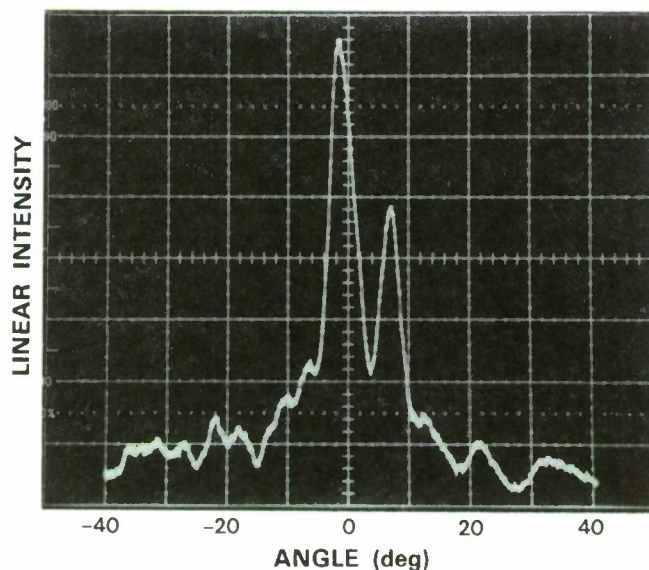
Figure 1-15. Far-field pattern in the junction plane from an array with an output section that has cylindrical mirror segments for improved fill factor.

into the same stripe and increased coupling into the adjacent stripes.[22] This improves the ability of the array to be locked despite nonuniformities between the stripes.

Scalloped mirrors can be incorporated into diffraction-coupled arrays whose stripes are also coupled through their evanescent fields or through leaky waves. The length of the diffraction-coupling sections can be designed with respect to the stripe spacing to obtain in-phase array operation rather than the 180° out-of-phase operation often preferred by the evanescent-field or leaky-wave coupling. Since the scalloped mirror yields improved coupling and reduced feedback, it can increase the effect of the diffraction coupling without the need for long or strongly pumped diffraction sections.

<div align="right">

D. Yap
J. N. Walpole
Z. L. Liau

</div>

17

REFERENCES

1. R.H. Rediker, T.A. Lind, and B.E. Burke, J. Lightwave Technol. **LT-6**, 916 (1988).

2. Z.L. Liau, V. Diadiuk, J.N. Walpole, and D.E. Mull, Appl. Phys. Lett. **52**, 1859 (1988).

3. Solid State Research Report, Lincoln Laboratory, MIT (1987:3), pp. 11-14, DTIC AD-A192837.

4. S.C. Palmateer, S.H. Groves, C.A. Wang, D.W. Weyburne, and R.A. Brown, J. Cryst. Growth **83**, 202 (1987).

5. Solid State Research Report, Lincoln Laboratory, MIT (1988:1), pp. 15-17, DTIC AD-A201044.

6. S.H. Groves, S.C. Palmateer, J.W. Caunt, and D.L. Hovey, Proc. ICMOVPE IV, Hakone, Japan, 1988, to be published J. Cryst. Growth.

7. S.C. Palmateer, S.H. Groves, J.W. Caunt, and D.L. Hovey, Electronic Materials Conference, Boulder, CO, June 1988, and in preparation.

8. D.B. Tuckerman and R. F. Pease, IEEE Electron Device Lett. **ED-2**, 126 (1981).

9. D.B. Tuckerman, Ph.D. thesis, Stanford University, 1984.

10. S. Sasaki and T. Kishimoto, Electron. Lett. **22**, 1332 (1986).

11. T. Kishimoto and S. Sasaki, Electron. Lett. **23**, 456 (1987).

12. R.J. Phillips, SM thesis, Massachusetts Institute of Technology, 1987.

13. R.J. Phillips, Lincoln Laboratory Journal **1**, 31 (1988).

14. J.N. Walpole and Z.L. Liau, Appl. Phys. Lett. **48**, 1636 (1986).

15. J. Katz, S. Margalit, and A. Yariv, Appl. Phys. Lett. **42**, 554 (1983).

16. J.N. Walpole, Z.L. Liau, L.J. Missaggia, and D. Yap, Appl. Phys. Lett. **50**, 1219 (1987).

17. T.R. Chen, K.L. Yu, B. Chang, A. Hasson, S. Margalit, and A. Yariv, Appl. Phys. Lett. **43**, 136 (1983).

18. J.J. Yang and M. Jansen, Electron. Lett. **22**, 2 (1986).

19. L.J. Mawst, D. Botez, T.J. Roth, and J.J. Yang, Electron. Lett. **24**, 570 (1988).

20. D. Yap., Z.L. Liau, D.Z. Tsang, and J.N. Walpole, Appl. Phys. Lett. **52**, 1464 (1988).

21. D. Yap, J.N. Walpole, and Z.L. Liau, Appl. Phys. Lett. **53**, 1260 (1988).

22. D. Yap, Ph.D. thesis, Massachusetts Institute of Technology, 1988.

2. QUANTUM ELECTRONICS

2.1 THREE-MIRROR Ti:Al$_2$O$_3$ RING LASER CAVITY

A commonly used cavity geometry for Ar-laser-pumped Ti:Al$_2$O$_3$ lasers is shown in Figure 2-1. (Ignore, for the moment, the path sketched for the beam inside the cavity.) The curved folding mirror M_f is used to compensate for the astigmatism due to focusing through the Brewster-angle-cut Ti:Al$_2$O$_3$ crystal.[1] The focus of the folding mirror must be close to the center of curvature of the pump-side end mirror M_p. For normal (standing wave) cavity operation, the distance D_{fo} between the folding mirror and the (flat) output mirror M_o is not critical, as the beam is approximately collimated in this region. However, if this distance is chosen so that the pump mirror is *imaged* by the folding mirror onto the output mirror, the cavity becomes degenerate[2]; any ray retraces itself after one complete round-trip. The imaging condition is (neglecting astigmatism)

$$1/D_{fo} + 1/D_{fp} = 2/R_f \qquad , \tag{2-1}$$

where R_f is the radius of the folding mirror and the distances D_{fo} and D_{fp} are defined in Figure 2-1. Because the actual mode path must find a gain region in the active medium, the laser
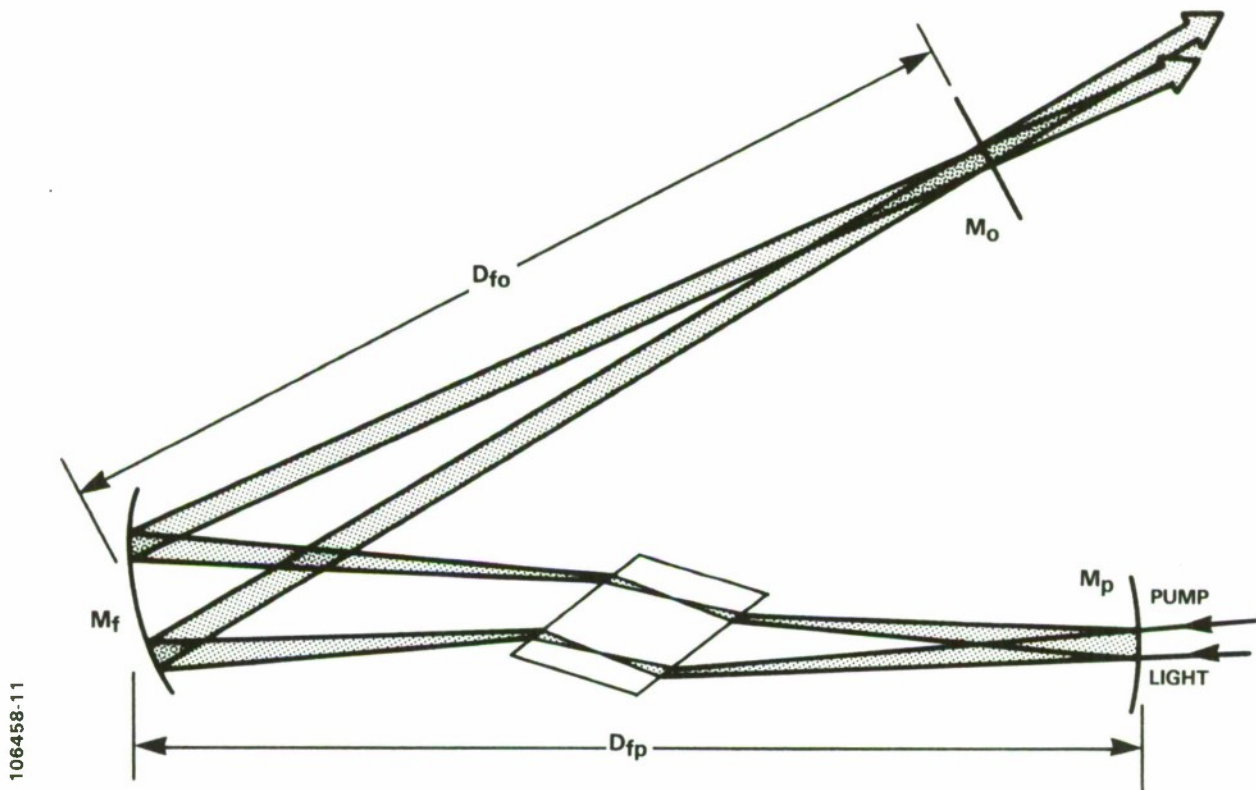
Figure 2-1. Astigmatically compensated laser cavity. The beam path is shown for the case where the cavity is degenerate and pumped off-axis.

19

beam position and Gaussian parameters are determined by the pump beam. The same cavity can be operated in a linear configuration (when the pump beam travels along the cavity axis, the standard alignment condition) or, by displacing the pump beam, in a ring configuration utilizing two distinct regions of the folding mirror, as shown in Figure 2-1. The figure shows the path of the infrared laser beam in the cavity; because of absorption in the crystal and transmission through the mirrors, the blue-green pump beam effectively passes through the crystal only once and, therefore, can pump only one of the two regions in the crystal traversed by the laser beam.

Experiments have been performed on a Ti:Al$_2$O$_3$ laser with the geometry of Figure 2-1. The pump and folding mirrors have radii of R_p = 10 cm and R_f = 25 cm, respectively, so that $D_{fp} = R_p + R_f/2 = 22.5$ cm. This requires a separation D_{fo} between folding and output mirrors of ≈ 28 cm for Equation (2-1) to be satisfied. The output mirror was mounted on a translation carriage so that its position could be varied along the cavity axis. The cavity was aligned in the conventional way for linear (on-axis) operation, with a lasing threshold of 1.8 W. The effect of a lateral translation of the pump beam was measured as an increase in threshold for varying values of the distance D_{fo}. For values of D_{fo} far from the imaging value, the threshold rose steeply with pump misalignment; the pump beam had to be within 0.1 mm of the cavity axis for lasing to be possible at all. However, when the output mirror was within 5 mm of the imaging position,
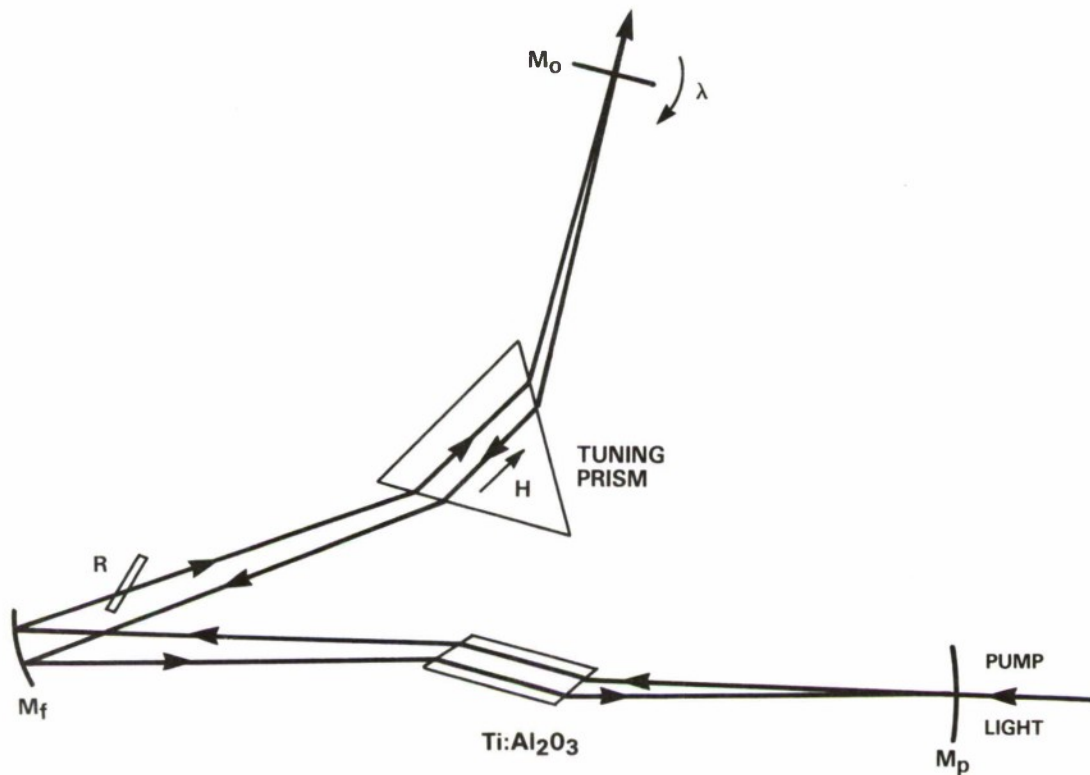
Figure 2-2. Mechanically tunable traveling-wave cavity. $\vec{H}$ is the magnetic field inside the tuning prism.

a translation of the pump beam raised the threshold to only 3.7 W. This increase remained approximately constant for pump beam displacements up to around 2 mm. The approximate doubling of the threshold from its on-axis value corresponds to halving the gain path over one round-trip (Figure 2-1), and is also an indication of low parasitic absorption in the 1.7-cm Ti:Al$_2$O$_3$ crystal.[3]

Since the two arms of the laser path in the cavity can be separated by several beam diameters (4 mm is easy to obtain), it is possible to insert nonreciprocal optics (an optical diode) in one arm to obtain unidirectional traveling-wave operation. Figure 2-2 shows a mechanically tunable cavity with a Brewster-angle quartz optical rotator, labeled R (of the type used in ring dye lasers). To complete the optical diode, a magnetic field is applied to the tuning prism. Since the latter is made of heavy flint glass and is traversed twice by the laser radiation, the fringing field from a magnet held above the prism generates sufficient Faraday rotation to ensure traveling-wave operation. The degree of suppression of the unwanted wave is measured by comparing the intensity of the two output beams, separated by about 1°. Ratios of 1:2,000 or better are typically obtained.

The cavity described here has the same configuration as a standard linear cavity, and can indeed be operated as such for initial alignment. It therefore lends itself to interferometric coupling with a side arm containing fine-tuning optics as previously described.[4] Work along these lines is underway with the goal of electrooptic, single-mode selection.

<div align="right">

V. Daneu
J.L. Daneu

</div>

2.2 FEMTOSECOND Ti:Al$_2$O$_3$ INJECTION-SEEDED LASER

A Ti:Al$_2$O$_3$ amplifier has a very wide (200 nm) gain bandwidth[5] and thus has excellent potential for amplifying and tuning femtosecond laser pulses.[6] We have used a Ti:Al$_2$O$_3$ injection-seeded laser, pumped with a 5-mJ copper-vapor laser, to amplify the output of a synchronously pumped, mode-locked dye laser. From a 0.1-pJ, 440-fs seed pulse at 790 nm, a 1-μJ, 1.2-ps output pulse is generated. These pulses have been recompressed with a grating pair to 275 fs.

Figure 2-3 is a schematic of the Ti:Al$_2$O$_3$ injection-seeded laser. A CW, mode-locked Nd:YAG laser generates 90-ps pulses at 12-ns intervals. The pulses are shortened to 5 ps in a fiber-grating compressor. These pulses are frequency doubled in KTP to generate 4-ps pulses at 532 nm, with a pulse energy of 1 nJ. An acousto-optic modulator (AOM) in the beam path before the compressor is used to maintain constant intensity in the second harmonic. This light pumps a dye laser whose cavity length is matched to the 12-ns pulse spacing. The dye laser is tuned with a birefringent filter.

A single pulse from the 82-MHz output train of the dye laser is selected with an AOM. The single-pulse selection operates at a 4-kHz repetition rate, synchronized to the 82-MHz dye-laser pulses and is used to trigger the copper-vapor laser. The pulse is transmitted through a
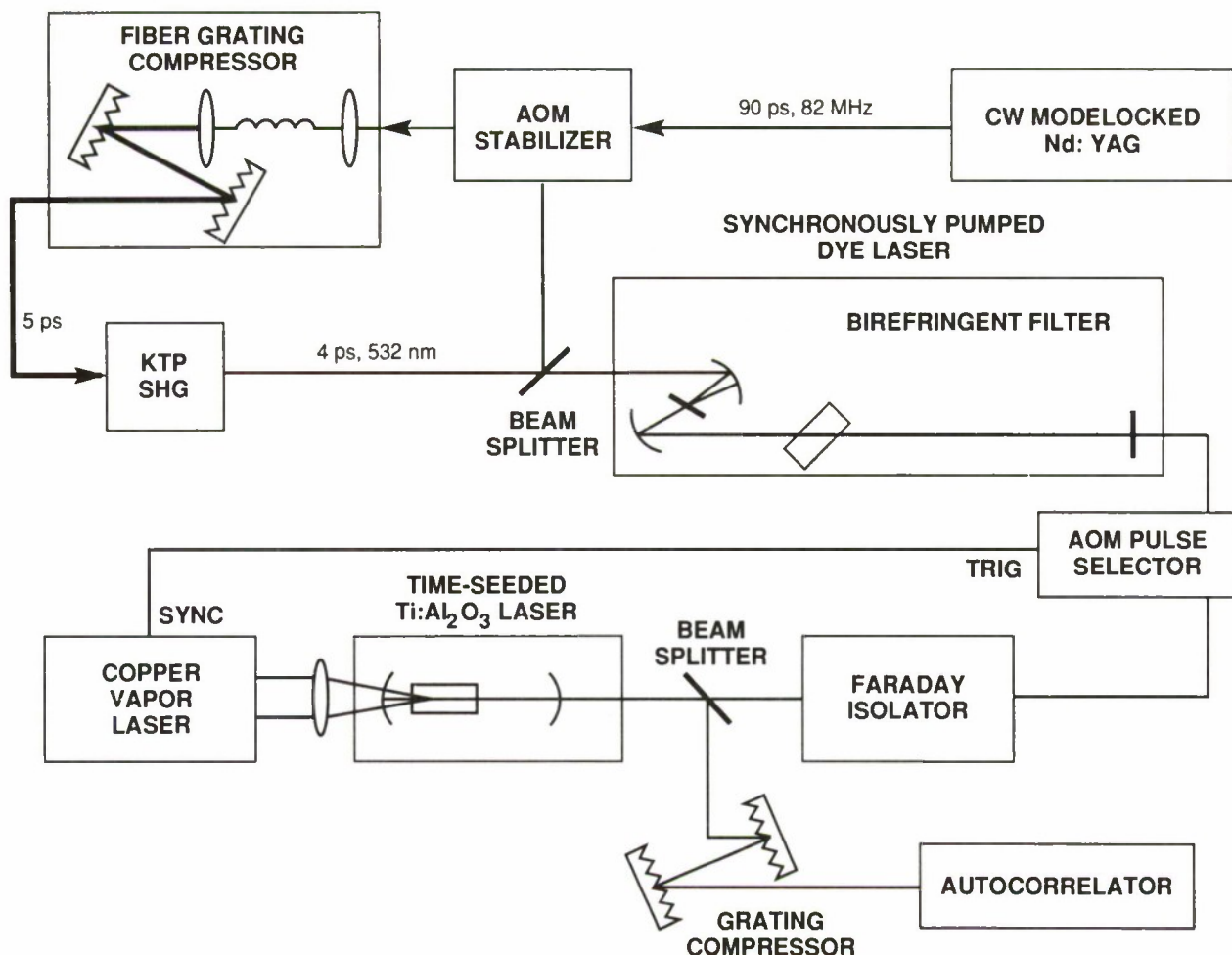
Figure 2-3.   Schematic of Ti:Al₂O₃ injection-seeded laser. A synchronously pumped, mode-locked dye laser provides subpicosecond pulses. After selection and isolation, these pulses are used to seed a Ti:Al₂O₃ laser pumped with a copper-vapor laser. The output is recompressed with a grating pair.

wavelength-independent Faraday isolator,[7] which protects the AOM pulse selector from the high power $Ti:Al_2O_3$ laser output. The wavelength-independent Faraday isolator passively provides good isolation over the 200-nm gain spectrum of the $Ti:Al_2O_3$ laser. Thus, it protects the pulse selector at the seeded frequency and at other frequencies where the $Ti:Al_2O_3$ laser operates when no seed pulse is present.

The $Ti:Al_2O_3$ laser consists of a 7-mm-long $Ti:Al_2O_3$ crystal (with a 3×3 mm cross section) between two mirrors 33 cm apart. It is pumped with a 5 mJ/pulse copper-vapor laser operating at 4 kHz. The pump light is polarized in the direction of optic axis of the $Ti:Al_2O_3$ and focused onto the crystal with a lens of 30-cm focal length. It enters the cavity through a dichroic mirror with a 25-cm radius of curvature. Approximately 1 mJ is absorbed in the crystal. The seed pulse

is mode-matched to the output of the Ti:Al$_2$O$_3$ laser using a telescope and coupled into the cavity through the output coupler. The output coupler has a 15-cm radius of curvature and transmits 8 percent at the lasing wavelength.

With no seed pulse, the output is a gain-switched pulse delayed by 150 ns after the pump pulse, as shown in Figure 2-4. This output builds up from spontaneous emission. With a 1-pJ seed pulse,[8] the seed pulse is amplified and saturates the gain after 130 ns. At that time there is an order of magnitude less energy in the nascent lasing than in the amplified seed pulses. The net output energy is the same with or without seeding, 100 μJ. Thus, nearly all of the energy is in the amplified pulses.
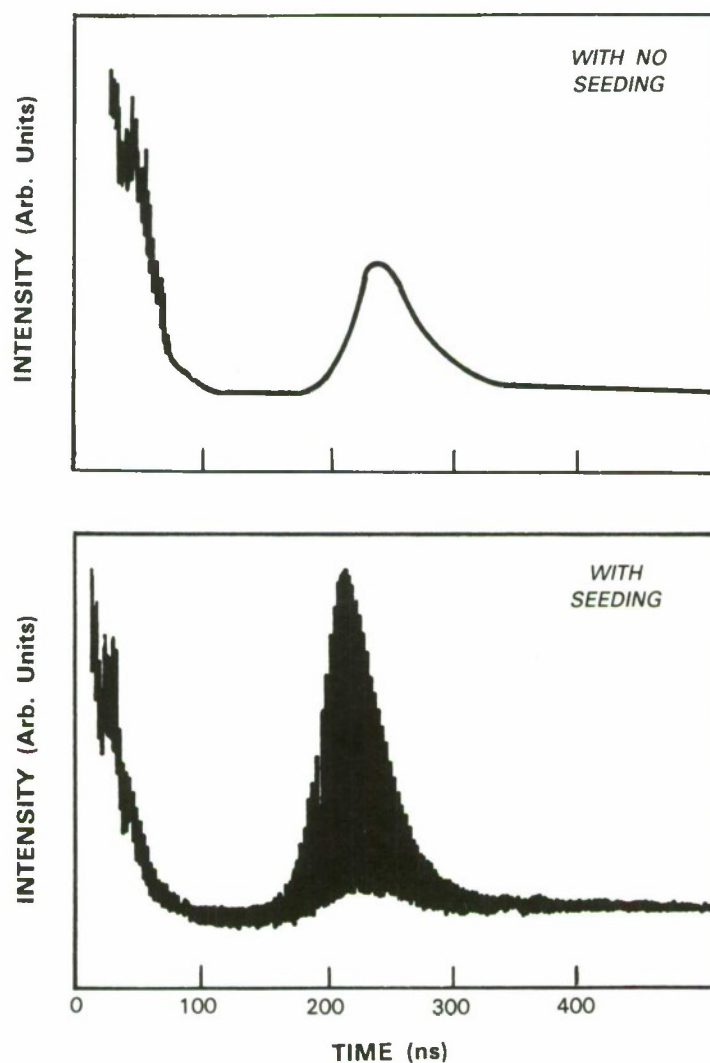
Figure 2-4.   Ti:Al$_2$O$_3$ laser output with and without injection seeding. Zero time corresponds to the pulse from the copper-vapor laser. The seed pulse is injected within the first few nanoseconds. During the 200-ns interval between input and output, the input pulse is amplified.

23

An expanded view of the Ti:Al$_2$O$_3$ laser output with seeding is shown in Figure 2-5. The cavity round-trip time of 2.2 ns is clearly seen. From the first to the fourth pulse there is a net amplification of a factor of 2.8, giving a round-trip gain of 1.4, consistent with previous gain measurements[9] and the known cavity parameters. The detector and electronics limit the width of the pulses and cause the small ripples after each pulse.

The mode-locked pulses from the dye laser have an autocorrelation width of 0.44 ps, as shown in Figure 2-6. The Ti:Al$_2$O$_3$ output pulses have a width that depends on the number of round-trips in the Ti:Al$_2$O$_3$ laser cavity. The pulse duration as a function of time delay after the firing of the copper-vapor laser is obtained with a boxcar integrator. The pulse duration is found to increase nearly linearly with time delay, with a slope of 5×10^{-6}. This slope is in good agreement with the slope expected form the dispersion of sapphire (6×10^{-6}).

The highest energy output pulses, which individually contain ≈ 1 μJ of energy, can be compressed using a double-pass, two-grating pulse compressor. These compressed pulses are measured to have an autocorrelation width of 0.275 ps and are even shorter than the input pulses. This is a result of the input pulses having a frequency chirp, so that they could have been compressed prior to seeding.
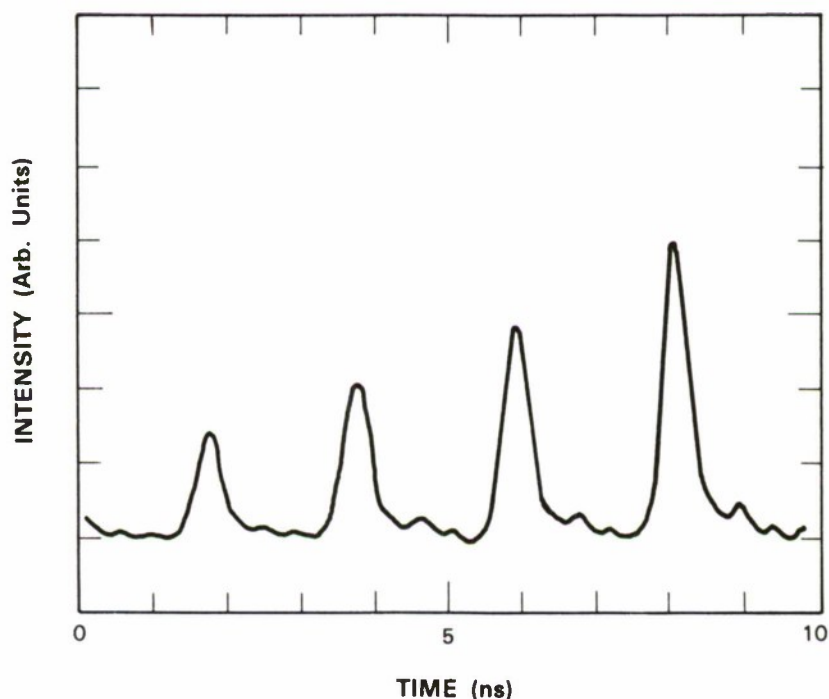
Figure 2-5.   Expanded view of the Ti:Al$_2$O$_3$ laser output. The laser pulses are amplified during each round-trip of 2.2 ns.

24
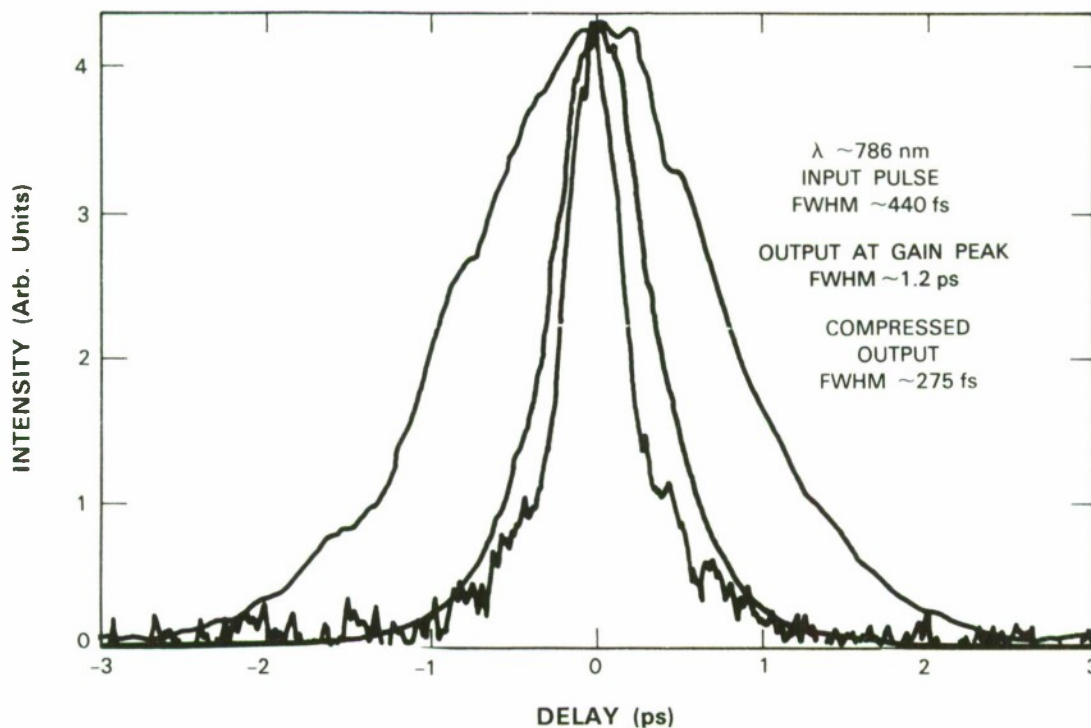
Figure 2-6. Autocorrelation traces of the seed pulse, output pulse, and compressed output pulse. The full widths at half-maximum are 440 fs, 1.2 ps, and 275 fs, respectively. The autocorrelator consists of a computer-controlled optical delay line and a noncollinear second harmonic generator. The doubled output is filtered and detected with a photomultiplier to obtain a background-free autocorrelation trace.

In conclusion, the energy of a 440-fs, 0.1-pJ pulse from a dye laser has been increased by a factor of 10^7 in a $Ti:Al_2O_3$ laser pumped by a copper-vapor laser. The 1.2-ps, 1-μJ output pulses have been compressed to 275 fs.

P.A. Schulz   M.J. LaGasse

R.W. Schoenlein   J.G. Fujimoto

2.3 END-PUMPED $Nd:LaF_3$ and $Nd:LaMgAl_{11}O_{19}$ LASERS

Both $Nd:LaF_3$ and $Nd:LaMgAl_{11}O_{19}$ (Nd:LMA) are of interest for diode-laser-pumped solid state lasers. Both materials have broader absorption bandwidths and longer upper-state lifetimes than Nd:YAG, and neither material has been thoroughly characterized. To characterize these materials, CW end-pumped laser oscillators of each material were excited by the output of a CW $Ti:Al_2O_3$ laser, as shown in Figure 2-7. Poor performance under these conditions would be an indication that there are difficulties with these materials for use with diode-laser pumping.

25
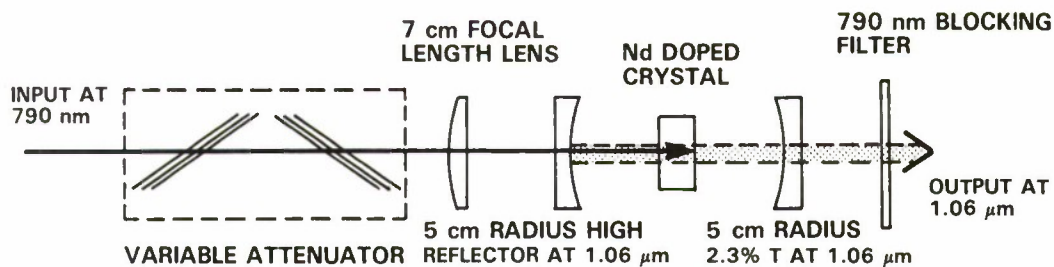
Figure 2-7. Experimental apparatus for end-pump Nd:LaF₃ and Nd:LMA lasers.

The LaF$_3$ sample is doped with $\approx$1 at.% Nd; the LMA sample is doped with $\approx$10 at.% Nd. Both samples are single-layer antireflection coated with MgF$_2$ for 1.06 μm. In the case of LaF$_3$ this coating is not optimum given the refractive index of MgF$_2$, resulting in a residual reflection at the surface of 0.6 percent. The pump wavelength in both cases is $\approx$790 nm. The cavity consists of two mirrors with 5-cm radius of curvature, separated by 9.5 cm. The output is taken through a 2.3-percent transmitting mirror.

Figure 2-8 shows the output power near 1.06 μm as a function of absorbed input power at 790 nm for both samples. The observed slope efficiency of 47 percent for Nd:LaF$_3$ is comparable with that observed in other end-pumped Nd^{3+} lasers. Even higher slope efficiencies may be possible with better antireflection coatings. The slope efficiency of 31 percent for the Nd:LMA sample is clearly below that of other Nd^{3+} lasers, but it is consistent with the slope efficiency observed in similar experiments with this material.[10]
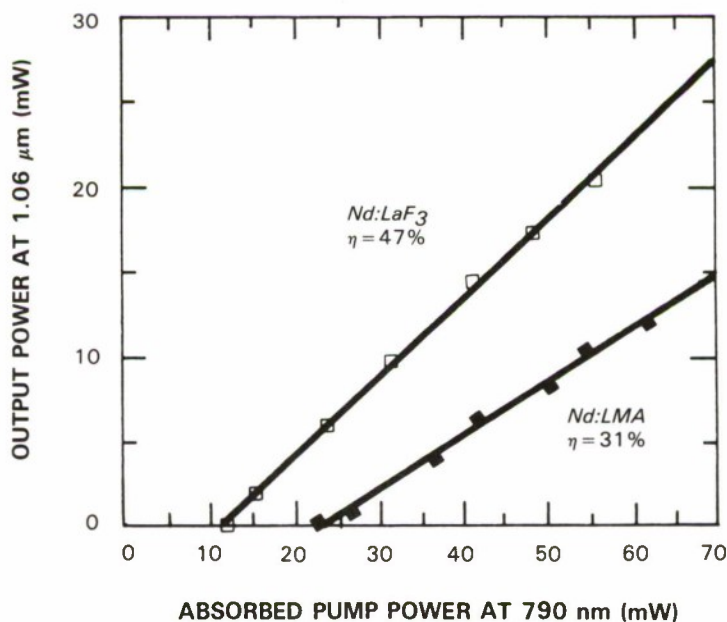
Figure 2-8. Output power as a function of absorbed pump power for the Nd:LaF₃ and Nd:LMA lasers. The slope efficiency η is 47 percent for Nd:LaF₃ and 31 percent for Nd:LMA.

26

There are at least three possible reasons for the low slope efficiency in Nd:LMA, all of which are undesirable for diode-laser pumping. One is large loss in the sample at the lasing wavelength. This does not appear to be the reason since when the output mirror is changed to a high reflector at 1.06 μm, the reduction in the lasing threshold is consistent with low loss. The other possibilities are excited-state absorption of the pump radiation or of the lasing radiation. The cause appears to be the latter of these two. Based on preliminary absorption spectra from the ground-state manifold, there are energy levels that are in resonance for absorption of a photon at the lasing wavelength by an ion in the upper laser level. There appear to be no energy levels in resonance for absorption of a pump photon by an ion in the upper laser level. If this interpretation is correct, then Nd:LMA is not a good choice for the gain medium for a diode-pumped laser. On the other hand, efficiencies comparable to Nd:YAG have been obtained in Nd:LMA with lamp pumping.[11] In this case, the heavier doping of Nd:LMA and broader absorption features allow for a higher pump efficiency under broadband excitation. This can overcome the power loss due to excited-state absorption at the expense of increased thermal loading of the gain medium.

In summary, laser experiments have been performed using Nd:LaF$_3$ and Nd:LMA as the gain media. Nd:LaF$_3$ performed as expected and appears to be a good candidate for diode-laser pumping. Nd:LMA showed poorer performance than expected. The poor performance is attributed to excited-state absorption at the lasing wavelength. Thus, Nd:LMA does not appear to be a promising candidate for diode-laser pumping.

<div align="right">

T.Y. Fan
W.E. DeFeo

</div>

2.4 SINGLE-FREQUENCY MICROCHIP Nd LASERS

Single-frequency microchip lasers use a miniature, monolithic, flat-flat, solid-state cavity whose mode spacing is greater than the medium gain bandwidth.[12] They rely on gain-guiding or nonlinear optical effects to define the transverse dimensions of the lasing mode. As a result, the fabrication process for the microchip lasers lends itself to mass production. Because of the small amount of material used for each laser and the simple fabrication, the cost per laser is extremely low. Once created, the microchip lasers are longitudinally pumped with the close-coupled, unfocused output of a diode laser.

To demonstrate the feasibility of diode-pumped microchip lasers, several different lasers were constructed and operated CW at room temperature. These included Nd:YAG (Nd$_x$Y$_{3-x}$Al$_5$O$_{12}$) at 1.06 μm using a 730-μm-long cavity, Nd:YAG at 1.3 μm using a 730-μm-long cavity, Nd pentaphosphate (NdP$_5$O$_{14}$) at 1.06 μm using a 100-μm-long cavity, and Nd:GSGG (Nd$_x$Gd$_{3-x}$ Sc$_2$Ga$_3$O$_{12}$) at 1.06 μm using a 625-μm-long cavity. In each case, single-longitudinal-mode, single-transverse-mode operation was achieved with pump powers many times above threshold.

The rest of this report will discuss the performance of the 1.06-μm Nd:YAG microchip lasers. These lasers were constructed from a slab of YAG with 1.1 wt% Nd doping. The slab was

cut and polished to a thickness of 730 μm. Dielectric cavity mirrors were deposited directly onto the YAG. On earlier microchip lasers the mirrors were cut from 100-μm-thick wafer mirrors and then bonded to the Nd:YAG.[12] The performance of the earlier devices was very similar to the performance of the dielectrically coated Nd:YAG cavities. The output mirror had a reflectivity of 99.7 percent at 1.06 μm and was designed to reflect the pump light. The opposite mirror had a reflectivity of 99.9 percent at 1.06 μm and transmitted the pump. The Nd:YAG was cut into pieces 1 mm square (or less) and bonded to a sapphire heat sink.

A Ti:Al$_2$O$_3$ laser was used as a pump source to characterize the microchip lasers prior to diode pumping. It was tuned to the Nd:YAG absorption peak at 0.809 μm and focused onto the microchip laser, with an experimentally determined spot size of about 50 μm in the Nd:YAG crystal. When the Nd:YAG microchip lasers were properly aligned with the pump, the lasing threshold was measured to be below 1 mW, and the slope quantum efficiency (determined from the output of the laser from the 99.7-percent reflecting mirror only) was slightly greater than 30 percent. The highest single-mode CW output power achieved with the microchip lasers was 22 mW. Only single-longitudinal-mode, single-transverse-mode operation was observed from threshold (1 mW) up to 40 times threshold. The output beam was circularly symmetric with a divergence of about 20 mrad, determined by the spot size of the pump. In contrast to results reported elsewhere,[13] the output of the microchip lasers was polarized to better than 1 part in 100.

The linewidth of the Nd:YAG microchip lasers was measured by heterodyning two free-running devices. Thermal tuning was used in order to get the lasers to operate at nearly the same frequency. The outputs of the lasers were stable enough to obtain heterodyne measurements with a resolution of 10 kHz. At this resolution, the measured spectral response was instrument limited, as shown in Figure 2-9. This gives a linewidth for the microchip lasers of <5 kHz, assuming
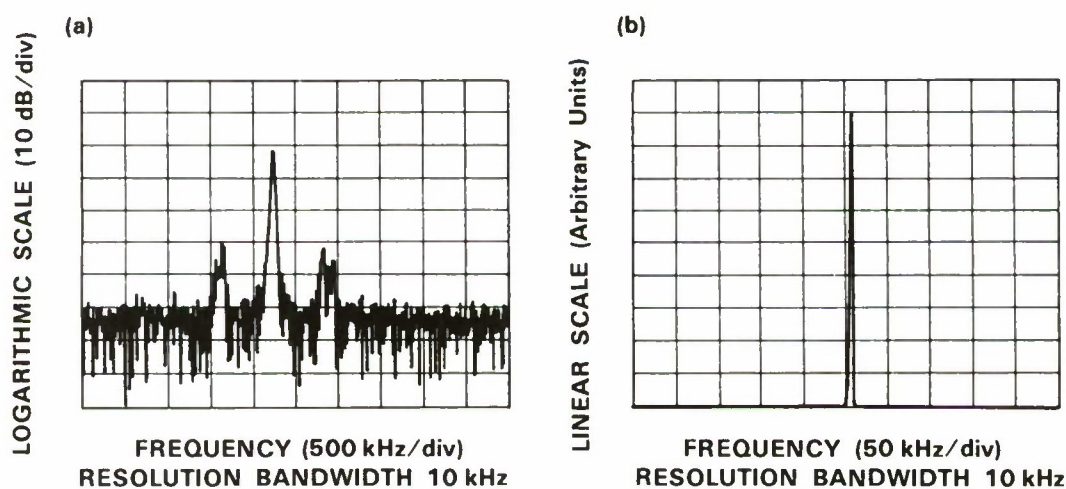
Figure 2-9. Instrument-limited heterodyne spectrum of two CW Nd:YAG microchip lasers: (a) on a logarithmic scale, and (b) on a linear scale.

28

equal contributions to the linewidth from each laser. The theoretical phase-fluctuation linewidth is estimated to be only a few hertz. Relaxation oscillations account for the observed sidebands 700 kHz away from the main peak. The intensity of the sidebands varied with time, but was always >30 dB below the main peak.

The microchip Nd:YAG lasers have been pumped with the unfocused output of a 20-mW GaAlAs diode laser. The Nd:YAG cavity was placed about 30 μm from the output facet of the diode laser and longitudinally pumped. The resulting pump spot size in the Nd:YAG was about 50 μm in diameter. The output of the microchip lasers showed single-longitudinal-mode, single-transverse-mode operation at all available powers. The divergence of the lasers was diffraction limited at about 20 mrad.

The low pump threshold, high efficiency, and single-frequency operation of the Nd:YAG microchip lasers makes diode-pumped microchip lasers extremely promising. Such lasers could be stress-tuned, using proven techniques,[14] over a wide range of frequencies. The microchip concept is also applicable, for example, to frequency converters, modulators and Q-switches, with photo-lithographically deposited electrodes. It results in low-cost, volume-producible lasers and electro-optic devices.

J.J. Zayhowski   A. Mooradian
R.H. Hancock   C. Dill

2.5 SUM-FREQUENCY MIXING OF FREQUENCY-MODULATED LASER RADIATION

Efficient optical excitation of a Doppler-broadened atomic vapor requires the illumination of each velocity subgroup within the vapor by resonant radiation. The number of different optical frequencies required for complete excitation is given by the Doppler-broadened linewidth divided by the atomic homogeneous linewidth. In sodium vapor the homogeneous linewidth is 10 MHz, while the Doppler-broadened linewidth is about 3 GHz, and thus 300 separate frequencies are required to achieve complete excitation. The attainment of such a frequency distribution from a *single* laser source is possible either by constructing a very long laser cavity[15] and ensuring that each laser mode within the Doppler-broadened linewidth is oscillating, or by extracavity modulation of the laser radiation with very high depth of modulation. We believe that a simpler method for achieving the required spectral content for efficient excitation of a Doppler-broadened atomic vapor is to generate the resonant radiation by sum-frequency mixing the outputs of *two* frequency-modulated lasers.

The sum-frequency-mixing process can result in a high frequency density for the sum radiation. The spectral range of the sum radiation is equal to the sum of the spectral ranges of the fundamental radiations. If the frequency intervals in the fundamental radiations are not the same, the number of frequencies in the sum radiation is given by the product of the number of frequencies in the two fundamental radiations. Figure 2-10 illustrates the spectral profiles of the radiation from two free-running CW Nd:YAG lasers (1.064 μm and 1.319 μm) and their sum radiation (0.589 μm). The sum radiation contains nine frequencies over a 550-MHz spectral
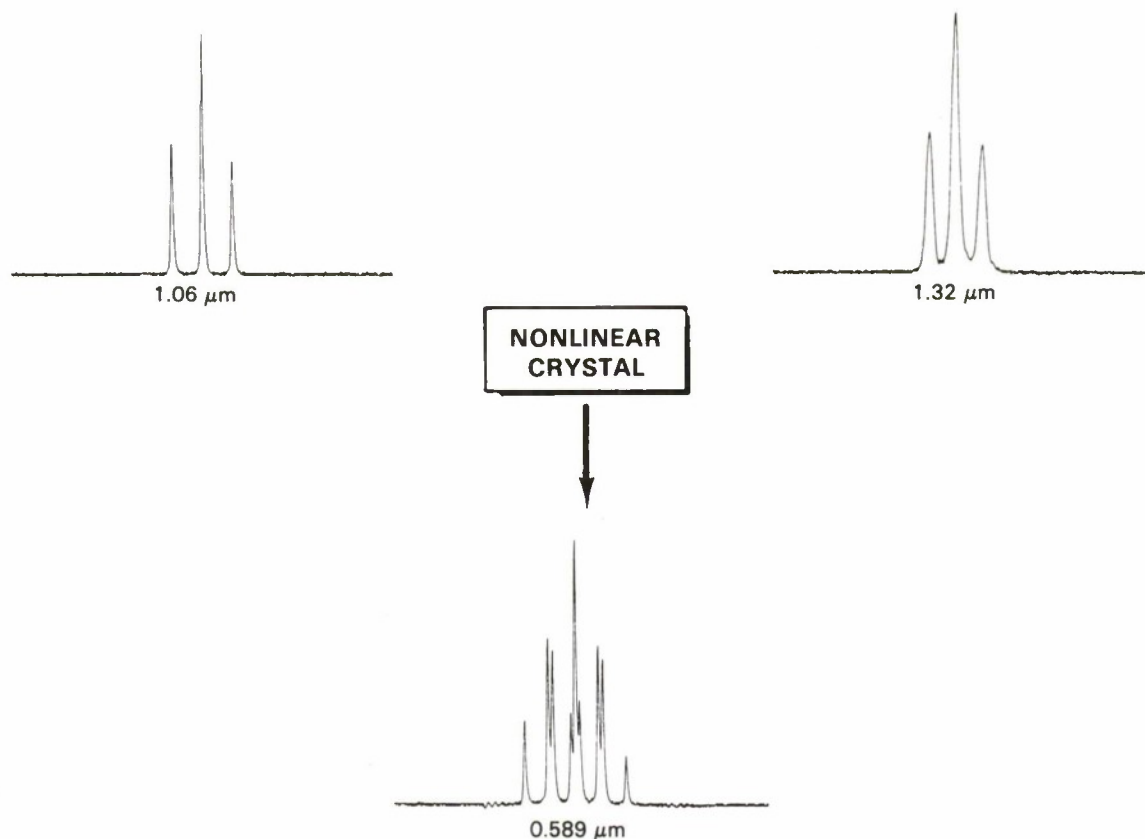
Figure 2-10. Spectral profiles of two free-running CW Nd:YAG lasers and their sum radiation. Both Nd:YAG lasers operated on three adjacent longitudinal cavity modes. The longitudinal cavity modes were separated by 125 MHz in the 1.064-μm laser and 150 MHz in the 1.319-μm laser. The spectral profiles were measured with three separate scanning confocal Fabry-Perot analyzers, each with a finesse of about 200. The 1.06-μm and 0.589-μm analyzers had free-spectral ranges of 2 GHz, while the 1.319-μm analyzer had a free-spectral range of 8 GHz. The resolution in each spectral profile is instrument limited.

range. The 61-MHz average frequency interval is less than one half the frequency interval of either Nd:YAG laser. By intracavity frequency modulation of both Nd:YAG lasers[16] it is possible to increase both the spectral range and the number of frequencies of the sum radiation, as shown in Figure 2-11 for increasing depths of modulation. In the lower spectral profile the sum radiation includes 59 frequencies over a 1.7-GHz range. The central 1 GHz of this spectral profile contains 39 frequencies spaced at intervals of 25 MHz. In this case 25 MHz is the minimum interval possible in the sum radiation since the difference between the modulation frequencies of the two Nd:YAG lasers is 25 MHz. By decreasing the difference in modulation frequencies to 10 MHz, the sum radiation could efficiently excite all of the sodium atoms in a Doppler-broadened vapor.

Single-frequency laser radiation is usually produced with a traveling-wave ring laser cavity. This avoids the spatial hole burning present within the gain media of standing-wave laser cavities

30
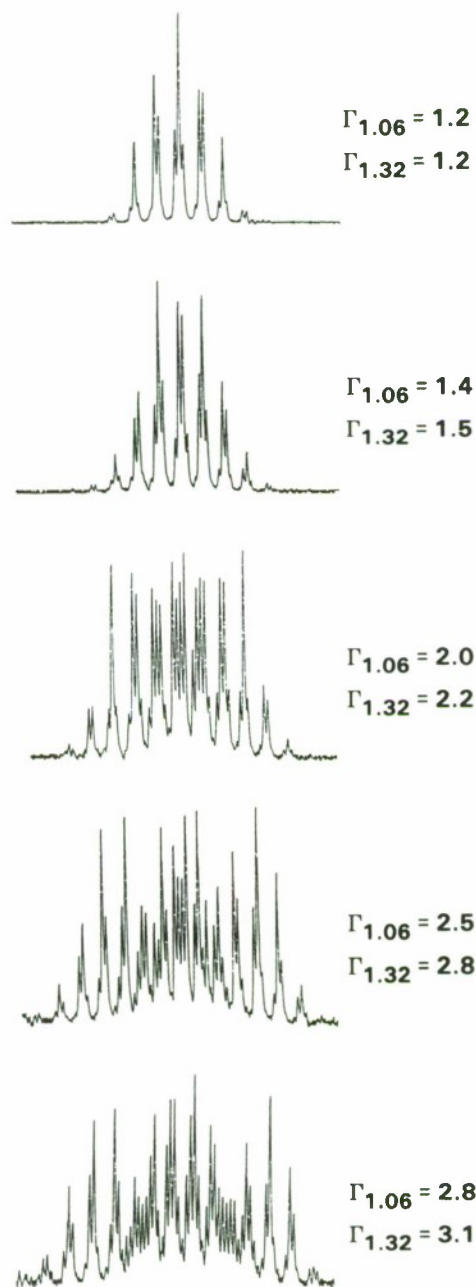
Figure 2-11. Spectral profiles of the sum radiation (0.589 µm) for increasing depths of modulation Γ of the fundamental radiation from two Nd:YAG lasers (1.064 µm and 1.319 µm). The 1.064-µm Nd:YAG laser was frequency modulated at 124.8 MHz while the 1.319-µm Nd:YAG laser was frequency modulated at 149.7 MHz. The separation between the nearest frequencies in the sum radiation is 25 MHz. The modulation frequencies were chosen so that the smallest frequency interval in the sum radiation could be resolved with the Fabry-Perot spectrum analyzer.

106458-32

31

$\Gamma = 1.2$

$\theta = 180°$
$\Gamma_{eff} = 0$

$\theta = 120°$
$\Gamma_{eff} = 1.4$

$\theta = 60°$
$\Gamma_{eff} = 2.2$

$\theta = 0°$
$\Gamma_{eff} = 2.4$

106458-16
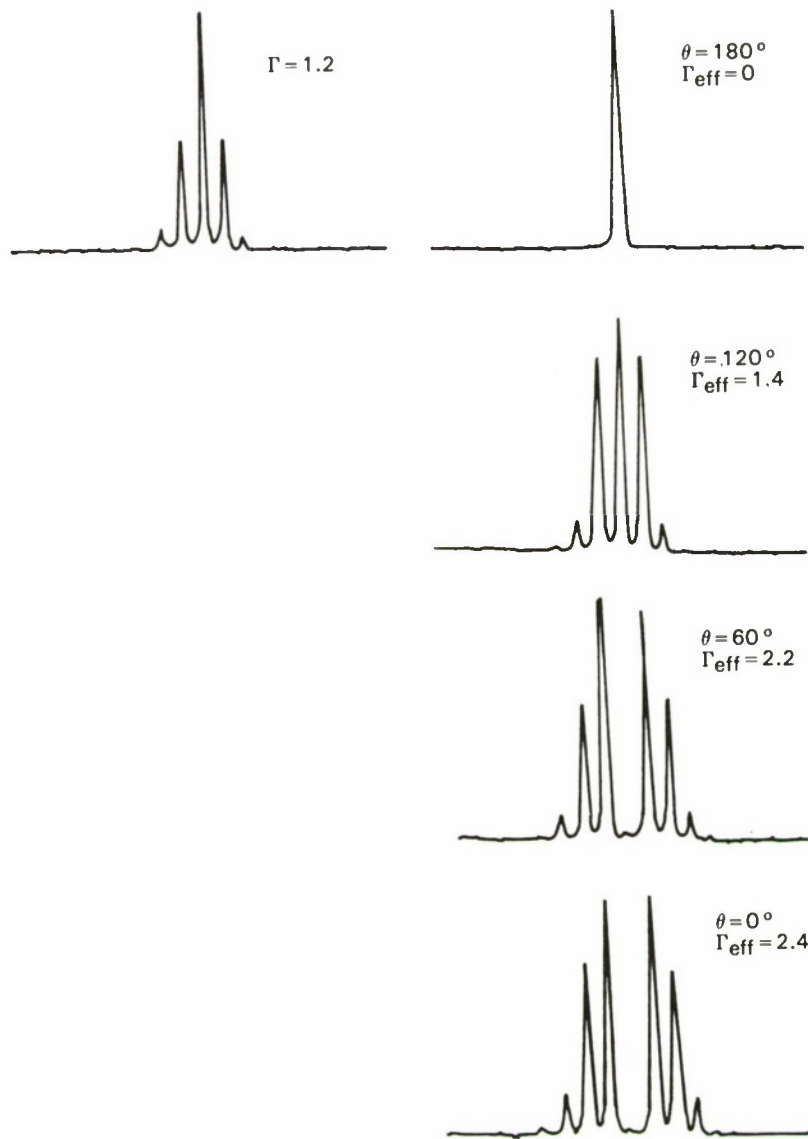
Figure 2-12. Spectral profiles of a 1.319-μm frequency-modulated Nd:YAG laser both before (left) and after (right) an external frequency modulator, for various phase angles θ between the intracavity and external cavity modulation voltages. The single-carrier 1.319-μm laser radiation had a modulation depth of Γ = 1.2 rad. By operating the external cavity modulator 180° out-of-phase with the intracavity modulator, and with the same depth of modulation, the 1.319-μm radiation could be completely demodulated to a single frequency. Γ_{eff} is the effective depth of modulation after the external cavity modulator.

32

which causes these lasers to prefer multimode operation. Unfortunately, the larger number of optical elements within the ring laser cavity usually results in less output power than equivalent standing-wave lasers. By intracavity frequency modulation of a standing-wave laser cavity, followed by extracavity demodulation, it is also possible to generate single-frequency laser radiation. Intracavity frequency modulation can result in single-carrier frequency-modulated laser radiation with a power equal to the unmodulated laser power.[16] This radiation may then be demodulated either directly with an external electrooptic phase modulator[17] or by nonlinear frequency conversion.[18] We have generated single-frequency radiation utilizing both of these techniques.

Figure 2-12 shows the spectral profiles obtained from a 400-mW, frequency-modulated, 1.319-μm Nd:YAG laser beam, of which 340 mW was passed through an external frequency demodulator. The spectral output of the Nd:YAG laser is shown in the upper left, while the spectral output of the external modulator is shown on the right as a function of the phase angle θ between the intracavity and extracavity modulation voltages. When the intracavity and extracavity modulators are driven 180° out-of-phase and with the same depths of modulation, single-frequency radiation is produced. The principal difficulty is obtaining sufficient extracavity modulation depth to offset the intracavity modulation depth required to achieve single-carrier operation of the laser. In this case, the intracavity phase modulator consisted of a $4 \times 4 \times 40$-mm LiNbO$_3$ crystal. The extracavity phase modulator consisted of two back-to-back $1 \times 1 \times 20$-mm LiTaO$_3$ crystals which were placed in a high-Q resonant circuit. Figure 2-13 shows the spectral profile of the frequency-modulated 1.319-μm Nd:YAG laser when operated on dual adjacent carrier frequencies both before and after being demodulated.

MODULATED $\Gamma = 1.2$

DEMODULATED $\Gamma = 0$

106458-17

Figure 2-13.   Spectral profiles of dual-carrier 1.319-μm laser radiation both before and after demodulation with an external cavity modulator. The external modulator was operated 180° out-of-phase and with the same depth of modulation as the intracavity modulator.

We have also generated single-frequency radiation by sum-frequency mixing the outputs of two Nd:YAG lasers which were frequency modulated 180° out-of-phase with the same depths of modulation.[16] Figure 2-14 shows the spectral profiles of the radiation from frequency-modulated 1.064-μm and 1.319-μm Nd:YAG lasers, and the sum-frequency mixed radiation for various phase angles θ between the two laser modulations. When one of the two Nd:YAG lasers operated with dual carrier frequencies, the demodulated ($\theta = 180°$) sum radiation consisted of two frequencies. This is shown in Figure 2-15.

33

Γ = 2.8

θ = 180°
$\Gamma_{eff} = 0$

1.319 μm

θ = 120°
$\Gamma_{eff} = 2.8$

Γ = 2.8

θ = 60°
$\Gamma_{eff} = 4.9$

1.064 μm

θ = 0°
$\Gamma_{eff} = 5.6$

0.589 μm
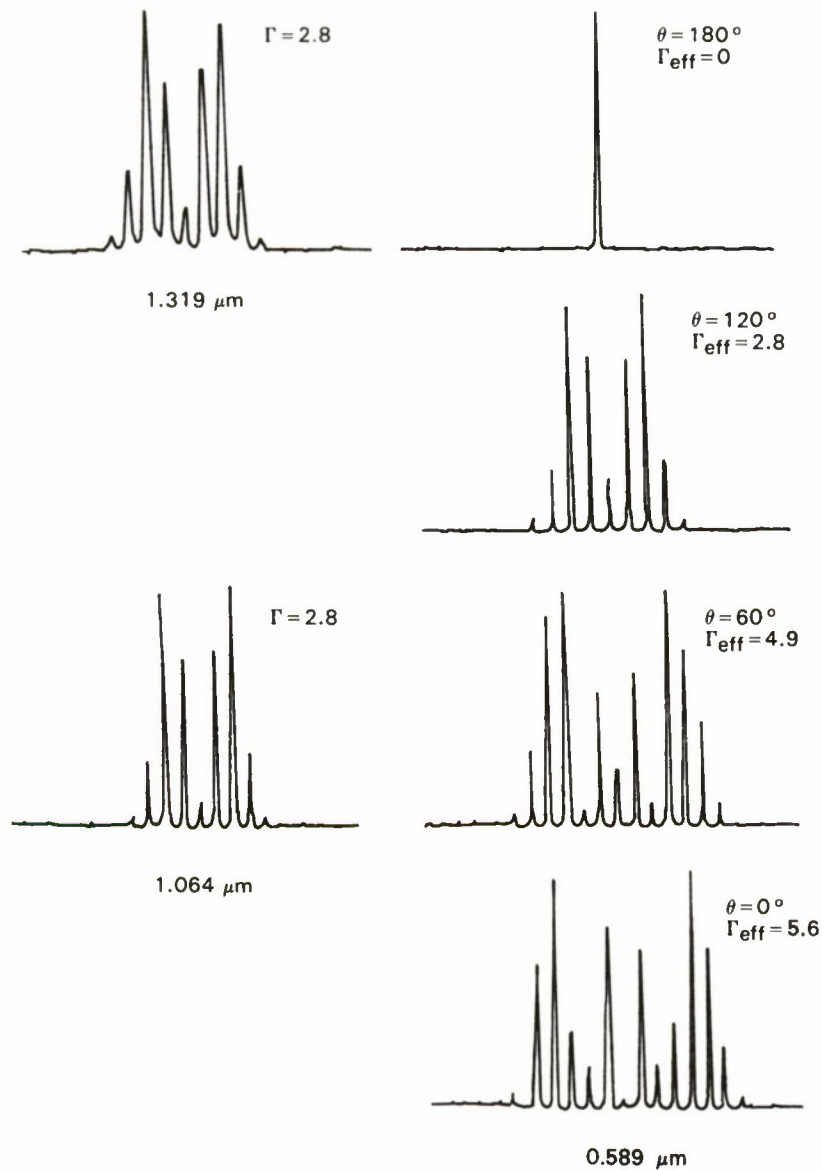
Figure 2-14. *Spectral profiles of frequency-modulated 1.064-μm and 1.319-μm Nd:YAG laser radiation (left) and their sum radiation (right), for various phase angles θ between the two laser modulations. Each Nd:YAG laser was modulated with the same depth of modulation, Γ = 2.8 rad. When these lasers were modulated 180° out-of-phase, single-frequency sum radiation at 0.589 μm was produced. Γ_{eff} is the effective depth of modulation of the sum radiation.*

106458-18

MODULATED

1.319 μm

DEMODULATED

0.589 μm

1.064 μm
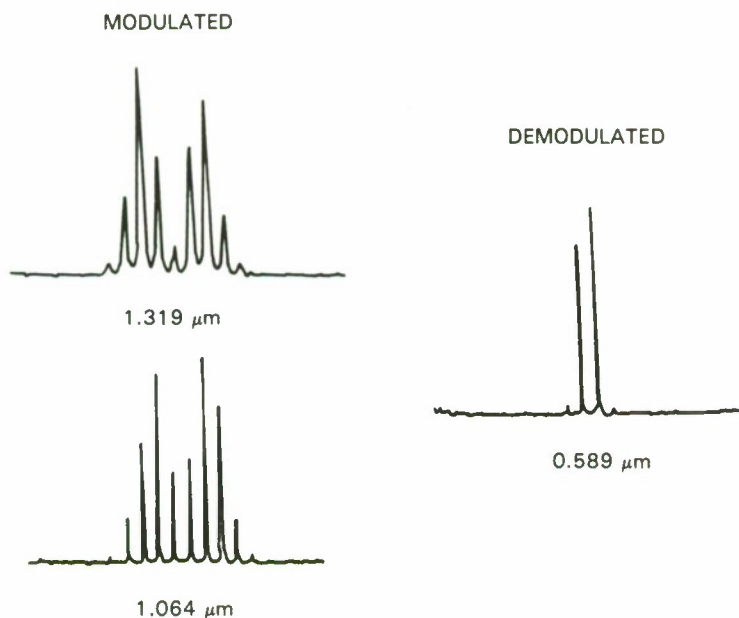
Figure 2-15.   Spectral profiles of single-carrier 1.319-μm and dual-carrier 1.064-μm Nd:YAG laser radiation, and the demodulated sum radiation.

The effective depth of modulation of the sum radiation is related to θ and the depth of modulation Γ of each Nd:YAG laser by

$$\Gamma_{eff} = 2\Gamma \cos (\theta/2). \qquad (2\text{-}2)$$

The effective depth of modulation of the 1.319-μm laser radiation after passing through the external cavity modulator is also given by this equation, where θ is now the relative phase angle between the internal and external cavity modulators. The data of Figures 2-12 and 2-14 are in good agreement with this equation.

T.H. Jeys

REFERENCES

1. H.W. Kogelnik, E.P. Ippen, A. Dienes, and C.V. Shank, IEEE J. Quantum Electron. **QE-8**, 373 (1972).

2. J.A. Arnaud, Appl. Opt. **8**, 189 (1969).

3. A. Sanchez, R.E. Fahey, A.J. Strauss, and R.L. Aggarwal, Opt. Lett. **11**, 363 (1986).

106458-19

4. Solid State Research Report, Lincoln Laboratory, MIT (1987:4), p.13, DTIC AD-A194708.

5. P.F. Moulton, J. Opt. Soc. Am. B **3**, 125 (1986).

6. W.H. Knox, IEEE J. Quantum Electron. **QE-24**, 388 (1988).

7 P.A. Schulz, to be published.

8. S. Basu and R. Byer, in *Technical Digest of the Conference on Lasers and Electrooptics* (OSA, Washington, D.C., 1988), paper THV1.

9. K.F. Wall, R.L. Aggarwal, R.E. Fahey, and A.J. Strauss, IEEE J. Quantum Electron. **QE-24**, 1016 (1988).

10. L.D. Schearer, M. Leduc, D. Vivien, A.M. Lejus, and J. Thery, IEEE J. Quantum Electron. **QE-22**, 713 (1986).

11. K.S. Bagdasarov, L.M. Dorozhkin, L.A. Ermakova, A.M. Kevorkov, Y.I. Krasilov, N.T. Kuznetsov, I.I. Kuratev, A.V. Ptemkin, L.N. Raiskaya, P.A. Tseitlin, and A.V. Shestakov, Sov. J. Quantum Electron. **13**, 1082 (1983).

12. Solid State Research Report, Lincoln Laboratory, MIT (1988:1), p. 26, DTIC AD-A201044.

13. P. Esherick and A. Owyoung, in *Technical Digest, Conference on Lasers and Electrooptics* (OSA, Washington, D.C., 1988), Paper THB2.

14. A. Owyoung and P. Esherick, Opt. Lett. **12**, 999 (1987).

15. J. Liang and C. Fabre, Optics Comm. **59**, 31 (1986); J. Liang, L. Moi, and C. Fabre, Optics Comm. **52**, 131 (1984); L. Moi, Optics Comm. **50**, 349 (1984).

16. Solid State Research Report, Lincoln Laboratory, MIT (1988:2), p. 19.

17. G.A. Massey, M.K. Oshman, and R. Targ, Appl. Phys. Lett. **6**, 10 (1965).

18. H.P. Weber and E. Mathieu, IEEE J. Quantum Electron. **QE-3**, 376 (1967); S.R. Bramwell, A.I. Ferguson, and D.M. Kane, Opt. Comm. **61**, 87 (1987).

3. MATERIALS RESEARCH

3.1 VERTICAL ROTATING-DISK OMVPE REACTOR

A vertical rotating-disk reactor has been developed for growth of extremely uniform GaAs and AlGaAs layers by organometallic vapor phase epitaxy (OMVPE). By operation at reduced pressure (0.2 atm) and a substrate rotation rate of 500 rpm, thickness uniformity of ± 1 percent and alloy compositional uniformity of ± 0.1 percent (e.g., ± 0.0003 in $Al_{0.3}Ga_{0.7}$) have been achieved for layers grown on 5-cm-diam. substrates.

Figure 3-1 is a schematic diagram of the reactor, which incorporates a vertical quartz tube of 10-cm internal diameter and an RF-heated rotating molybdenum susceptor of 6.7-cm diam. The process gases enter the top of the tube through a stainless steel mesh to ensure uniform (plug) flow and exit symmetrically at the bottom to maintain the cylindrical symmetry of the system. Substrates are loaded from the top of the tube through a glove box to minimize introduction of air into the reactor. The upper portion of the tube remains free of deposits during
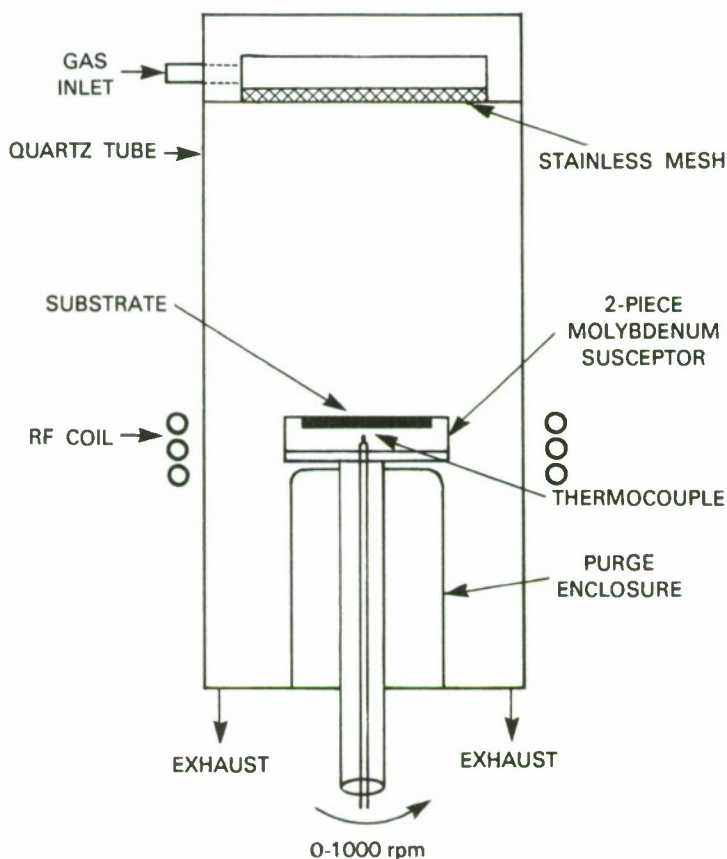
Figure 3-1. *Schematic of vertical rotating-disk OMVPE reactor.*

growth, thus eliminating the possibility of particulates falling onto the substrate and also minimizing the downtime required for reactor cleaning. Controlled susceptor rotation rates up to 1,000 rpm can be obtained by using a variable speed motor coupled to a magnetic-fluid feedthrough. The center of the susceptor cap is recessed to prevent the substrate wafer from flying off the susceptor at high rotation rates. Temperature uniformity across a 5-cm-diam. GaAs substrate at the growth temperature is $\pm 2°C$ as measured with an optical pyrometer.

The source gases used for growth of GaAs and AlGaAs epilayers were trimethylgallium (TMG), trimethylaluminum (TMA), and 100 percent arsine. Hydrogen was used as the carrier gas. The TMG and TMA concentrations were 0.8-4 $\times$ 10^{-4} and 0.05-0.4 $\times$ 10^{-4} mole fraction, respectively, and the V/III ratio ranged from 40 to 130. Hydrogen selenide (500 ppm in hydrogen) was used as an n-type dopant. The reactor pressure was maintained at 0.2 atm to suppress natural convective flows. The GaAs layers were grown at 700°C and the AlGaAs layers at 800°C. Susceptor rotation rates were varied between 20 and 500 rpm.

Specular surfaces were obtained for GaAs and AlGaAs layers grown with V/III ratios of greater than 80. Nominally undoped GaAs layers were n type, with a typical carrier concentration of 1×10^{14} cm^{-3} and mobility exceeding 1×10^5 cm^{2}V^{-1}s^{-1} at 77 K. Susceptor rotation had no effect on these values.

Thickness profiles are shown in Figure 3-2 for 10-μm-thick GaAs epilayers grown on 5-cm-diam. substrates at rotation rates of 20, 200, and 500 rpm. The plotted thickness values are normalized to the thickness at the center of the substrate. The measured thickness is greater near the substrate periphery than at the center by 15 percent for a susceptor rotation rate of 20 rpm, 5 percent for 200 rpm, and 1 percent for 500 rpm. For mass-transport-limited growth, as in the present study, epilayer thickness is inversely proportional to the boundary layer thickness. Therefore the experimental results imply that the velocity of the impinging gas is not uniform across the substrate in the absence of rotation, but that rotation is effective in establishing a self-similar velocity profile and uniform boundary layer. In other experiments, thickness uniformity was found to be independent of substrate temperature, growth rate, and V/III ratio.

Figure 3-3 shows carrier concentration depth profiles measured with an electrochemical profiler at six locations on a Se-doped GaAs epilayer grown on a 5-cm-diam. substrate at a rotation rate of 500 rpm. The profiles are flat, and lateral uniformity in concentration at a given depth is ± 2.5 percent or better. The agreement from profile to profile in the depth of the epilayer-substrate interface confirms that the epilayer thickness is uniform to ± 1 percent across the substrate. For a given concentration of hydrogen selenide, the same carrier concentration in the epilayers was obtained for growth at rotation rates of 20, 200, and 500 rpm.

The lateral compositional uniformity of $Al_xGa_{1-x}As$ epilayers was determined by comparing the positions of the bound-exciton peak in photoluminescence (PL) spectra measured at 5 K. Figure 3-4 shows the peaks measured at six locations across the diameter of an $Al_{0.29}Ga_{0.71}As$ epilayer grown on a 5-cm-diam. substrate at a rotation rate of 500 rpm. The variation of the peak
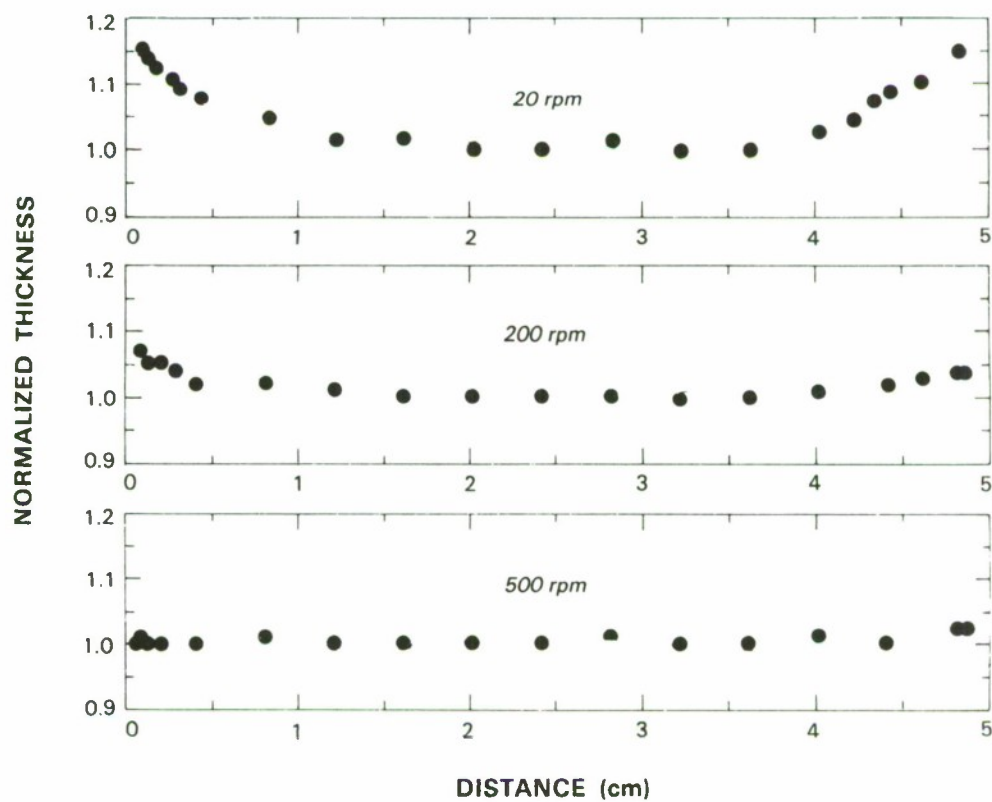
Figure 3-2. Normalized epilayer thickness profiles across 5-cm-diam. substrate for rotation rates of 20, 200, and 500 rpm.
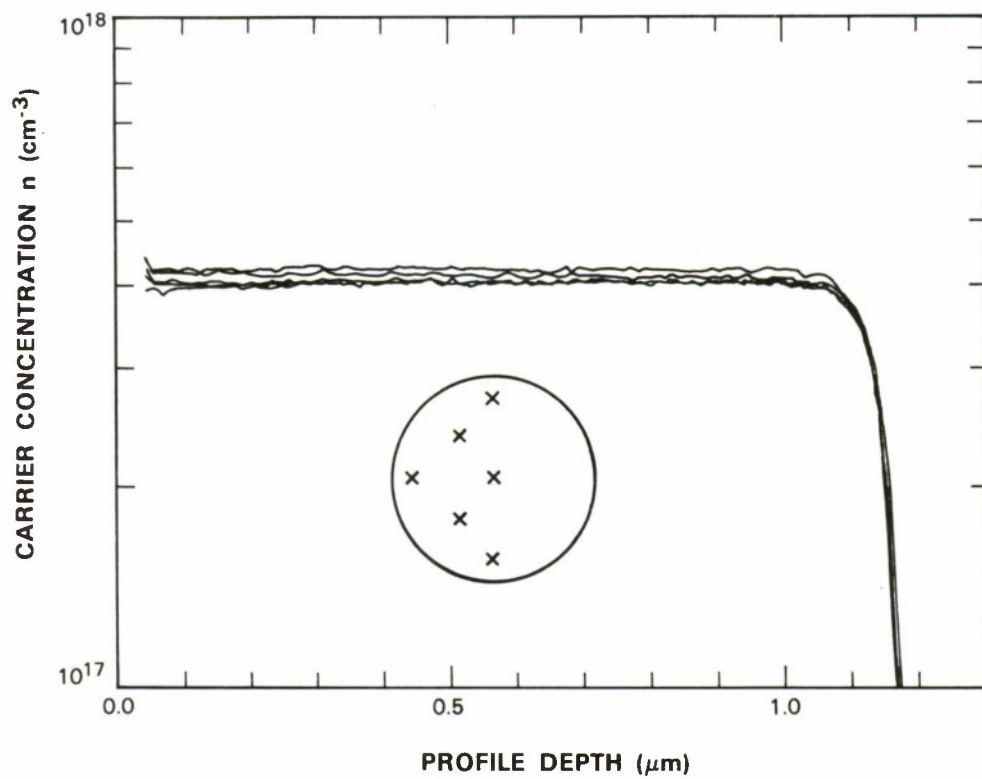
Figure 3-3.   Carrier concentration depth profiles measured at positions indicated on 5-cm-diam. Se-doped GaAs epilayer.
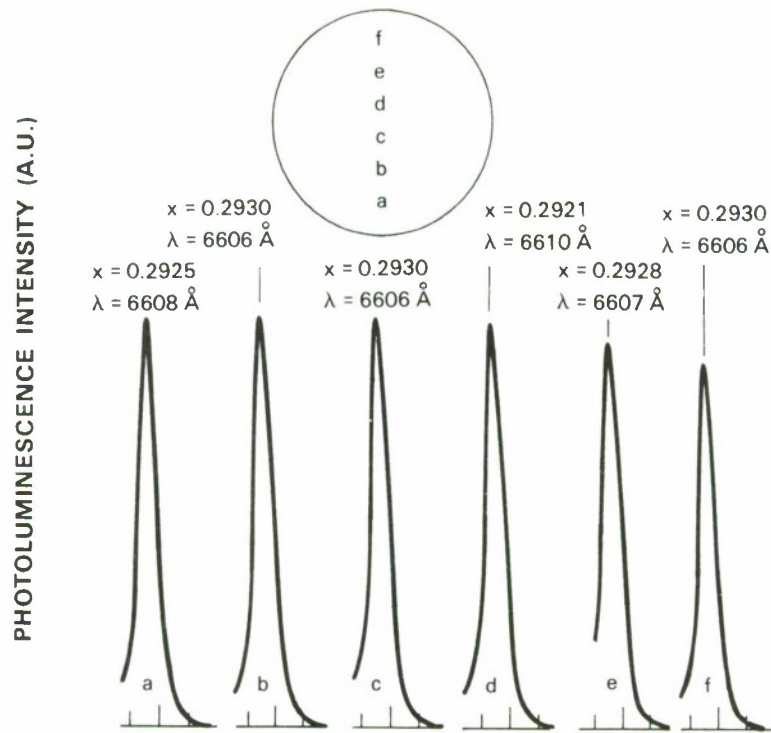
Figure 3-4. Bound-exciton photoluminescence peaks measured at 5 K for positions indicated on a 5-cm-diam. $Al_xGa_{1-x}As$ epilayer with $\bar{x} = 0.2927$.

·wavelength is less than ±2Å, which corresponds to a standard deviation σ of 0.0003 in x. Compositional uniformity of four $Al_xGa_{1-x}As$ epilayers with $0.1 < x < 0.4$ is summarized in Table 3-1. In all cases, $\sigma/\bar{x}$ is better than ±0.2 percent. The compositional uniformity showed no dependence on rotation rate. The insensitivity of both doping and compositional uniformity to the rotation rate indicates that the relative rates of gas phase transport for the different reactant species are independent of rotation rate, although the absolute rates vary.

Multiple GaAs/AlGaAs quantum well structures grown in the reactor were characterized by PL measurements at 6 K. Figure 3-5 is the spectrum of a four-well structure with GaAs wells and $Al_{0.5}Ga_{0.5}As$ barriers that was grown at the rate of 5 Å/s without growth interruptions. The well widths ranged from 22 to 103 Å, as estimated from the peak energy of the emission corresponding to the electron-heavy hole transition. The full width at half maximum of the peak for the 22-Å well, 12 meV, is comparable to values reported in the literature[1] for high-quality structures. An additional measure of the epilayer thickness uniformity is given by the variation in the peak positions measured at different locations across the substrate. For the 48-Å well, for example, this variation corresponds to a thickness variation of only 1 Å.

C.A. Wang
D.M. Tracy
J.W. Caunt

TABLE 3-1		
Compositional Uniformity of $Al_xGa_{1-x}As$ Epilayers		
PL Peak (Å)	$\bar{x}$	σ
7454-7457	0.1212	0.0002
6903-6907	0.2280	0.0003
6606-6610	0.2927	0.0003
6215-6221	0.3870	0.0006
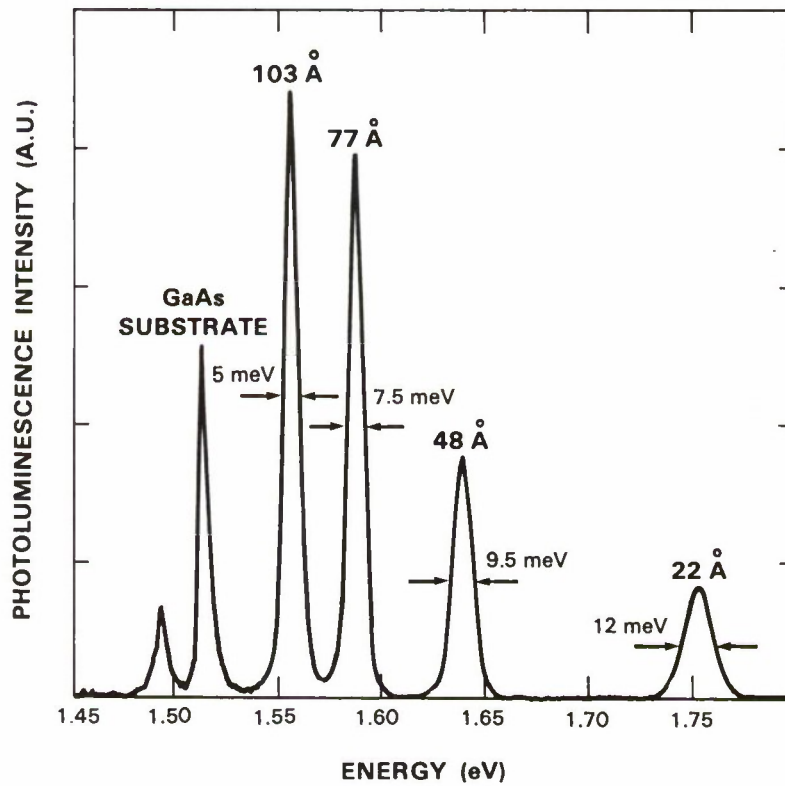
Figure 3-5. *Photoluminescence spectrum at 6 K for structure containing four GaAs quantum wells with* $Al_{0.5}Ga_{0.5}As$ *barriers.*

42

REFERENCES

1.   M. Tanaka and H. Sakaki, J. Cryst. Growth **81**, 153 (1987).

4. SUBMICROMETER TECHNOLOGY

4.1. NEW ELECTRON BEAM LITHOGRAPHY SYSTEM

We have recently acquired a new scanning electron-beam lithography system, which is a vector-scan, Gaussian-spot, e-beam system optimized for high-resolution patterning. It is designed for maskmaking as well as direct-write on substrate applications, and can accommodate samples up to 5 inches in size. It features an 8-nm writing spot, laser-interferometer-controlled substrate stage, automatic pattern registration, correction for writing field distortion, and computer automation for unattended operation during long patterning runs. In comparison with other commercial e-beam lithography systems, it offers superior patterning resolution, but, as it is designed for a research environment, it lacks the throughput enhancements and software sophistication commonly found on production systems. We expect that the new system will complement the existing primary pattern generation resources, and will find application to research programs which stress high-resolution patterning, flexibility, designer interaction, or quick turn-around. Its capabilities are especially suited to the patterning of high-resolution contact photomasks, x-ray masks, masked ion beam lithography tooling, and direct-write device applications.

The designer has a choice of four pattern description languages: MANN-3600, JEOL01, CIF and GDSII-stream. The MANN-3600 language, which describes all patterns in terms of rectangles, is compatible with our optical pattern generator and is supported by several geometric-design software packages. The JEOL01 provides a richer set of geometric primitives including polygons, single-pass lines, and circles. There are no graphical editors for JEOL01, but the textual format of JEOL01 is simple enough to permit the designer to enter patterns by hand. The CIF pattern format is more sophisticated than JEOL01 and is supported by geometric design software. In addition to a rich set of geometric primitives, CIF supports a hierarchical pattern description and complex pattern transformations. The GDSII stream format is used for data interchange by several commercial geometric design packages. The system manufacturer provided software to accept the MANN-3600 and JEOL01 pattern formats directly. We have written software to translate CIF into JEOL01 format, and software is available to convert GDSII-stream format to CIF. The CIF translator accommodates the idiosyncrasies of our geometric-design software, and allows the designer to exercise low-level controls (such as specifying single-pass features and dose modulation) from a high-level design environment. We have also developed pattern preview and verification software for the MANN-3600, JEOL01 and CIF pattern formats.

The new system has just recently passed its customer acceptance testing. During the shakedown period numerous software enhancements were made. The acceptance tests demonstrated many of the capabilities of the system. Figure 4-1 illustrates scanning electron micrographs of representative test structures written in 200 nm of PMMA resist on a silicon substrate. These geometries were written with a 25-kV accelerating voltage, a nominal spot size of 0.025 μm, and were patterned with multiple beam scans. Although not illustrated in the figure, the test also included 0.050-μm isolated lines written as single beam pass features. Figure 4-2 illustrates a series of 70-nm gold lines patterned on a silicon substrate using a PMMA exposure followed by a lift-off technique.
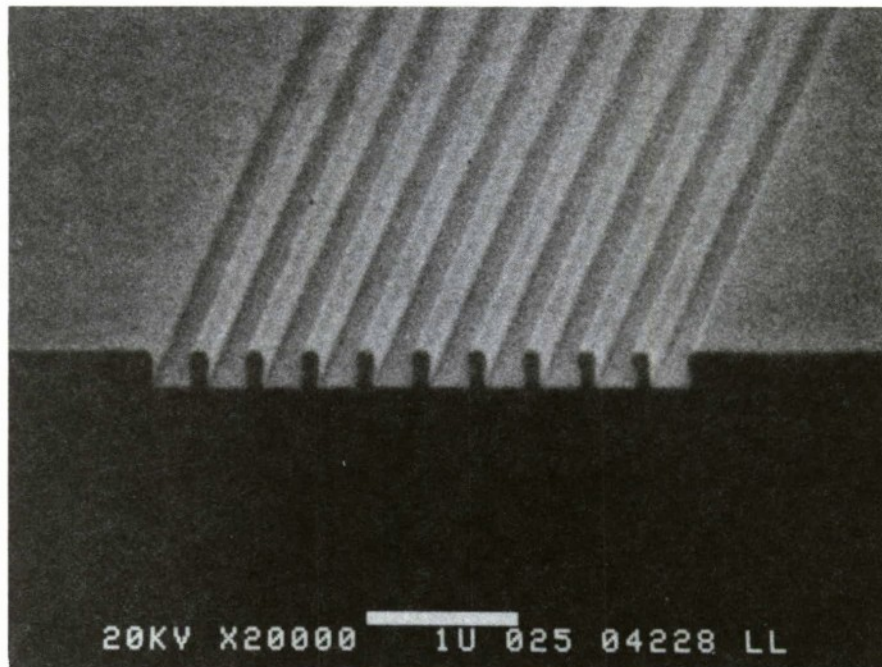
(a)
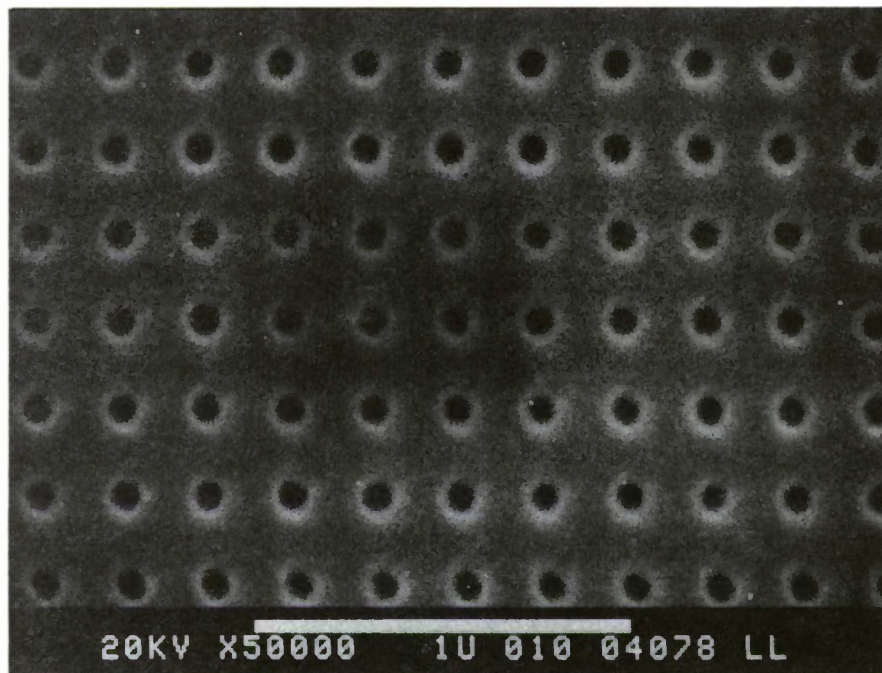
(b)

Figure 4-1. Scanning electron beam lithography test patterns written in 200 nm of PMMA resist: (a) 320-nm-period grating, and (b) 80-nm-diam. dots.

46
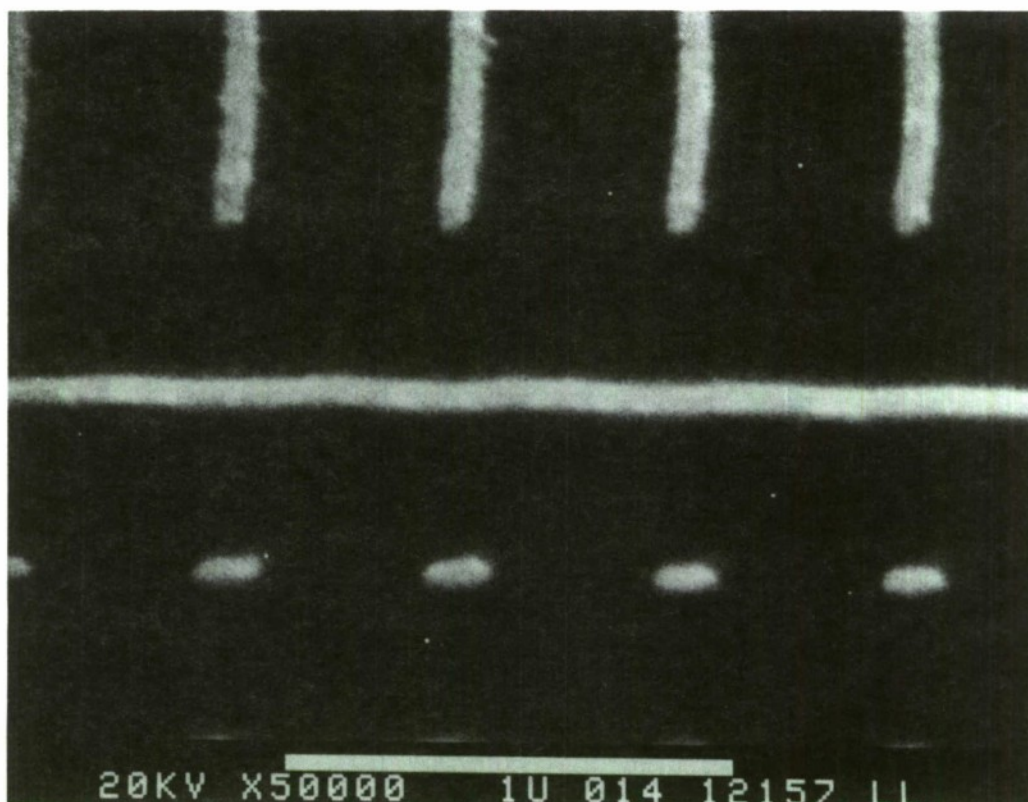
Figure 4-2.   70-nm gold lines on a silicon substrate patterned using direct-write lithography.

To date, the new system has enjoyed a limited but expanding role in our research programs. It has been used to pattern structures for the study of dry-etching-induced damage in GaAs devices.[1] For this research, it was used to prepare masked-ion-beam lithography tooling or to directly expose features on the GaAs substrates. Line widths were varied between 0.08 and 1.5 μm. The patterning resolution, feature edge smoothness and acuity, and the ability to adjust feature sizes through exposure dose modulation were critical to this application.

The system has also been used to produce contact photomasks for the development of a diamond permeable-base transistor. Figure 4-3 illustrates an optical micrograph of the base-grating photomask for the transistor. The dark squares, visible in the photo, are actually gratings of 1-, 2-, and 4-μm periods.

Optical waveguide structures require extremely smooth pattern edges and accurate feature placement to avoid pattern butting errors and discontinuities at corners and joints. Figure 4-4

47

250 μm

10

79
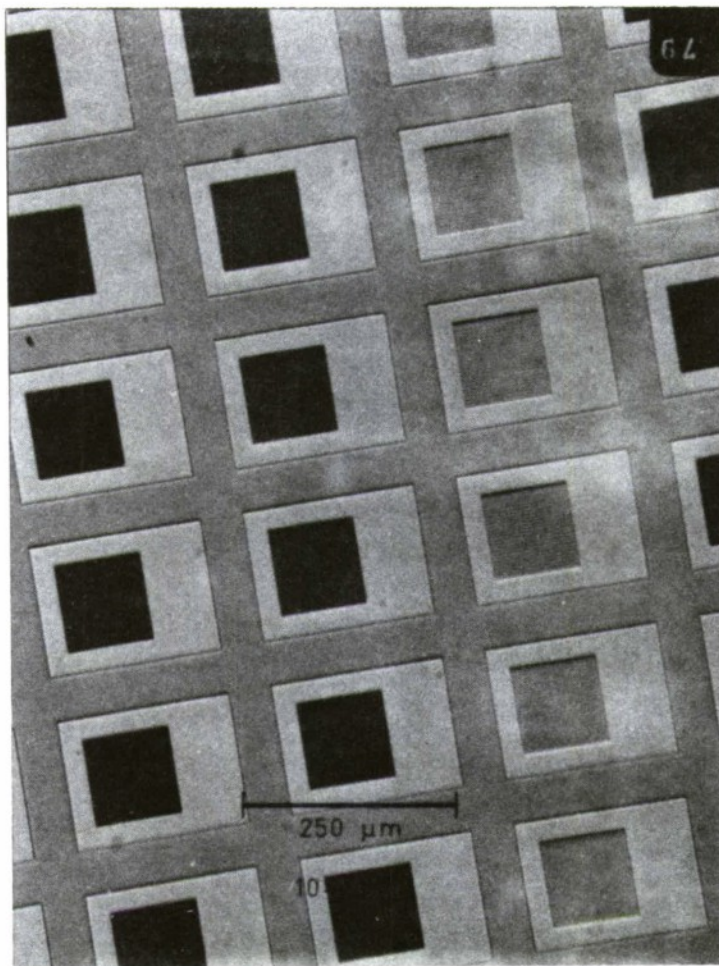
106458-22

Figure 4-3.   Diamond permeable-base transistor base grating photomask with linewidths of 0.5 μm, 1 μm and 2 μm.

illustrates a micrograph of a photomask used to pattern a multimode power splitter. The photo illustrates a small section of a 32-channel power splitter patterned using the electron beam system.

<div align="right">

T. M. Lyszczarz
M. J. Rooks

</div>
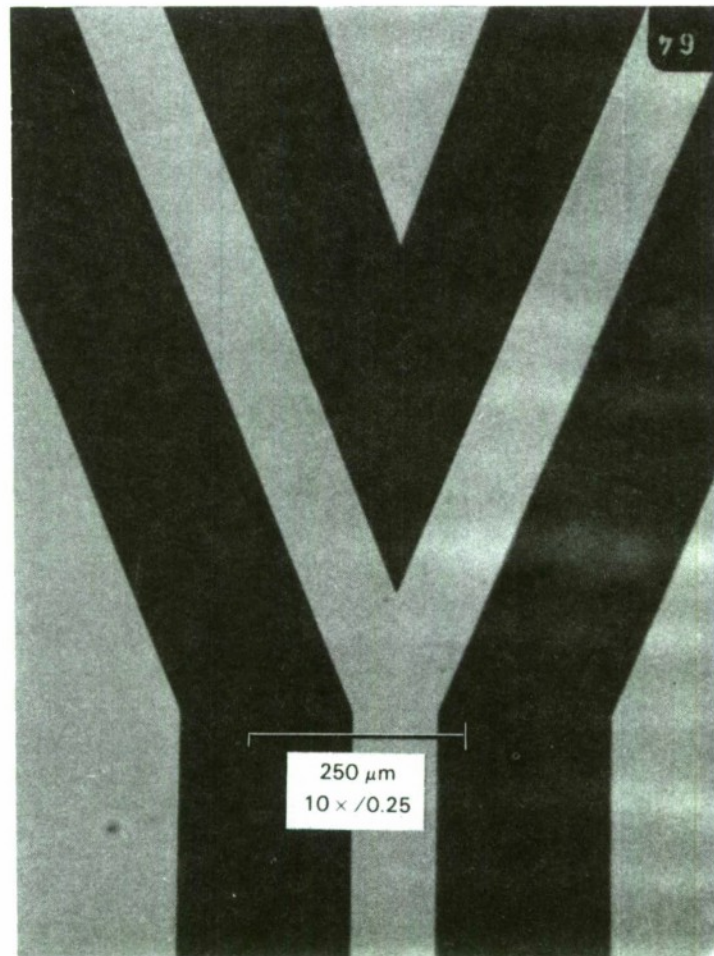
Figure 4-4. Multimode optical waveguide splitter photomask. The pattern is in chrome on a quartz plate.

4.2   DRY-ETCHING-INDUCED DAMAGE ON VERTICAL SIDEWALLS OF GaAs CHANNELS

Damage induced by dry etching greatly affects electronic transport in structures with submicrometer dimensions. Previous studies[2,3] have shown that surface damage induced during etching of a conducting channel (e.g., in the gate recess etch for a metal-semiconductor field-effect transistor) can significantly alter transport phenomena. Vertical sidewalls of etched structures are exposed to lower ion fluxes than surfaces lying in the wafer plane, and receive oblique ion bombardment. In the present work, dry-etching-induced damage on the vertical sidewalls of narrow GaAs structures is characterized. To assess the effect of damage induced by the etch processes, conduction through narrow channels, leakage current on Schottky diodes, and Auger electron spectra were analyzed.

The effect of sidewall damage on electronic transport was studied using narrow conducting channels between ohmic pads. The channels were defined by either masked-ion-beam lithography or electron-beam lithography with channel widths varying from 0.08 to 1.5 μm. With SiO_2 as the etch mask, conducting channels were formed by using reactive-ion etching (RIE) or ion-beam-assisted etching (IBAE) to remove the epitaxial material outside the channels down to the semi-insulating substrates. Figures 4-5(a) and 4-5(b) show the sidewalls of 0.15-μm-wide channels etched by RIE and IBAE, respectively. In RIE, Cl_2 was used as the etch gas at 5-mTorr pressure and 250-V dc self-bias. This etching condition provides an anisotropic etch profile, extremely smooth sidewalls and bottom surface, and a GaAs etch rate of 0.45 μm/min. In IBAE, a 500-V Ar ion beam and 2.8-mTorr Cl_2 pressure were used. Very smooth sidewalls and a GaAs etch rate of 0.05 μm/min were obtained. Even though faster etch rates can be obtained by IBAE, the present etching condition provides the best anisotropy and selectivity.

To evaluate the effect of sidewall damage due to RIE and IBAE, channel conduction was monitored by measuring the current-voltage (I-V) characteristics between the ohmic pads. Dry-etching-induced damage on the sidewalls of these channels can cause current reduction by effectively reducing the width of the channels because of the formation of damage layers. Figure 4-6 shows saturation current as a function of channel width. Samples etched by RIE in Cl_2 at 250 V and IBAE with Ar^+ and Cl_2 at 500 V showed similar results in saturation current measurements. Channel conduction was still observed with channel widths down to 0.08 μm. This implies that any sidewall damage under these etching conditions does not alter electronic transport significantly. The estimated saturation current shown in the figure was calculated by assuming 0.06 μm for the depletion width and 7.2×10^6 cm/s for the saturation velocity. The 0.06 μm depletion width is expected for GaAs doped at 1×10^{18} cm^{-3} with normal pinning of the Fermi level at the surface. There is good agreement between the measured and estimated current. Similar to surface damage, dry-etching-induced sidewall damage was found to have a dependence on etching conditions such as ion energy and etching species. The measured saturation current decreases with increased ion energy and the addition of inert species.

The effects of redeposition of impurities and the difference between an etched bottom surface and a vertical sidewall were analyzed using ion beam etching (IBE). Unpatterned GaAs substrates were etched by IBE at different angles without the complication of reactive radicals, and comparison was made with samples etched by IBAE at the same angles. The electrical measurements and the Auger analysis of the GaAs substrates indicate that leakage current and redeposition of impurities are strongly dependent on etch angle when simple sputter etching is used. Figure 4-7 shows the Fe concentration obtained from Auger analysis after IBE at sample tilt angles varying from 0° to 90°, as a function of sputtered depth during analysis. Impurity concentrations increase with the angle used during etching. The highest concentration of Fe was detected at 90°. The largest leakage current in the diodes was measured at the same angle. It is expected that materials from the stainless steel stage can be sputtered off and redeposited on the samples for all etching angles. The tilt angle of the substrate can affect both the amount of impurities deposited and the efficiency of removal. The impurities on the etched samples can be substantially reduced by etching on a coated stage or by adsorption of reactive species on the surface. At an
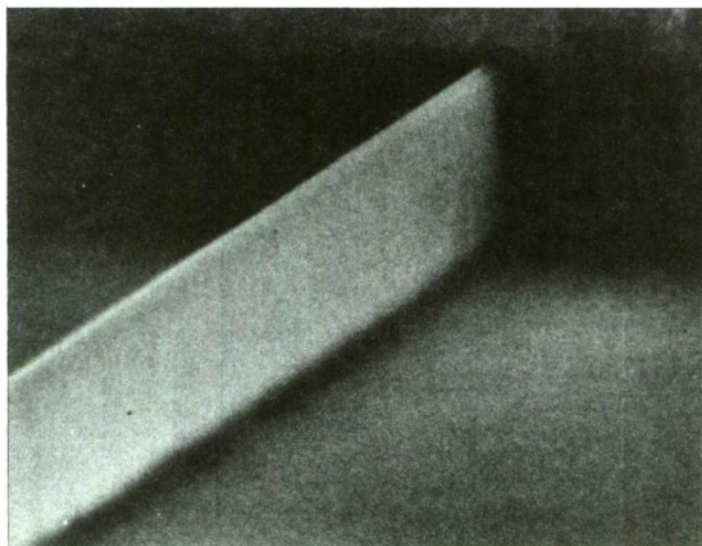
(a)
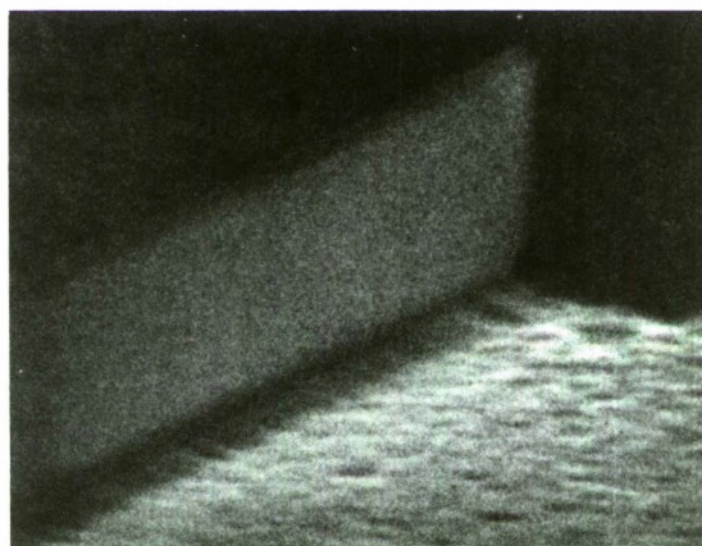
(b)

|← 1 μm →|

Figure 4-5.   Scanning electron micrographs showing sidewalls of 0.15-μm-wide channels etched by (a) RIE in Cl₂ at 5 mTorr and 250 V, and (b) IBAE with 500-V Ar⁺ and 2.8-mTorr equivalent Cl₂ pressure.

51
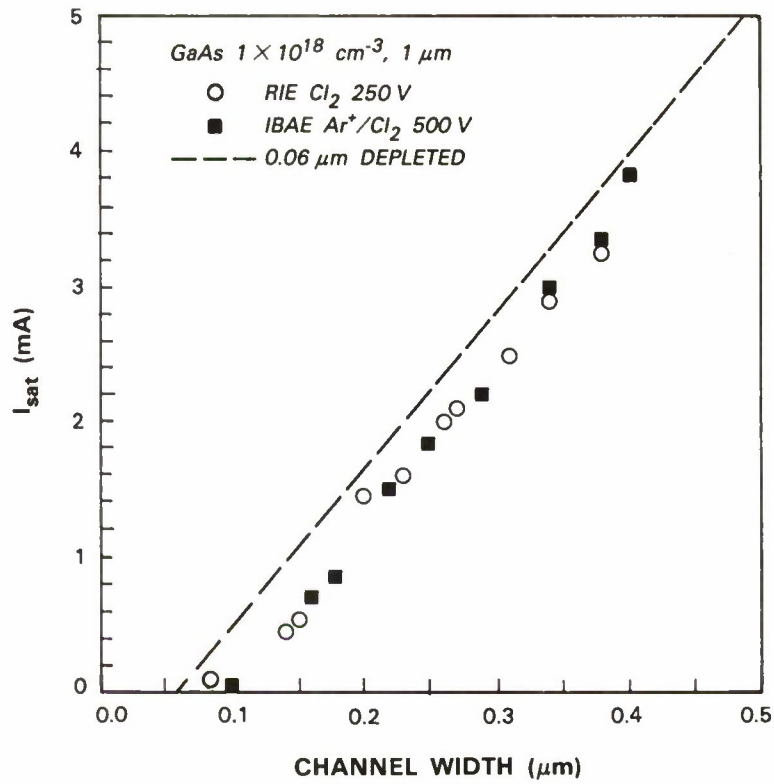
Figure 4-6.   Saturation current as a function of channel width after RIE and IBAE. The dotted line is the estimated current using 0.06 μm for the depletion width and 7.2 × 10⁶ cm/s for the saturation velocity.
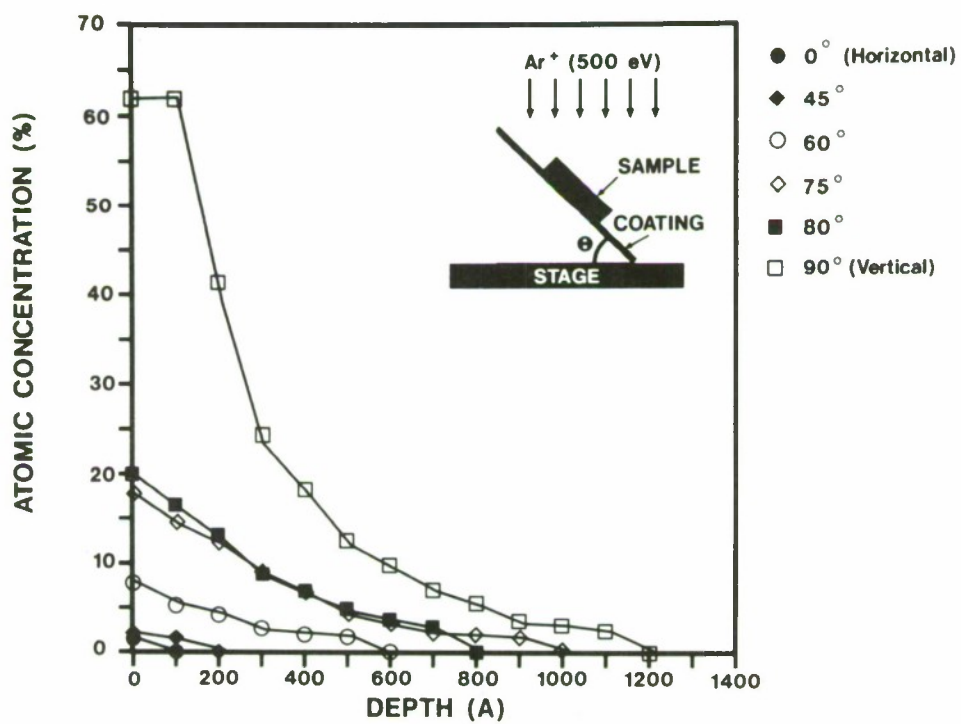
Figure 4-7. Fe concentration for samples etched by IBE on an unprotected stainless steel stage. The angle between the stage and the sample holder varies from 0° to 90°. Fe contamination is attributed to sputtering from the stage.

80° sample tilt, the Fe concentration at the surface is substantially less after IBAE (5 percent) than after IBE (20 percent). In addition, the effects of redeposition of impurities are expected to be even less for patterned samples because of shadowing by the etched structures.

The optimal etching condition that provides minimal damage of GaAs is achieved by using low ion energy, reactive gases, and a contamination-free etch chamber. These etching techniques are well suited for the fabrication of devices that require smooth and damage-free surfaces, such as vertical transistors, laser facets and mirrors, and quantum wires and dots.

S. W. Pang   D. J. Ehrlich
W. D. Goodhue   R. B. Goodman
T. M. Lyszczarz G. D. Johnson

4.3 HOMOEPITAXIAL SEMICONDUCTING DIAMOND

Semiconducting diamond has a number of properties that make it very useful for high-frequency, high-power devices. These include high electron and hole mobilities, high electric field breakdown, and high thermal conductivity.[4-6] A comparison of calculated electrical characteristics for diamond and silicon permeable base-transistors (PBTs)[7] is shown in Figure 4-8. With the use of a two-dimensional model, which accurately predicts the Si PBT characteristics, the current-voltage curves for a diamond PBT of similar geometry were obtained by modifying the mobility to that of holes in diamond. The predicted breakdown voltage is >600 V, and the maximum power dissipation is ≈150 W, more than 10 times that of the same device fabricated in Si.

The predicted improvement in high power performance for diamond over that of Si and GaAs devices has motivated the development of diamond transistors[5,6,8] and the epitaxial growth of semiconducting diamond films.[9,10] The system used to produce the epitaxial diamond films reported here consists of a plasma formed in 99.3 percent H_2 and 0.7 percent CH_4 by a 1-kW microwave source. The plasma is used to form free radicals and heat the diamond substrate to ≈800°C, as described elsewhere.[11] The growth rate is 0.5 μm h^{-1} on a (100) surface of a diamond substrate. A small piece of boron (0.1 cm diam.) is usually placed near the diamond substrate as a source of boron dopant. The films have acceptor levels on the order of 10^{16} cm^{-3}, as determined by capacitance-voltage measurements. The acceptors have an activation energy of 0.35 eV, as shown in Figure 4-9, which is consistent with boron doping. Figure 4-10 shows the smooth morphology of the 2.5-μm-thick epitaxial diamond film. The reflection electron diffraction of the film is the same as that of the original diamond substrate, and the Raman spectrum, shown in Figure 4-11, with the peak at 1,323 cm^{-1} indicates diamond with little or no detectable amorphous carbon.[12] Point-contact Schottky diodes are easily formed on these films using tungsten probes for the diode contact and indium foil for the ohmic contacts. Large area (100 × 100 μm) tungsten or aluminum Schottky-diode contacts formed on the diamond film are very leaky, as shown in Figure 4-12 for aluminum. Cleaning techniques which remove graphite, such as oxygen or hydrogen plasma etching or immersion in a solution of CrO_3 and H_2SO_4 at 200°C, do not improve the Schottky-diode characteristics.

M.W. Geis   J.J. Zayhowski
D.D. Rathman   D.L. Smythe
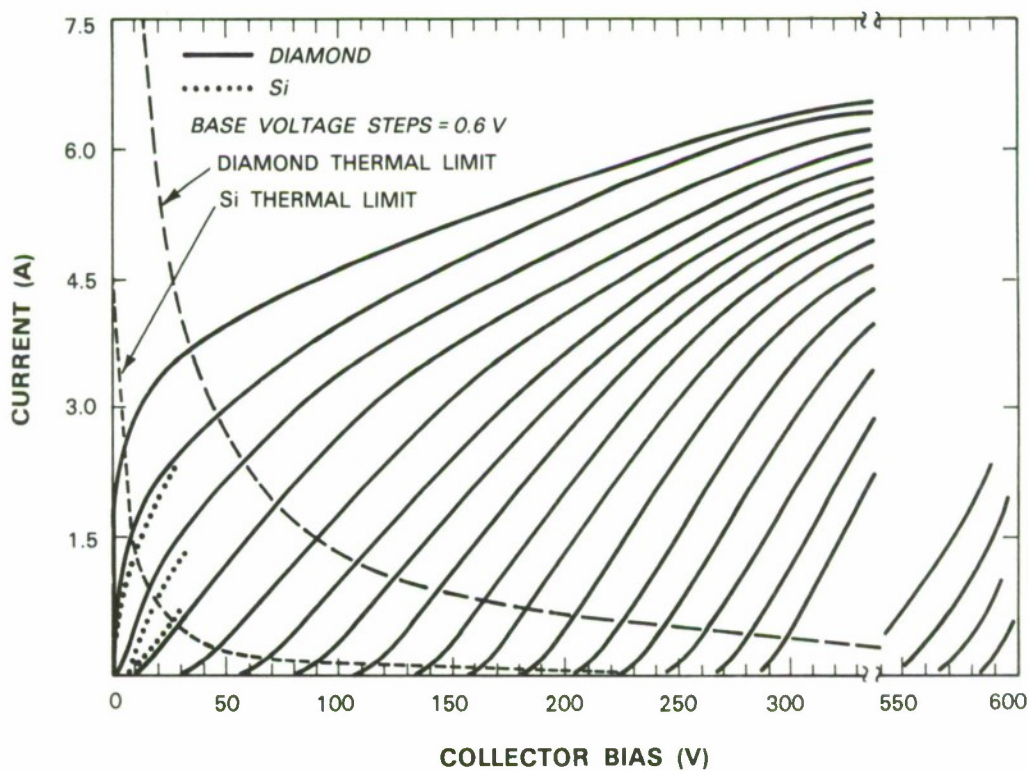
Figure 4-8.   The collector current as a function of collector voltage at several base voltages for permeable-base transistors made of Si and diamond. The devices are 160 × 40 µm in size and are mounted on a heat sink maintained at 25° C.. The maximum power dissipation curves for the devices were determined from maximum operational temperature and thermal conductivity. The maximum temperature is defined as the temperature at which the electron mobility for the Si device or the hole mobility for the diamond device decreases to 30 percent of its room temperature value. This temperature is 200° C for Si and 300° C for diamond.
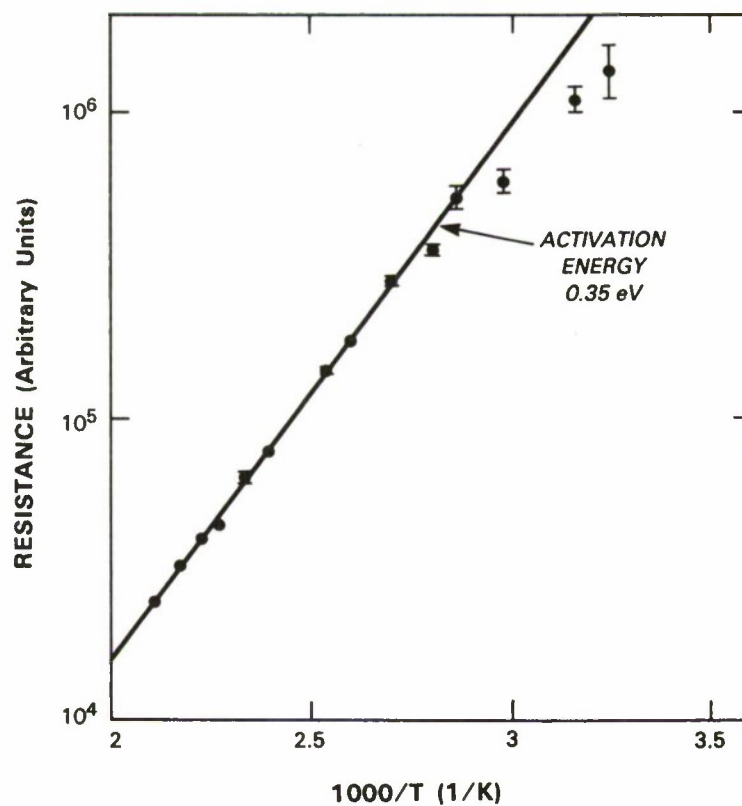
Figure 4-9. The resistance of an epitaxial diamond film as a function of temperature, determined using the van der Pauw method. The activation energy obtained from the slope of the line is 0.35 eV.
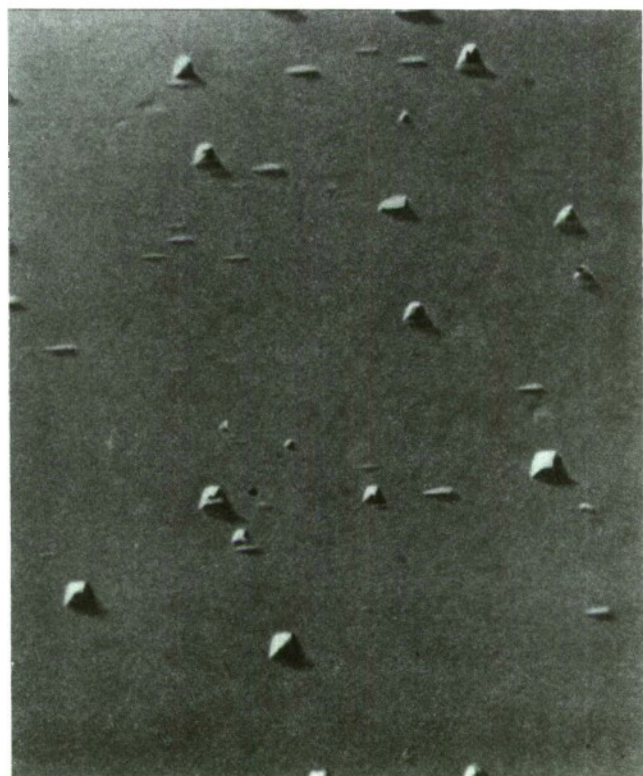
Figure 4-10.   Optical micrograph of a 2.5-µm-thick epitaxial diamond film.
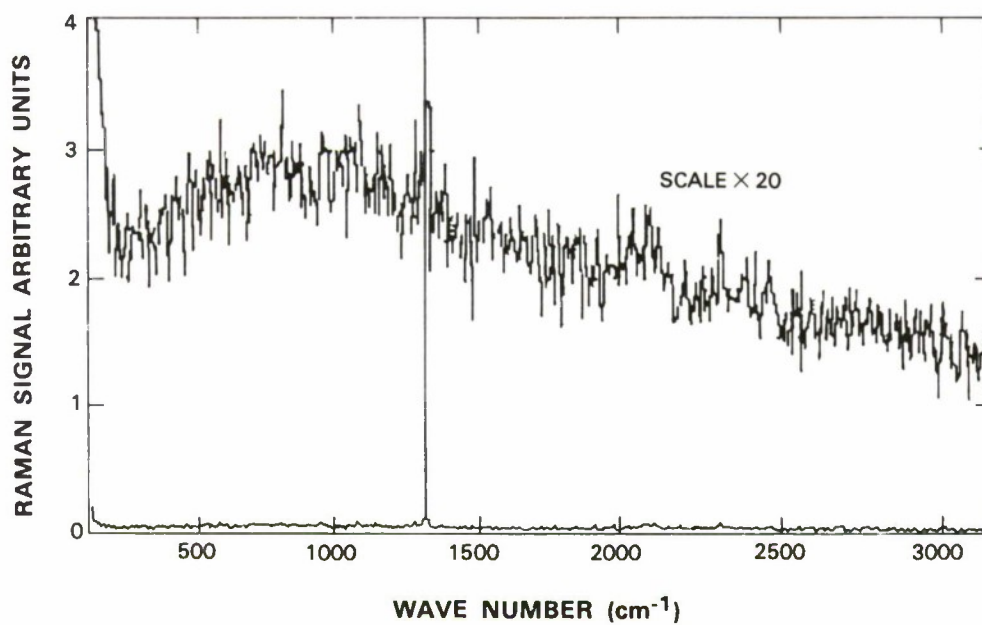
Figure 4-11. Raman spectrum of an epitaxial diamond film. An additional curve with a scale increase of 20 is also shown to better display the low signal background

58
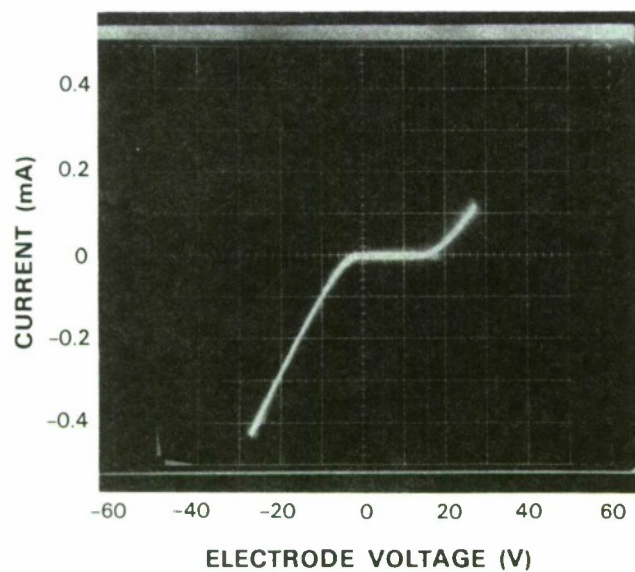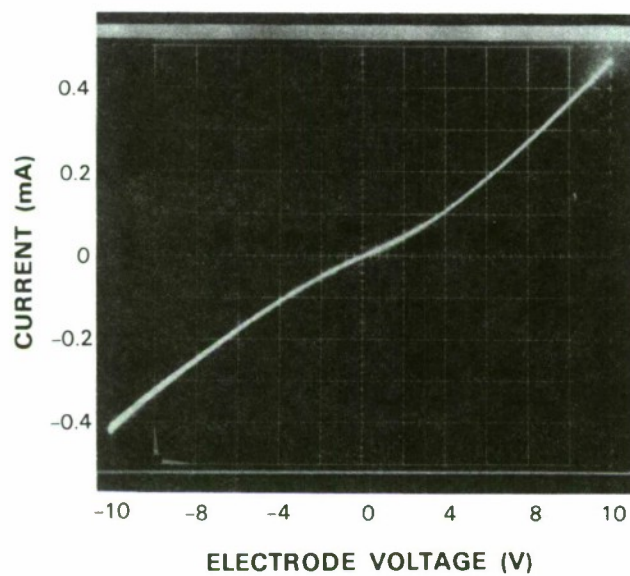
Figure 4-12. Current-voltage curves obtained on the epitaxial diamond film (a) for a point-contact and (b) for a large-area, electron-beam-evaporated aluminum contact (100 × 100 μm aluminum pad).

59

REFERENCES:

1. Solid State Research, Lincoln Laboratory, MIT (1988:3), pp. 49 this issue

2. S.W. Pang, J. Electrochem. Soc. **133**, 784 (1986).

3. D. Kirillov, C.B. Cooper, and R.A. Powell, J. Vac. Sci. Technol. B **4**, 1316 (1986).

4. V.K. Bazhenov, I.M. Vikulin, and A.G. Gontar, Sov. Phys. Semicond. **19**, 829 (1985).

5. M.W. Geis, D.D. Rathman, D.J. Ehrlich, R.A. Murphy, and W.T. Lindley, IEEE Electron Device Lett. **EDL-8**, 341 (1987).

6. M.W. Geis, N.N. Efremow, and D.D. Rathman, J. Vac. Sci. Technol. A **6**, 1953 (1988).

7. B.A. Vojak and G.D. Alley, IEEE Trans. Electron Devices **ED-30**, 877 (1983).

8. J.F. Prins, Appl. Phys. Lett. **41**, 950 (1982).

9. B.V. Derjaguin, B.V. Spitsyn, A.E. Goridetsky, A.P. Zakharov, L.L. Bouilov, and A.E. Sleksenko, J. Cryst. Growth **31**, 44 (1975).

10. M. Kamo, Y. Sato, S. Matsumoto, and N. Setaka, J. Cryst. Growth **62**, 642 (1983).

11. P.K. Bachman, W.R. Drawl, D. Knight, R. Weimer, and R.F. Messier, in *Diamond and Diamond-Like Materials Synthesis*, G.H. Johnson, A.R. Badzian, and M.W. Geis, eds. (Materials Research Society, 1988).

12. D.S. Knight, W.R. Drawl, A. Badzian, T. Badzian, and W.B. White, in *Diamond and Diamond-Like Materials Synthesis*, G.H. Johnson, A.R. Badzian, and M.W. Geis, eds. (Materials Research Society, 1988).

5. MICROELECTRONICS

5.1 420 × 420 CCD FRAME-TRANSFER IMAGER

A 420 × 420-pixel CCD imager has been designed and fabricated for use in space surveillance applications. This device is similar to an earlier imager[1,2] but with the addition of a frame store on the chip. The frame store is a temporary memory for the image charge and is used to reduce image smear encountered in the earlier device at low frame rates. The new imager is designed to be abuttable to other imagers on three sides, in contrast to the earlier two-side-abuttable chip. An improved output charge detection circuit has been incorporated on the device, and noise levels as low as 6 electrons rms have been measured at a data rate of 1 MHz.

Figure 5-1 shows a schematic of the new imager. The fabrication process is the same as that of the earlier device and uses a triple-polysilicon, three-phase structure with a buried channel.
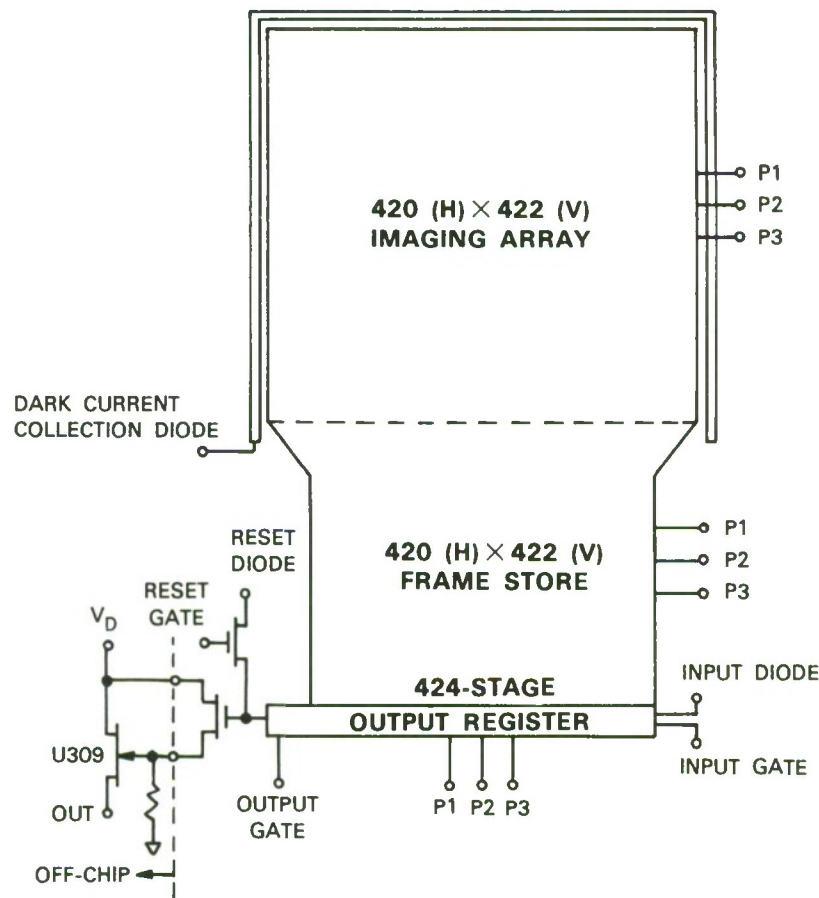
Figure 5-1.   Schematic of the 420 × 420-pixel frame-transfer CCD imager. Two extra rows of pixels are included in the imaging array and frame store to allow for possible misalignment of the light shield that is placed over the frame store and output register.

61

The optical image is incident on the 420 × 420-pixel imaging array that forms the upper portion of the device. The dark current collection diode along the top and sides is used to collect thermally generated charge from the sawn edges of the chip before it reaches the imaging pixels. At the end of the image integration period the integrated charge is clocked into a 420 × 420 frame-store region. A tapered section of 30 rows of pixels at the top of the frame store provides a transition from the 27 × 27-μm pixels of the imaging array to the 23(H) × 18(W)-μm pixels of the frame store. The charge in the frame store is then transferred line-by-line to the output register and read out through the output charge sensing circuit during the next image integration period. A light shield consisting of a few thousand angstroms of aluminum is placed over the frame store and output register, since these regions are not used for image sensing. Two extra rows of pixels in each array are included to allow for potential misalignment of the light shield with respect to the imaging-array/frame-store boundary. This misalignment is anticipated on future back-illuminated versions of the device where difficult photomask alignments for the light shield must be made between front and back surfaces of the wafer. Figure 5-2 shows a photograph of a packaged device (the imager in this photo does not have the Al light shield). The chip size is 12 × 20 mm.
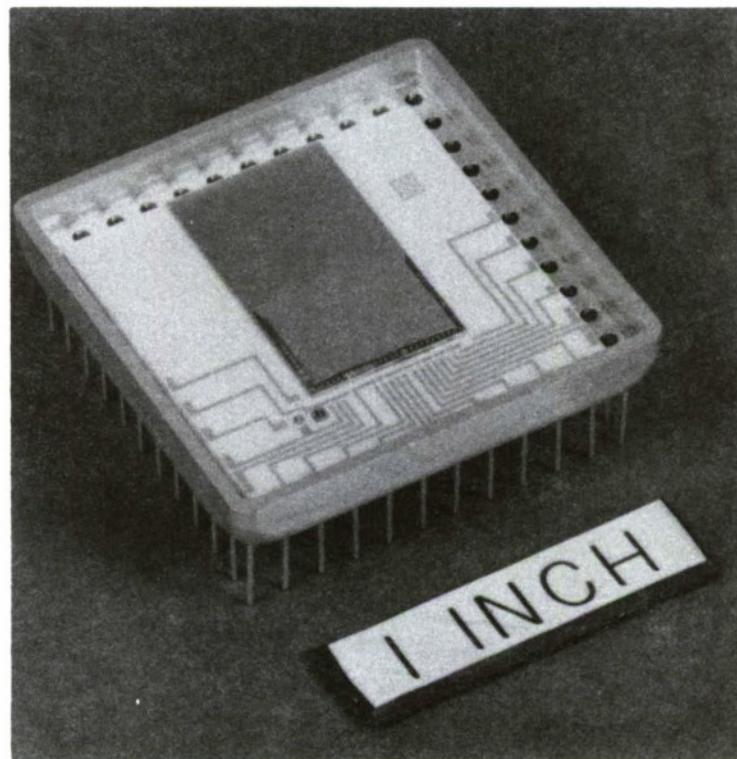
Figure 5-2.   Photograph of a CCD imager chip mounted in a 44-pin package.

96410-1

62

The frame store is important as a fast-in/slow-out memory because it allows an image to be rapidly removed from the imaging array while still permitting an output data rate low enough for low-noise signal extraction. In the earlier device, which contained only the imaging array, the entire image had to be read out before the imaging array could begin integrating the next frame. The readout time was almost 0.2 s at a 1-MHz output data rate, and therefore significant image smear effects could be seen at frame rates faster than 1 f/s. In the new device, the image can be clocked into the frame store in about 2 ms, and the image smear effects are reduced by a factor of 100. The frame-transfer speed is limited to a minimum of 2 ms by the RC time constant of the polysilicon gates.

A major feature of this device is that it is designed to be closely abuttable to three other chips so that multichip focal plane arrays of these imagers can be made. The pixels are brought close to the die edge along the top and left sides of the imaging array, but along the right edge extra space must be allotted to the clock lines. In multichip arrays it is important to minimize the gap between adjacent imagers. We expect to achieve a gap of no more than 2 to 3 pixels along the top seam, but a gap of 4 to 6 pixels is expected along the side seams because of the clock lines.

Another new feature concerns the design of the output circuit that peforms the charge-to-voltage conversion. In the previous imager the output FET had gate dimensions of $4 \times 40 \ \mu m$ and the responsivity of the circuit was 3.5 to 4 μV/electron. In the new device the gate has been decreased to $2 \times 10 \ \mu m$ and some parasitic capacitances have been reduced, with the result that the responsivity has been increased to about 11 to 12 μV/electron. Noise measurements have been made at an output clock rate of 1 MHz and a temperature of $-40°C$. For the earlier device the noise was typically 15 electrons rms, while the new device has produced levels of 6 electrons . rms. This is the lowest reported noise level for a CCD at this data rate.

<div align="right">B.E. Burke</div>

5.2 TECHNIQUE FOR MONOLITHICALLY INTEGRATING GaAs/AlGaAs LASERS OF DIFFERENT WAVELENGTHS

We have developed a technique using molecular beam epitaxy (MBE) for growing GaAs and AlGaAs layers with thicknesses and Al content that vary in a controlled manner over the surface of a (100)-oriented GaAs substrate. The technique has been used to fabricate lasers which operate 40 nm apart in wavelength from two different regions of a single wafer. By combining this technique with one- or two-dimensional GaAs/AlGaAs laser array technology,[3,4] a multiwavelength optical interconnect technology is possible.

Several groups have achieved layer thickness variations in the GaAs/AlGaAs system by growing upon substrates in which grooves have been etched, thereby relying on the growth rate differences between various crystallographic planes.[5] This etched-groove process achieves variations of layer thickness at the expense of planarity and creates variations only at the edges and sidewalls of the grooves. In our process the mechanism for locally controlling the thickness and

Al content of the layers is the Ga sticking coefficient, which is manipulated through the control of local substrate temperature in an MBE growth environment. The sticking coefficient of Ga dramatically decreases with substrate temperatures higher than 700°C (Reference 6). Therefore in layers grown above 700°C, the thicknesses of GaAs layers and AlGaAs layers decrease as temperature increases. In addition, the loss of Ga in the AlGaAs layers causes an increase in the fraction of AlAs and a consequent increase in the local bandgap.

To demonstrate that lasers of different wavelengths can be monolithically integrated by this technique, the following epitaxial layers were grown on a p^+-GaAs substrate: a high-Al-content p-AlGaAs cladding layer, a low-Al-content undoped AlGaAs layer, five GaAs active wells with undoped AlGaAs barriers, a low-Al-content undoped AlGaAs layer, a high-Al-content n-AlGaAs cladding layer, and an n-GaAs contacting layer. During the entire growth process the substrate was mounted with indium on a slotted MBE mounting block to create zones of two different temperatures at the surface to the substrate. A diagram of the slotted mounting block is shown in Figure 5-3. With the temperature of the block set at 720°C, the surface temperature of the substrate was 720°C over the indium-contacted regions and 680°C over the uncontacted regions, as measured by a two-color infrared pyrometer. The shutters were timed to give nominal well and barrier thicknesses of 10 nm and 20 nm, respectively, at 680°C.
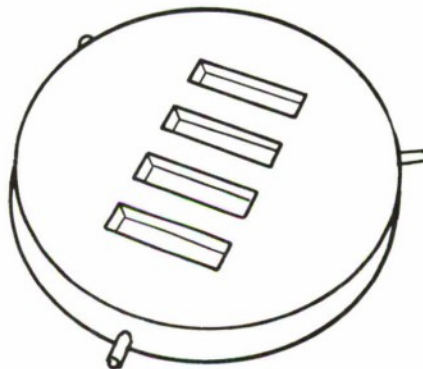
Figure 5-3.   Diagram of the slotted mounting block used to form regions of different temperatures on the surface of the wafer.

Broad-area lasers were fabricated and cleaved from both the hotter and colder surface-temperature growth regions of the wafer. Figure 5-4 shows the pulsed power output vs current for typical lasers fabricated from the two regions. Lasers in the colder region had threshold current densities around 0.9 kA cm^{-2}, differential quantum efficiencies of 15 percent per facet, and wavelengths around 865 nm, while lasers in the hotter region had threshold current densities around 1.5 kA cm^{-2}, differential quantum efficiencies of 7 percent per facet, and wavelengths around 825 nm. Figure 5-5 shows wavelength spectra of lasers from the two regions. No attempt has been made to optimize the growth conditions with regard to threshold current density.
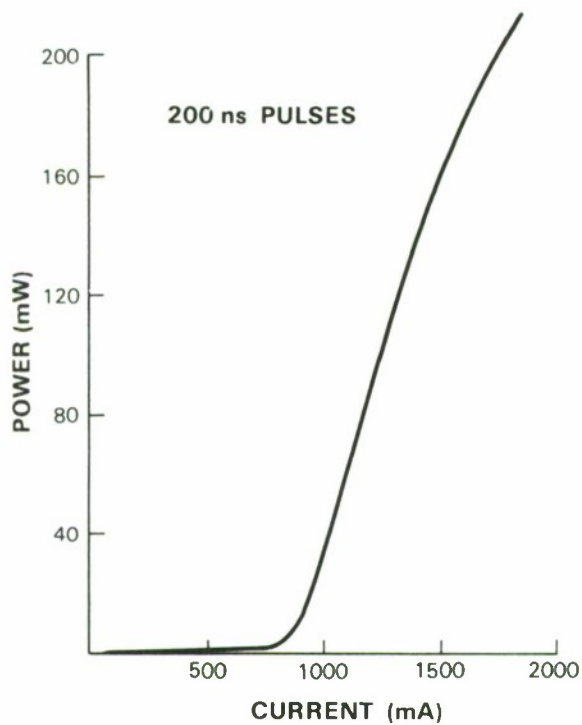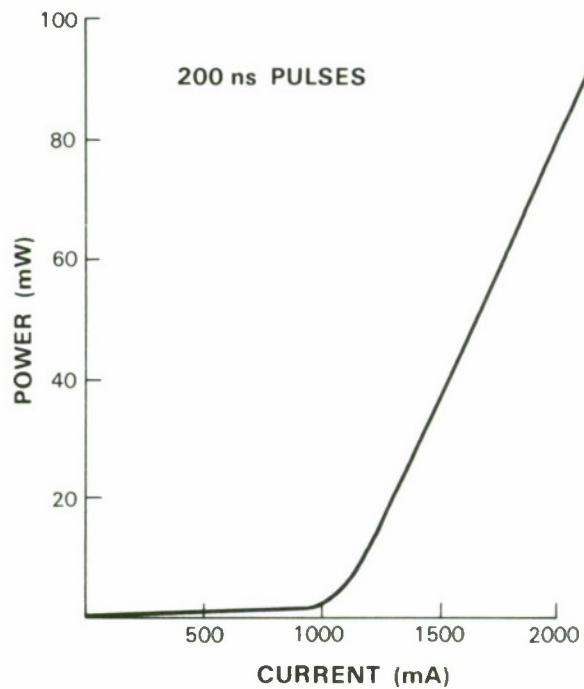
Figure 5-4.   Optical power vs current for broad-area lasers fabricated from (a) a colder and (b) a hotter region of the wafer.
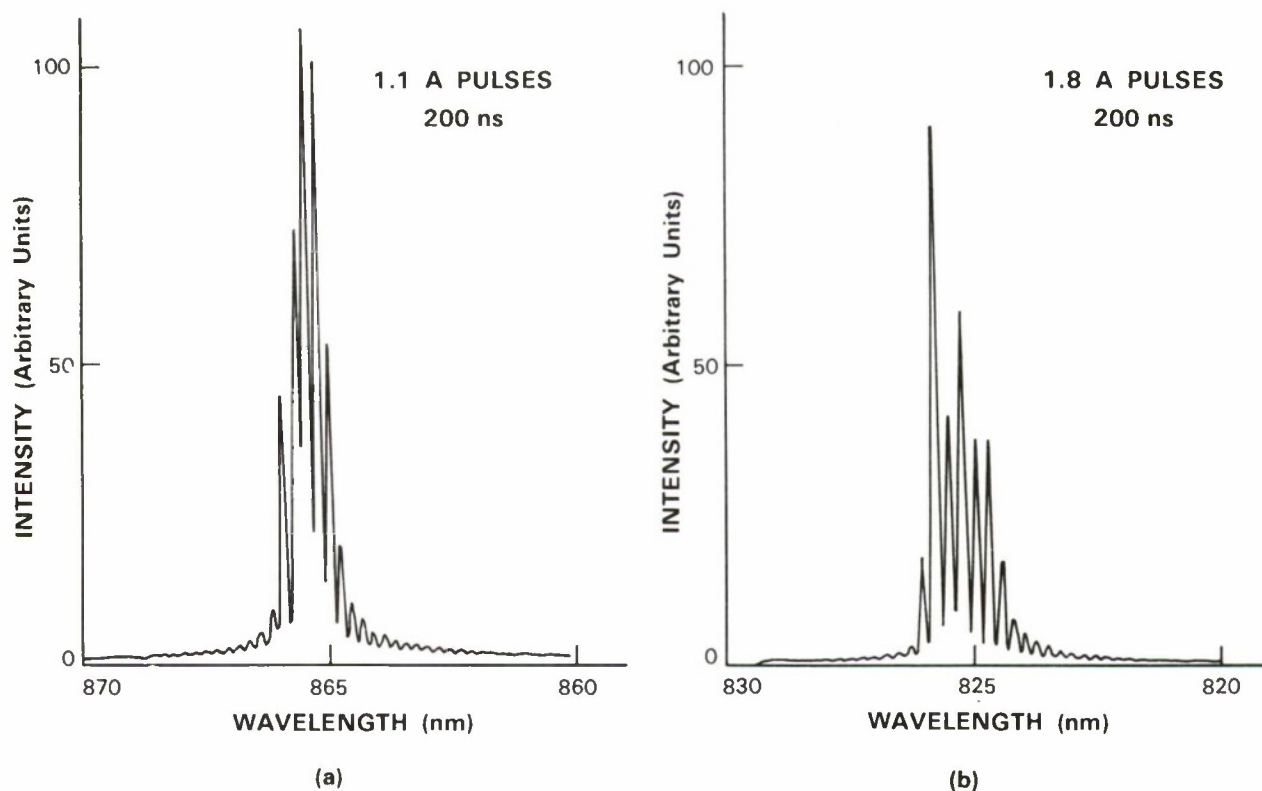
Figure 5-5. Spectra from broad-area lasers fabricated from (a) a colder and (b) a hotter region of the wafer.

In summary, we have used the temperature dependence of the Ga sticking coefficient for the first time to intentionally fabricate lasers from a single wafer with significant differences in wavelength. Beside being useful in the monolithic integration of lasers of different wavelengths, this technology is also applicable to a number of other device and material systems.

W.D. Goodhue
J.P. Donnelly
J.J. Zayhowski

66

REFERENCES

1. Solid State Research Report, Lincoln Laboratory, MIT (1985:1), p. 31, DTIC AD-A160922.

2. B.E. Burke, R.W. Mountain, P.J. Daniels, and D.C. Harrison, Opt. Eng. **26**, 890 (1987).

3. D.R. Scifres, C. Lindstrom, R.D. Burnham, W. Streifer, and T.L. Paoli, Electron Lett. **19**, 169 (1983).

4. J.P. Donnelly, W.D. Goodhue, T.H. Windhorn, and R.J. Bailey, Appl. Phys. Lett. **51**, 1138 (1987).

5. See, for example, W.T. Tsang and A.Y. Cho, Appl. Phys. Lett. **30**, 293 (1977).

6. See, for example, J. Ralston, G.W. Wicks, and L.F. Eastman, J. Vac. Sci. Technol. B **4**, 594 (1986).

6. ANALOG DEVICE TECHNOLOGY

6.1 SUPERCONDUCTING THIN FILMS OF BiSrCaCuO

Since the discovery of superconductivity in the BiSrCaCuO (BSCCO) system,[1] superconducting thin films in this system have been prepared by a variety of techniques, including coevaporation,[2] cosputtering,[3,4] sputtering of a composite target,[5] and precursor pyrolysis.[6] In this section, we report the preparation of such films by sequential electron-beam evaporation followed by oxygen annealing, a technique previously used[7,8] for preparing superconducting $YBa_2Cu_3O_x$ (YBCO) films. For our best BSCCO film, zero resistance was observed at 90 K, and the critical current increased from 8×10^4 A/cm^2 at 77 K to 2.3×10^5 A/cm^2 at 4.2 K.

Thin films composed of successive Cu, Bi and $Sr_{2/3}Ca_{1/3}F_2$ layers were deposited on polished <100> MgO substrates in a single-electron-gun, three-hearth vacuum system employed earlier for preparing YBCO films.[7] The substrates were held at ambient temperature during deposition. The Cu and Bi sources had purities of 99.99 and 99.999 percent, respectively. The fluoride source consisted of pieces from a solid-solution $Sr_{2/3}Ca_{1/3}F_2$ single crystal grown by melting a 2:1 molar mixture of optical-grade SrF_2 and CaF_2 single-crystal chips, then solidifying the melt directionally by the vertical gradient-freeze method. Films with better chemical stability and more accurately controlled composition are obtained by using the alkaline earth fluorides (which vaporize and condense as fluoride molecules) as sources instead of the corresponding metallic elements, which react strongly with oxygen and water vapor. The fluoride technique was first employed in preparing YBCO films by coevaporation with a BaF_2 source,[8] and it has also been used in the preparation of BSCCO films by coevaporation.[2] Films having a nominal post-oxidation composition of $Bi_2Sr_2Ca_1Cu_2O_x$ were prepared by depositing the following sequence of three layers with thicknesses monitored by a quartz-crystal oscillator: Cu, 25 nm; Bi, 75 nm; and $Sr_{2/3}Ca_{1/3}F_2$, 148 nm. Typically, this sequence was repeated six times, for a total film thickness of about 2 μm.

Following deposition, the films were annealed in a tube furnace under flowing O_2. During the first part of each annealing run, the O_2 was bubbled through a water reservoir heated to 50 to 60°C. The furnace was heated to the annealing temperature, and film was inserted into the furnace. After the desired annealing time, the water reservoir was bypassed, so the dry O_2 was used for the remainder of the run. The furnace was cooled to 500°C at the rate of about 6°C/ min and then turned off.

Superconducting films were obtained by annealing at temperatures ranging from 780 to 870°C. Auger electron spectroscopy (AES) shows that the as-deposited multilayer structure is transformed, by diffusion, into a single layer of uniform composition. The composition appears to be uniform to within 100 Å of the film surface. Precise stoichiometric data could not be obtained using AES because the intensity of the line used to determine the Bi composition is small and the line is too close to a strong line for Ca. However, the AES data do show that the single-crystal source material for $Sr_{2/3}Ca_{1/3}F_2$ evaporates in stoichiometric proportion. X-ray diffraction data show that these films contain a dominant phase (c = 30.8 Å) that is reported[9,10] to

be superconducting with composition approximating $Bi_2(Sr, Ca)_3Cu_2O_8$, together with a second phase (c = 24.4 Å) that is reported[11,12] to be semiconducting with composition approximating $Bi_2(Sr, Ca, Bi)_2CuO_6$. A representative diffraction pattern, which was obtained for a film annealed at 870°C for 30 min, is shown in Figure 6-1. The (00ℓ) lines for the two phases are present, showing that the films are highly textured, with both phases having their c-axes perpendicular to the substrate. Such texturing is also observed for BSCCO films prepared by other techniques.[2-6] Also present in Figure 6-1 are the (105) and (110) lines for the superconducting phase. The (105) line is the strongest line observed in x-ray powder diffraction of BSCCO material.[10] The appearance of the (105) line in our spectrum indicated that there is a mosaic spread of the c-axis relative to the substrate.
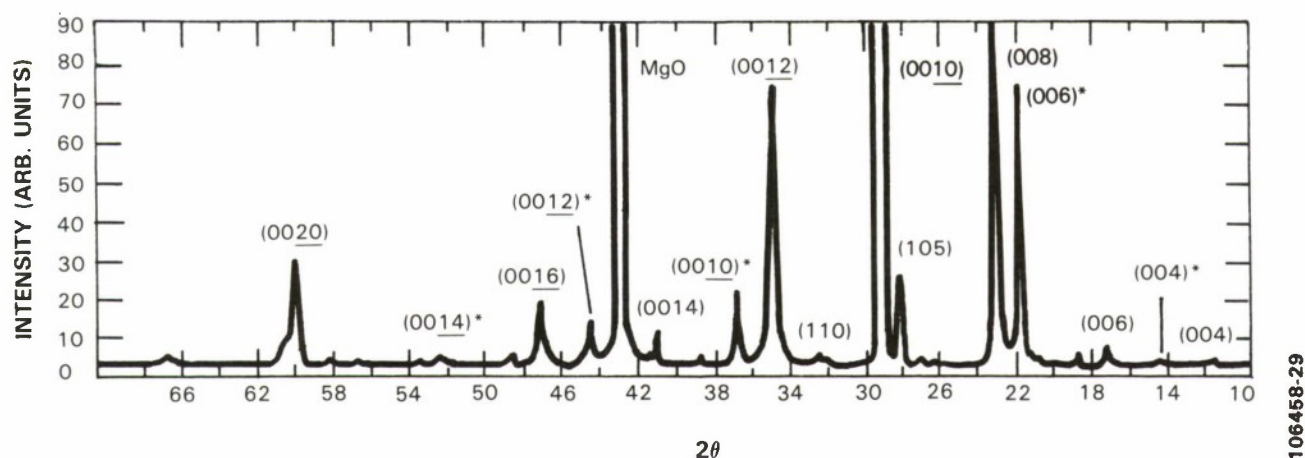
Figure 6-1. *X-ray diffraction 2θ scan of a BSCCO film annealed at 870°C for 30 min. The (00ℓ) lines for both the superconducting and semiconducting (*) phases are present. The appearance of the (105) and (110) lines suggests a mosaic spread of the c-axis relative to the MgO substrate.*

A four-point probe with tungsten contacts was used to measure the resistance of the annealed films as a function of temperature. Trace (a) in Figure 6-2 shows the results for a $Bi_2Sr_2Ca_1Cu_2O_x$ film annealed at 850°C for 30 min. The material exhibits metallic resistivity down to ≈110 K. The resistivity then begins to decrease slowly to a temperature of ≈90 K and finally drops sharply to zero at 85 K. The latter part of the transition (70 to 10 percent) has a width of ≈4 K. It is noteworthy that the long resistive tail, common to thin films of YBCO, is not present in this film. Trace (b) in Figure 6-2 shows the results obtained in initial measurements on the film of Figure 6-1, which exhibits the best superconducting properties. Although the surface roughness is too great for accurate resistivity measurements, the resistivity at room temperature is estimated to be about 500 $\mu\Omega$ cm. With decreasing temperature, the resistance decreases linearly down to about 110 K and then falls with increasing slope, reaching zero at 90 K. The dashed line in Figure 6-2 is a fit to the resistance above 90 K and is extrapolated to 0 K. Repeated temperature cycling, which resulted in the condensation of water on the film, caused
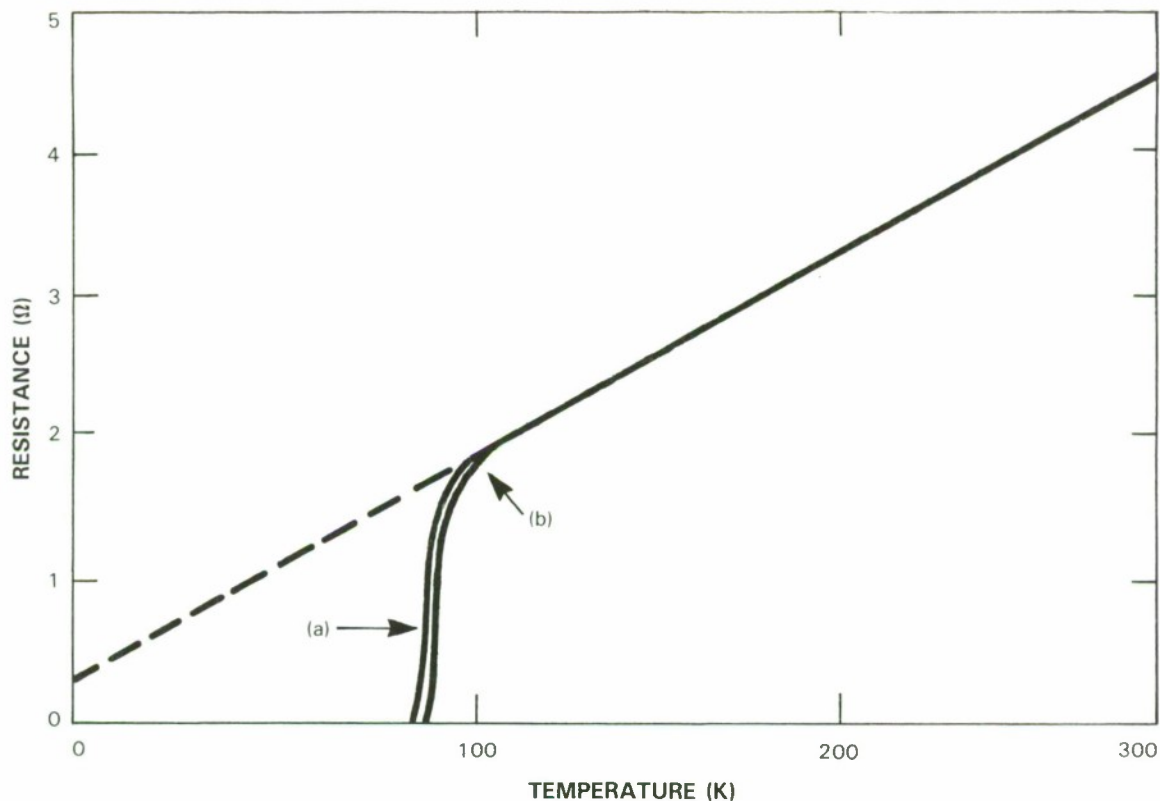
Figure 6-2. Resistance vs temperature for two BSCCO films annealed at (a) 850°C and (b) 870°C for 30 min. Note that the resistive tail common to YBCO is not present in these films.

the resistance curve of this film to develop a low-temperature tail that gave a small reduction in the zero-resistance temperature $T_c(R = 0)$. After ten cycles, T_c had fallen to 85 K. For other films, the initial value of T_c generally decreased with decreasing annealing temperature. In a number of cases, T_c was between 80 and 85 K. The lowest value was 70 K, which was obtained for a film annealed at 780°C for 30 min.

To determine the critical current density J_c, the films were scribed to form a narrow conducting channel, and current-voltage measurements were made with the four-point probe. For the film of Figures 6-1 and 6-2(b), Figure 6-3 shows the temperature dependence of J_c, defined as the current that produces a voltage of 1 mV, which corresponds to a resistivity of the order of 0.1 $\mu\Omega$ cm. The value of J_c increases from 0.8×10^5 A/cm^2 at 77 K to 2.3×10^5 A/cm^2 at 4.2 K. It should be noted that these results were obtained after the film had been thermally cycled several times with $T_c(R = 0)$ decreasing to 85 K.

The preferential ordering of the films which is observed in x-ray diffraction analysis of our thin films accounts for the sharp transistions, $\Delta T_c \approx 4$ K, and high critical currents in our films. The preferred orientation is most probably a direct result of the large structural anisotropy of the BSCCO structure which has been shown to cause preferential ordering in other materials. Since

71
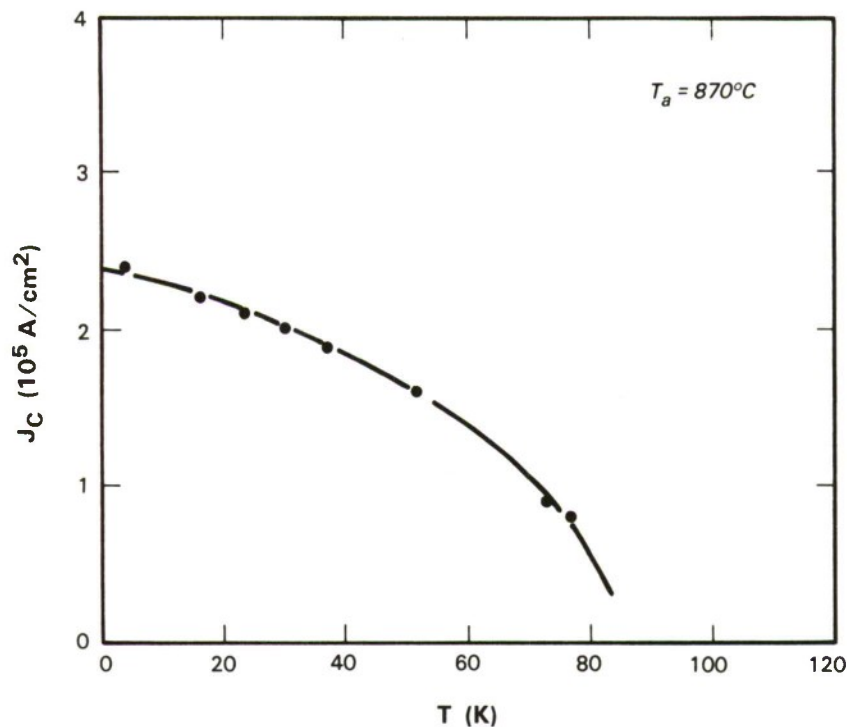
Figure 6-3. Critical current density for BSCCO film annealed at 870° C for 30 min. These data were taken after the film had developed a resistive tail, decreasing $T_c(R = 0)$ to 85 K.

YBCO does not exhibit strong preferential ordering, the processing of YBCO to produce high-quality films is more complex. Our selection of <100> MgO as a substrate material is dictated by our desire to use thin films of BSCCO in microwave electronics. We have attempted to deposit stoichiometric films of BSCCO on yttria-stabilized zirconia (YSZ), but during the high-temperature anneal there was massive substrate reaction. Superconducting films of BSCCO have been successfully made on YSZ by increasing the amount of deposited Sr and Ca.[4] However, substrate reaction at the film-substrate interface makes this process unacceptable for electronic applications.

In summary, thin films of BiSrCaCuO have been successfully produced by sequential electron-beam evaporation on <100> MgO substrates. The films contain both the superconducting metallic phase and the semiconducting phase of BSCCO. The films are highly textured with the c-axis of the BSCCO perpendicular to the plane of the MgO substrate. Our best films to date have a zero-resistance temperature of 90 K and transition widths $\approx$ 4 K. The films have critical current densitites of 8×10^4 A/cm^2 at 77 K, increasing to 2.3×10^5 A/cm^2 at 4.2 K.

The sharp superconducting transition and the high critical currents are attributed to the preferential ordering in the films. This characteristic, in addition to the existence of a superconducting phase at 110 K, may make BSCCO more attractive for device applications than YBCO.

J.W. Steinbeck
A.C. Anderson
B-Y. Tsaur
A.J. Strauss

6.2 Nb THIN-FILM CAPACITORS FOR SUPERCONDUCTIVE CIRCUITS

The multichannel superconductive time-integrating correlator[13] currently under development requires thin-film parallel L-C resonators with Q's $\approx$ 500 at a resonant frequency of $\approx$20 MHz. The loss due to the shunt conductance of the capacitor is strongly dependent on the material and the method of deposition of the counterelectrode. Although the electrical requirements of the circuit can be easily met with Nb/Pb or Pb-alloy capacitors, from the point of view of long-term stability and thermal cyclability, it is highly desirable that an all-refractory-metal process be developed.

The capacitors for the L-C resonators (Figure 6-4) were formed by sputter depositing and patterning a Nb film on a Si wafer, covering the Nb with evaporated SiO, and opening windows in the SiO. The exposed Nb was partially anodized in a solution of ammonium pentaborate and ethylene glycol to form the dielectric. The Nb_2O_5 thus formed had a thickness, proportional to the anodization voltage, of 25 Å/V and a dielectric constant of $\approx$32. It was found that, when the thermally evaporated Pb counterelectrode was replaced by a sputter-deposited Nb film, the Q of the L-C resonators decreased from 500 to only $\approx$150. The effect of the sputtering parameters on
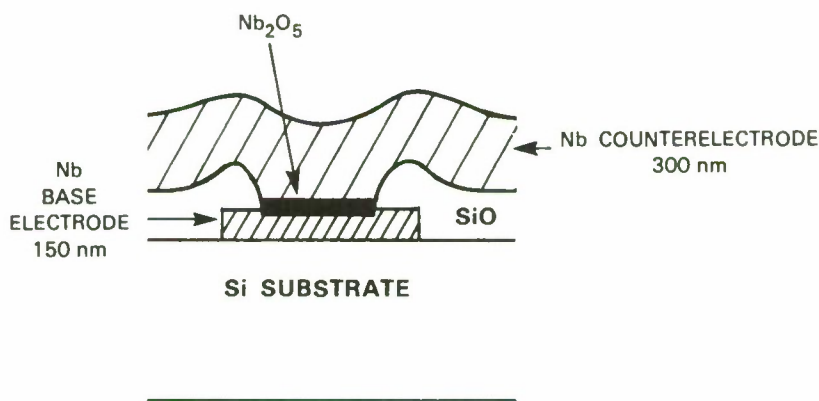
Figure 6-4. Cross-sectional view of a Nb thin-film capacitor.

73

the Q was studied. The Q improved with decrease in dc sputtering power from 1,500 to 500 W and an increase in Ar pressure from 10 to 20 mTorr. This indicates that damage to the dielectric film is caused by energetic particle bombardment and the consequent increase in the substrate temperature during sputtering. Subsequent improvement in the Q was obtained by increasing the current density during the dielectric anodization process.

The process optimization led to all-Nb thin-film capacitors with breakdown voltages >85 percent of the anodic oxide forming voltage. At 4.2 K, the dielectric strength of the anodic oxide was $>3 \times 10^6$ V/cm and the loss tangent of the capacitors was ≈ 0.002 at 1 MHz. The resonant frequency was varied between 10 and 20 MHz by increasing the thickness of the dielectric. For dielectric thicknesses >75 nm, the Q of the resonator exceeded 400. The resonant frequency was stable within less than 0.1 percent after repeated thermal cycling. Correlator circuits incorporating these capacitors are in fabrication.

<div align="right">M. Bhushan</div>

REFERENCES

1. H. Maeda, Y. Tanaka, M. Fukatomi, and T. Asano, Jpn J. Appl. Phys. Lett. **27**, 209 (1988).

2. C.E. Rice, A.F.J. Levi, R.M. Fleming, P. Marsh, K.W. Baldwin, M. Anzlower, A.E. White, K.T. Short, S. Nakahara, and H.L. Stormer, Appl. Phys. Lett. **52**, 1828 (1988).

3. J.H. Kang, R.T. Kampwirth, and K.E. Gray, Appl. Phys. Lett. **52**, 2080 (1988).

4. D.W. Face, M.J. Neal, M.M. Matthiesen, J.T. Kucera, J. Crain, J.M. Graybeal, T.P. Orlando, and D.A. Rudman, Appl. Phys. Lett. **53**, 246 (1988).

5. B.T. Sullivan, N.R. Osborne, W.N. Hardy, J.F. Carolan, B.X. Yang, P.J. Michael, and R.R. Parsons, Appl. Phys. Lett. **52**, 1992 (1988).

6. S.L. Furcone and Y.-M. Chiang, Appl. Phys. Lett. **52**, 2180 (1988).

7. B-Y. Tsaur, M.S. DiIorio, and A.J. Strauss, Appl. Phys. Lett. **51**, 858 (1987).

8. A. Mogro-Campero, B.D. Hunt, L.G. Turner, M.C. Burrell, and W.E. Balz, Appl. Phys. Lett. **52**, 584 (1988).

9. P.M. Mankiewich, J.H. Scofield, W.J. Skocpol, R.E. Howard, A.H. Dayem, and E. Good, Appl. Phys. Lett. **51**, 1753 (1987).

10. J.M. Tarascon, Y. LePage, P. Barboux, B.G. Bagley, L.H. Greene, W.R. McKinnon, G.W. Hull, M. Girond, and D.M. Hwang, Phys. Rev. B **37**, 9382 (1988).

11. S.I. Shah, G.A. Jones, and M.A. Subramanian, Appl. Phys. Lett. **53**, 429 (1988).

12. S.A. Sunshine, T. Siegrist, L.F. Schneemeyer, D.W. Murphy, R.J. Cava, R.B. van Dover, R.M. Fleming, S.H. Glaram, S. Nakahara, R. Farrow, J.W. Rupp, Jr., and W.F. Peck, Phys. Rev. B **38**, 893 (1988).

13. Solid State Research Report, Lincoln Laboratory, MIT (1986:2), p. 59, DTIC AD-A180799.

REPORT DOCUMENTATION PAGE

1a. REPORT SECURITY CLASSIFICATION	1b. RESTRICTIVE MARKINGS
Unclassified	

2a. SECURITY CLASSIFICATION AUTHORITY	3. DISTRIBUTION/AVAILABILITY OF REPORT
	Approved for public release; distribution unlimited.
2b. DECLASSIFICATION/DOWNGRADING SCHEDULE	

4. PERFORMING ORGANIZATION REPORT NUMBER(S)	5. MONITORING ORGANIZATION REPORT NUMBER(S)
1988:3	ESD-TR-88-209

6a. NAME OF PERFORMING ORGANIZATION	6b. OFFICE SYMBOL (If applicable)	7a. NAME OF MONITORING ORGANIZATION
Lincoln Laboratory, MIT		Electronic Systems Division

6c. ADDRESS (City, State, and Zip Code)	7b. ADDRESS (City, State, and Zip Code)
P.O. Box 73 Lexington, MA 02173-0073	Hanscom AFB, MA 01731

8a. NAME OF FUNDING/SPONSORING ORGANIZATION	8b. OFFICE SYMBOL (If applicable)	9. PROCUREMENT INSTRUMENT IDENTIFICATION NUMBER
HQ AF Systems Command	AFSC/XTKT	F19628-85-C-0002

8c. ADDRESS (City, State, and Zip Code)	10. SOURCE OF FUNDING NUMBERS			

8c. ADDRESS (City, State, and Zip Code)	PROGRAM ELEMENT NO.	PROJECT NO.	TASK NO.	WORK UNIT ACCESSION NO.
Andrews AFB Washington, DC 20334-5000	63250F	221		

11. TITLE (Include Security Classification)

Solid State Research

12. PERSONAL AUTHOR(S)
Alan L. McWhorter

13a. TYPE OF REPORT	13b. TIME COVERED	14. DATE OF REPORT (Year, Month, Day)	15. PAGE COUNT
Quarterly Technical Report	FROM 1 May TO 31 Jul 88	15 August 1988	106

16. SUPPLEMENTARY NOTATION

None

17. COSATI CODES			18. SUBJECT TERMS (Continue on reverse if necessary and identify by block number)
FIELD	GROUP	SUB-GROUP	electrooptical devices analog device technology e-beam lithography quantum electronics lasers dry etching materials research laser arrays charge-coupled imagers submicrometer technology wavefront sensor superconductors microelectronics nonlinear optics thin-film capacitors

19. ABSTRACT (Continue on reverse if necessary and identify by block number)

This report covers in detail the research work of the Solid State Division at Lincoln Laboratory for the period 1 May through 31 July 1988. The topics covered are Electrooptical Devices, Quantum Electronics, Materials Research, Submicrometer Technology, Microelectronics, and Analog Device Technology. Funding is provided primarily by the Air Force, with additional support provided by the Army, DARPA, Navy, SDIO, NASA, and DOE.

20. DISTRIBUTION/AVAILABILITY OF ABSTRACT	21. ABSTRACT SECURITY CLASSIFICATION
☐ UNCLASSIFIED/UNLIMITED ☒ SAME AS RPT. ☐ DTIC USERS	Unclassified

22a. NAME OF RESPONSIBLE INDIVIDUAL	22b. TELEPHONE (Include Area Code)	22c. OFFICE SYMBOL
Lt. Col. Hugh L. Southall, USAF	(617) 981-2330	ESD/TML

DD FORM 1473, 84 MAR 83 APR edition may be used until exhausted.   **UNCLASSIFIED**
All other editions are obsolete.